Centro de Investigación y de Estudios Avanzados del

Instituto Politécnico Nacional

UNIDAD ZACATENCO

Programa de Nanociencias y Nanotecnología

Efectos del tamaño de partícula en las propiedades superconductoras del $SmFeAsO_{1-x}F_x$

TESIS

Que presenta

Francisco Emmanuel Sánchez Zacate

En cumplimiento parcial de los requisitos para obtener el grado de

Doctor en Ciencias

En la especialidad de

Nanociencias y Nanotecnología

Directores de tesis:

Dr. Agustín Conde Gallardo

Dr. José Gerardo Cabañas Moreno

Ciudad de México Julio 2020

Center for Research and Advanced Studies of the

National Polytechnic Institute

ZACATENCO UNIT

Program on Nanoscience and Nanotechnology

Particle size effects on the superconducting properties of $SmFeAsO_{1-x}F_x$

THESIS

by

Francisco Emmanuel Sánchez Zacate

In partial fulfillment of the requirements for the degree of

Doctor of Philosophy

With the speciality of

Nanoscience and Nanotechnology

Thesis Advisors:

Dr. Agustín Conde Gallardo

Dr. José Gerardo Cabañas Moreno

Mexico City July 2020

Quiero dedicar mi trabajo de doctorado

a mi familia,

y en especial a mi mamá.

Gracias por el amor

y por enseñarme a vivir.

Acknowledgements

I would like to thank Dr. Agustín Conde and Dr. José Gerardo Cabañas for supervising my thesis work. I also greatly appreciate the support of my colleagues in the laboratory work.

I would like to acknowledge to Marcela Guerrero, M.A. Leyva, M. Dominguez, N. Castillo for their technical assistance, as well as CONACyT Mexico for the support granted during the Ph.D. scholarship. This work was partially supported by the project CB-239895-CONACyT.

Resumen

La presente tesis es un estudio sobre los efectos de la reducción del tamaño de partícula (r_g) en el superconductor a base de hierro $SmFeAsO_{1-x}F_x$. Este trabajo se centra en las propiedades magnéticas y su evolución a medida que se reduce el tamaño de las partículas. En primer lugar, se preparó una muestra policristalina (con cristales orientados al azar) de $SmFeAsO_{0.91}F_{0.09}$, mediante el método de reacción de estado sólido en un solo paso, aplicando una molienda manual usando un mortero y pistilo de ágata. Para la identificación de las fases, se usó la técnica de difracción de Rayos-X (XRD en inglés), la cual confirmó la muy baja presencia de fases no deseadas. La temperatura crítica de la muestra (T_c) fue determinada por la transición observada en la curva Resistencia-Temperatura, indicando una T_c=56.1 K (las curvas Magnetización-Temperatura indican 58.8 K). El contenido real de flúor en la muestra se determinó mediante comparación entre el valor experimental de T_c y el diagrama de fase T_c-x, de muestras sintetizadas de forma similar.

Esta muestra de alta calidad fue dividida y molida suavemente a mano durante diferentes intervalos de tiempo, para obtener un conjunto de muestras con una variedad de tamaños de partícula: 1680 nm (sin molienda), 550 nm, 470 nm, 405 nm, 345 nm y 220 nm. El rango de tamaño abarca desde el tamaño en volumen de la muestra sintetizada, hasta la escala de la longitud de penetración (220 nm). Los picos principales de los patrones de difracción de Rayos-X no presentan corrimientos sistemáticos, lo cual indica que todas las muestras mantienen la misma estructura cristalina. El tamaño de partícula se determinó directamente a partir de micrografías tomadas en un microscopio electrónico de barrido.

La caracterización magnética se realizó en un magnetómetro de muestra vibratoria. La naturaleza granular de las muestras se estableció por la presencia de una segunda caída (alrededor de T=19 K) en las curvas de Magnetización-Temperatura (M-T). Por otro lado, la región de magnetización virgen se estudió en las curvas de Magnetización-Campo Magnético (M-H). Se encontró que el campo crítico inferior (H_{c1}), que limita el régimen de Meissner, presenta una dependencia cuadrática respecto del tamaño de partícula: $H_{c1} \sim r_g^2$, con valores en el rango de $30 \leq H_{c1} \leq 395$ Oe, para $220 \leq r_g \leq 1680$ nm. Además, el campo de penetración completa H^*, que limita la región de magnetización virgen, sigue una ley logarítmica dependiente de r_g: $H^* = H_0 (1+r_g/r_0)$, con constantes H_0=709.97 Oe y r_0=178 nm. Los valores experimentales están en el rango de $510 \leq H^* \leq 1570$ Oe, para tamaños de partícula entre $220 \leq r_g \leq 1680$ nm. Ambos resultados experimentales concuerdan con algunos modelos teóricos aplicados previamente a otros superconductores de alta temperatura crítica (HTS en inglés).

Los valores experimentales obtenidos para H_{c1} se utilizaron para calcular la longitud de coherencia efectiva (ξ_{eff}). Es evidente que esta se acorta a medida que disminuye r_g, siguiendo una ley cuadrática $\xi_{eff} \sim r_g^2$, con valores en el rango de $0.37 \leq \xi_{eff} \leq 2.5$ nm, para $220 \leq r_g \leq 1680$ nm. A su vez, estos resultados sugieren que la longitud de penetración efectiva (λ_{eff}) aumenta cuando $r_g \rightarrow 0$.

El campo de irreversibilidad (H_{irr}) se determinó directamente a partir de los ciclos de histéresis de las curvas M-H, con valores en el rango de 7,1 a 15,8 kOe, para tamaños de partícula entre $220 \leq r_g \leq 1680$ nm. Para partículas con la misma escala que λ ($220 \leq r_g \leq 550$ nm), $H_{irr}^{1/3}$ disminuye linealmente con r_g, mientras que para la muestra con mayor tamaño de partícula (r_g=1680 nm) alcanza un valor de saturación. Este comportamiento puede ser explicado al considerar el límite para partículas pequeñas, del modelo de oscilaciones térmicas de los vórtices magnéticos (*flux creep* en inglés). Los valores de H_{irr} se utilizaron para estimar H_{c2}(50 K) sobre la base del modelo antes mencionado, obteniéndose magnitudes en el rango de $3.8 \leq H_{c2}(50\ K) \leq 22$ T, para $220 \leq r_g \leq 1680$ nm. A su vez, H_{c2}(50 K) permitió calcular el valor de $H_{c2}(0)$ (baja temperatura). Se obtuvieron magnitudes entre 18.5 T para r_g=220 nm, y hasta 107 T para la muestra con mayor tamaño de partícula (1680 nm). Estos valores son mucho más bajos que los propuestos en los primeros años posteriores al descubrimiento de los superconductores basados en hierro, pero concuerdan con el comportamiento observado de H_{irr} y con estudios más recientes, donde se asume que el rompimiento de los pares de Cooper en estos materiales es debido al alineamiento de los espines de los electrones, causado por el campo magnético aplicado.

La densidad de corriente crítica intragranular (J_{intra}) se determinó directamente a partir de las curvas M-H, mediante el modelo de Bean. La corriente crítica está determinada por el anclaje de los vórtices magnéticos, y está compuesta por la suma de dos componentes. Por lo tanto, el comportamiento de J_{intra} puede ser explicado considerando dos mecanismos de anclaje diferentes: Para H bajo, la interacción entre los vórtices es insignificante y J_{intra} puede considerarse independiente de H. En este régimen, domina el anclaje fuerte de vórtices. En el régimen intermedio de H, aparece la interacción vórtice-vórtice. En este caso, domina el anclaje colectivo débil de vórtices.

La densidad de corriente crítica intergranular (J_c) se determinó de forma similar a J_{intra}, pero sólo para la muestra con r_g=1680 nm, esto debido a que el proceso de molienda al que fueron sometidas el resto de las muestras, afecta grandemente la calidad de las mediciones eléctricas. El bajo valor de $J_c = 6.56 \times 10^5$ A·m^{-2} es debido a la fragilidad de las uniones Josephson que acoplan los granos que forman la muestra. La densidad de corriente crítica de desacoplamiento (J_D) se calculó utilizando los valores de ξ_{eff} y λ_{eff} obtenidos previamente. Ésta resultó ser un orden de magnitud mayor que J_{intra}. Se encontró que J_D disminuye linealmente con el tamaño de partícula, cuando $r_g \sim \lambda$, mientras que para la muestra con mayor tamaño de partícula (r_g=1680 nm) alcanza su valor máximo (en volumen). Este es exactamente el mismo comportamiento observado para $H_{irr}^{1/3}$.

En general, se observa que los campos críticos, la longitud de coherencia y las corrientes críticas tienen magnitudes más pequeñas conforme el tamaño de partícula se hace cada vez más pequeño.

Desde el punto de vista tecnológico, el método de polvo en tubo (powder in-tube) se usa con frecuencia en la fabricación de cables superconductores, y es precisamente el tamaño de partícula el parámetro que determina las propiedades de estos. En este contexto, los resultados del presente trabajo son una contribución al entendimiento de los efectos que el tamaño de partícula tiene sobre las propiedades superconductoras de los cables fabricados a partir de polvo superconductor de $SmFeAsO_{1-x}F_x$.

Abstract

The present thesis is a study of the size effects on the superconducting behavior of iron-based $SmFeAsO_{1-x}F_x$ alloy. This work is focused on magnetization properties and how it evolves as the particle size is reduced. In first place, a randomly oriented polycrystalline sample of $SmFeAsO_{0.91}F_{0.09}$ was prepared by the one step method of solid state reaction. This was done by using hand-made milling. The phase identification was done by X-Ray diffraction (XRD), and confirms the very low presence of unwanted phases. The critical temperature (T_c) was determined by the transition observed in the Resistance-Temperature curve (R-T), indicating a T_c=56.1 K (M-T curves indicate 58.8 K). The fluorine content was determined by comparison, between the experimental T_c value and, the T_c-x phase diagram of samples synthesized in a similar way.

High quality sample was divided in six parts, and softly milled by hand over different time intervals, to obtain a set of samples with a variety of particle sizes: 1680 nm (unmilled), 550 nm, 470 nm, 405 nm, 345 nm and 220 nm. The range of size covers from bulk size (r_g = 1680 nm), until the scale of the penetration depth (220 nm). All samples kept the same crystalline structure (verified by XRD). The particle size was determined directly from SEM micrographs.

The magnetic characterization was done in a vibrating sample magnetometer (VSM). The present study is focused in the analysis of these measurements. The granular nature of the samples was stablished by the presence of a second transition fall around T=19 K, in the Magnetization-Temperature curves (M-T). On the other side, the virgin magnetization region was studied in the Magnetization-Magnetic Field curves (M-H). It was found that the lower critical field (H_{c1}), which limits the Meissner regime, exhibit a quadratic power law dependence on the particle size: $H_{c1} \sim r_g^2$, with values $30 \leq H_{c1} \leq 395$ Oe, for $220 \leq r_g \leq 1680$ nm. Moreover, the full penetration field (H^*), which limits the virgin magnetization region, follows a logarithmic law on r_g: $H^* = H_0(1 + \frac{r_g}{r_0})$, with constants H_0=709.97 Oe and r_0=178 nm. The experimental values are in the range $510 \leq H^* \leq 1570$ Oe, for $220 \leq r_g \leq 1680$ nm. The experimental results are in agreement with theoretical models of High Temperature Superconductors (HTS) previously reported.

The experimental values obtained for H_{c1} were used to calculate the effective coherence length (ξ_{eff}). It gets shorter as the particle size diminishes, following a quadratic power law: $\xi_{eff} \sim r_g^2$, with values in the range $0.37 \leq \xi_{eff} \leq 2.5$ nm, for $220 \leq r_g \leq 1680$ nm. In turn, these results suggest that the effective penetration depth (λ_{eff}) increases when $r_g \rightarrow 0$.

The irreversibility field (H_{irr}) was determined directly from M-H hysteresis loops, with values from 7.1 to 15.8 kOe, $220 \leq r_g \leq 1680$ nm. For particles with the same scale of λ ($220 \leq r_g$

≤ 550 nm), H_{irr} diminishes linearly with r_g, while for r_g = 1680 nm, it reaches a saturation value. This behavior is well represented by the small particle limit of the flux creep model. The values of H_{irr} were used to estimate H_{c2} on the basis of the mentioned model, , with values in the range $3.8 \leq H_{c2} \leq 22$ T, for $220 \leq r_g \leq 1680$ nm. The results are much lower than the ones proposed after the discovery of iron-based superconductors (IBSC), but are in agreement with the observed behavior of H_{irr} and recent studies.

The intragranular critical current density (J_{intra}) was determined directly form M-H curves. The critical current is determined by the magnetic vortex pinning and is composed by the sum of two components. Hence, the behavior of J_{intra} can be explained by considering two different pinning mechanisms: For low H, the interaction between vortices is negligible and J_{intra} can be considered independent of H. In this regimen, the strong vortex pinning dominates. In the intermediate regime of H, vortex-vortex interaction appears. In this case, the weak collective pinning dominates.

The intergranular critical current density (J_c) was determined in a similar way as J_{intra}, but only for the sample that was not ground to reduce its particle size (r_g=1680). The low value J_c= 6.56×10^5 A·m^{-2} is caused by the well-known weak-link problem associated with granularity. The depairing critical current density (J_D) was calculated by using the values of ξ_{eff} and λ_{eff} previously obtained. It results one order of magnitude bigger than J_{intra}. J_D decreases linearly with particle size ($r_g \sim \lambda$), while for big enough particles (r_g=1680 nm) it reaches its bulk value. This is the same behavior observed for $H_{irr}^{1/3}$.

In general, it is observed that critical fields, coherence length and critical currents have smaller magnitudes as particle size becomes smaller.

From the technological point of view, a technique commonly used in the manufacture of superconducting cables is the powder in-tube method, where the particle size is the main parameter that determines the superconducting properties of the cables. In this vein, the results of this work contribute to the knowledge of the influence of the particle size in the technical characteristics of cables made from superconducting powder of $SmFeAsO_{1-x}F_x$.

Contents

List of Figures

List of Tables

Introduction

The word *Nanoscience* comes from the Greek *nanos* which means *dwarf* and from the Latin voice *scientia* which means knowledge. In 1960 the prefix nano (n) was included in the International System of Units and defined as one billionth of something (10^{-9}), while the modern meaning of science refers to objective, structured and verifiable knowledge. Hence, Nanoscience is the study of Physics, Chemistry, and Biology that rules at small scale. This is one of the fastest growing branches of science at the beginning of the XXI century, due to a large number of possible technological applications.

Since the decade of 80´s, the miniaturization promotes the study of physical properties in small systems that can´t be considered anymore as macroscopic. This generated great interest in mesoscopic systems. Nevertheless, the development of techniques like scanning tunneling microscopy (STM), scanning electron microscopy (SEM), and atomic force microscopy (AFM), have allowed the observation and manipulation of materials at nanometric scale. The word *mesoscopic* comes from the Greek *mesos*, which means in the middle, and from *scopio*, which means to observe. This leaves the mesoscopic scale between the macro and nano scale.

Nanostructured materials, like nanoparticles, nanowires, nanodots and thin films, exhibit atypical physical and chemical properties. These unusual properties can be attributed to quantum size effects, the dimensionality of the sample or surface effects.

In a bulk material, the dimensions of the object are much larger than the range of the *interaction potential of atoms*. Hence, the boundaries do not interact locally inside the object (except at the borders). On the other side, nanoscale and mesoscopic materials have a large surface/volume ratio, and the range of the interaction potential of atoms is similar to the size of the object. Thus, the frontiers of the sample have a significant effect in the electron confinement, which gives rise to new phenomena.

The dimensionality is given by the size of the sample, for example, a material in bulk is considered 3-D, while a very thin film as a 2-D system. In the first case, the surface, interface and confinement effects are not considered because the length of the sample in any direction is too large and can be approximated to infinite. However, in a film sufficiently thin, the physical properties along the perpendicular direction will be dominated by quantum size and surface effects, while in the parallel directions the physical properties can be still approximated by those of the bulk material. A nanowire is a 1-D system, and the size effects will be dominant in the perpendicular direction while in the longitudinal one the system will be nearly boundless. Nanoparticles, clusters, colloids, nanocrystals and fullerenes are examples of 0-D systems, in which electrons are confined over all directions.

Quantum effects by reducing the size of a sample are observed in most of the physical properties of the materials, and superconductivity is not the exception. The present work considers particle sizes of hundreds of nanometers, a size range that permits to induce superconductivity, and studies the changes originated by the gradual reduction in the size of the sample.

Another effect of the reduced size is the increment of the total surface area. When a bulk material is reduced to small particles, the sum of the surface areas of all small particles will be so much higher than the surface area of the sample in bulk form. This can increase considerably the chemical reactivity of materials to the point that stable materials like aluminum can burn spontaneously at ambient conditions, making necessary the manipulation of chemical precursors under an inert atmosphere.

In a superconducting material, finite size effects can be observed in particles of mesoscopic size (like the particles used in this thesis). Size effects modify the Meissner state and the critical state, also known as vortex state. The critical fields and critical currents of a superconductor are determined by the penetration depth (λ) and the coherence length (ξ), both parameters identify the superconductor material and can vary from hundreds of nanometers to a few Angstrom (10^{-10} m), depending on the specific material. The influence of the effective size of the sample on the magnetic properties of superconductors has been established by theoretical and experimental works for a variety of superconducting materials of type I and type II.

This thesis is a complete study of the effects of reducing the particle size in superconducting polycrystalline powder samples of the iron-based superconductor $SmFeAsO_{1-x}F_x$. The realized work can be divided in three steps: fabrication of the superconducting samples, characterization of the morphological, electric and magnetic properties, and finally the analysis and interpretation of the experimental results.

At the beginning of this work, the effort was focused on the chemical synthesis of $SmFeAsO_{1-x}O_x$, via a solid-state reaction performed by grinding. Different stoichiometries and variables of the fabrication process were tested. After this it was possible to obtain a randomly oriented polycrystalline sample of $SmFeAsO_{0.91}F_{0.09}$. This sample has a high T_c, and a minimum presence of contaminant phases, verified by X-ray diffraction.

High quality sample was divided and softly ground by hand, over different time intervals, to obtain a set of samples with a variety of average sizes: 1680 nm (this sample was not ground to reduce its particle size), 550 nm, 470 nm, 405 nm, 345 nm and 220 nm. The range of size covers from bulk size (r_g = 1680 nm), to the scale of the penetration depth (220 nm).

The morphological and crystallographic properties of the samples were studied by X-ray diffraction (XRD) and Scanning Electron Microscopy (SEM). The electric properties were studied by four-probe resistance measurements (R-T). The main study of the present work is based on the size effects on the magnetic properties of the $SmFeAsO_{1-x}F_x$ superconductor. Therefore, the

magnetic characterization is the most important part in this thesis. This magnetic characterization encloses both magnetization vs. temperature (M-T) and isothermal magnetization (M-H).

The study includes the different regimes in a superconductor: Meissner state, virgin magnetization region, mixed state, and finally the upper critical field, which points to the loss of superconducting properties. By comparing the experimental results with some theoretical works, it was possible to find an explanation for the evolution of the main parameters of this superconductor: Meissner state, transition critical temperature (T_c), lower critical field (H_{c1}), full penetration field (H^*), penetration depth (λ), coherence length (ξ), irreversibility field (H_{irr}), upper critical field (H_{c2}), intergranular critical current density (J_c), intragranular critical current density (J_{intra}) and depairing critical current density (J_D).

1 A brief introduction to superconductivity

1.1 History of superconductivity

In 1894 H. Kamerlingh Onnes, who was a professor at Leiden University, began to experiment in helium liquefaction, becoming one of the pioneers in low-temperature physics. In 1908, his laboratory was the first in obtaining liquid helium (evaporation point is at 4.2 K), making accessible temperatures as low as 1 K. This achievement permitted Onnes to study the physical properties of a variety of materials at low-temperatures that before were inaccessible. In 1911, he found that *electrical resistance of mercury drops to zero at a temperature of 4.15 K, Onnes called this phenomenon superconductivity.* A year after, he found that a sufficiently strong magnetic field applied to the superconducting material reestablished the electrical resistivity. In 1913, Onnes and his colleagues found superconductivity in lead at a temperature of 7.2 K; that same year, Onnes received the Nobel prize for his work on helium liquefaction [1].

In 1933, Meissner and Ochsenfeld observed that the magnetic field is expelled from the inside of a superconductor, when it is cooled below its critical temperature in the presence of a weak external magnetic field [2]; this phenomenon is known as the Meissner-Ochsenfeld effect. The brothers Fritz and Heinz London, proposed the first phenomenological theory of superconductivity, in an effort to explain the Meissner effect, their results predict that the magnetic field is expelled from the bulk of the superconductor, but also that it penetrates a small distance inside the sample surface, known as the penetration depth [3].

In 1950, superconductivity was described by Vitali Ginzburg and Lev Landau, in a phenomenological theory of superconductivity based on thermodynamical principles, in which the phenomenon was considered a phase transition. The formulation of this phase transition is based in terms of an order parameter. The London theory of superconductivity is a special case of the Ginzburg-Landau theory of superconductivity [4]. In the same year, H. Fröhlich explained that two electrons can experience a net attractive potential each other when a crystal lattice distortion is considered. This is caused by the circulation of the electrons across the lattice [5]. At about the same time the isotopic effect was discovered, which consists in the inverse relation between the superconducting transition (T_c) and the atomic masses of the different isotopes of one single chemical element [6,7]. The isotopic effect establishes the influence of the crystal lattice in the superconducting phenomenon.

During various decades, along with chemical elements, many alloys were found to be superconductors. In 1953, superconductivity in V_3Si at 17.1 K; this material is part of the well know A15 group [8]. This new kind of materials was named as type II superconductors. The

compound V_3Si was among the materials with the highest T_c, until the discovery of copper based superconductors with a perovskite structure.

In 1957, Alexei Abrikosov solved the Ginzburg-Landau equations and found solutions that explain the magnetic flux penetration inside type II superconductors, which led to a magnetic flux lattice (Abrikosov lattice), inside this kind of materials [9].

Also, in 1957 John Bardeen, Leon Cooper, and John Robert Schrieffer developed the microscopic theory of superconductivity, known as BCS. Based on the Fröhlich results, they explained that the electron-phonon interaction causes a small attractive potential between electrons, which couple in pairs, with opposite spin and momentum, called Cooper pairs. The charge carrier in a supercurrent is the Cooper pair, which net spin is cero and is no more subjected to Pauli´s exclusion principle, so that, all Cooper pairs condensed in one single ground state [10,11]. This ground state is a superconducting state. Our current knowledge of the superconducting phenomenon is based on the BCS theory: However, it does not explain the physics of unconventional superconductors, like high T_c superconductors or the iron-based superconductors.

In 1959, Gor'kov proved that the phenomenological theory of Ginzburg-Landau is a special case of the microscopic BCS [12] theory. Nevertheless, the former is still very useful and in the present work, I try to explain some experimental results within terms of the Ginzburg-Landau theory.

A Josephson junction consists of two superconductors, separated by an insulator. In 1962, B.D. Josephson proposed that quantum tunneling can be possible for Cooper pairs [13]. The Josephson effect was experimentally observed by P.W. Anderson and J.M. Rowell [14]. In 1973, B. D. Josephson together with Leo Esaki and Ivar Giaever received the Nobel prize for their works, in the area of electron quantum tunneling. In 1974, another compound of the A15 group, Nb_3Ge, reached a T_c=23.2 K [15, 16], the highest until the discovery of superconductivity on cuprates. The first unconventional superconductor was found at the end of the same decade: $CeCu_2Si_2$ [17]. The physics involved in this kind of materials cannot be explained by the BCS or Bogolyubov theories.

William Little suggested in 1964, that organic superconductors would be possible [18]; however, it was not until 1980 that Klaus Bechgaard and his colleagues, found the first organic superconductor stable at standard pressure, $(TMTSF)_2PF_6$ [19], with a T_c=0.9 K.

The β-$(BEDT\text{-}TTF)_2I_3$, a second family of organic superconductors, was discovered in 1984 [20]. Two years later, in 1986, J.G. Bednorz and K.A. Müller find superconductivity in $Ba_xLa_{5-x}Cu_5O_{5(3-y)}$ and at the same time discover a new family of superconducting compounds based on copper and oxygen usually named cuprates [21]. LaBaCuO has a T_c= 30 K, which is higher than the previous highest T_c= 23.2 K of Nb_3Ge. Later, both scientists received the Nobel prize by the discovery of superconductivity in ceramic materials. In the same year, the compound $YBa_2Cu_3O_{7-x}$

reached a T_c=93 K, that was the first time that a superconducting critical temperature exceeded the boiling point of liquid nitrogen [22].

In 1991, superconductivity was found in fullerenes K_3C_{60} reached a T_c=18 K [23]. Only two years later, $HgBa_2Ca_2Cu_3O_{8+\delta}$ was developed. In the next year, this material established the current record of T_c=135 K [24].

The first conventional high T_c superconductor appeared in 2001, MgB_2, with a T_c=39 K [25] at normal pressure conditions, this critical temperature is one of the highest for a non-cuprate or iron-based superconductor. In 2003, Abrikosov and Ginzburg received the Nobel prize for their contributions to the Ginzburg-Landau-Abrikosov-Gor'kov theory.

In 2006, Hideo Hosono, Yoichi Kamihara and collaborators discovered superconductivity in LaOFeP at temperatures under 5 K. This material belongs to a recently discovered family known as oxypnictides or iron pnictide compounds [26, 27]. Nowadays, the study of iron-based superconductors is an active research topic that could give clues about the nature of superconductivity in High-Temperature superconductors. In the specific case of $SmFeAsO_{1-x}F_x$, it is possible to obtain samples with superconducting critical temperatures over 56 K, the high T_c facilitates the observation of size effects on the superconducting properties. The superconductivity group at Physics Department of CINVESTAV, started to study this family of superconductors since 2011 and the present thesis is part of that effort.

1.2 Basic concepts in superconductivity

Superconductivity is a physical phenomenon consisting of the complete loss of electrical resistivity (see Figure 1-1) and the expulsion of a magnetic field from the bulk of the material. The transition from normal to the superconducting state takes place when the material is cooled until the transition critical temperature (T_c) is reached (or lower temperatures), then the superconducting properties appear. The material returns to the normal state if: the temperature exceeds T_c, the sample is immersed in a strong enough magnetic field, called the *critical magnetic field* (H_c), or if a sufficiently high electrical current flows across the material, known as the critical current (J_c).

Commonly the superconductors behave like normal metals in the normal state, but they are not so good electrical conductors (for example, lead, tantalum, and tin). Good electrical conductors like gold, silver or copper never turn into superconductors. Moreover, as commented before, superconductors expel the magnetic field, so they are perfect diamagnetic materials (ideal case), but in the normal state they follow a paramagnetic behavior. The magnetic induction (B) inside any material is (in CGS units):

$$B= H+4\pi M \tag{1.1}$$

If the material is in the superconducting state and the Meissner effect occurs, then: B=0 (1.2)

Substituting Eq. (1.2) in (1.1): $0= H+4\pi M$,

$$H= -4\pi M \quad (1.3)$$

As can be seen in eq. (1.3), a superconductor has negative magnetization (M), so the material is *diamagnetic* and therefore the magnetic susceptibility is negative. Considering the usual relationship between the applied field H and the magnetization:

$$B= H+4\pi(\chi H); \qquad B=0,\ M=\chi H.$$

$$0= H(1+ 4\pi\chi)$$

$$0= 1+ 4\pi\chi$$

$$1= -4\pi\chi \quad (1.4)$$

If the superconductor is in the Meissner state, then $\chi= -1$ and the material presents perfect diamagnetism.

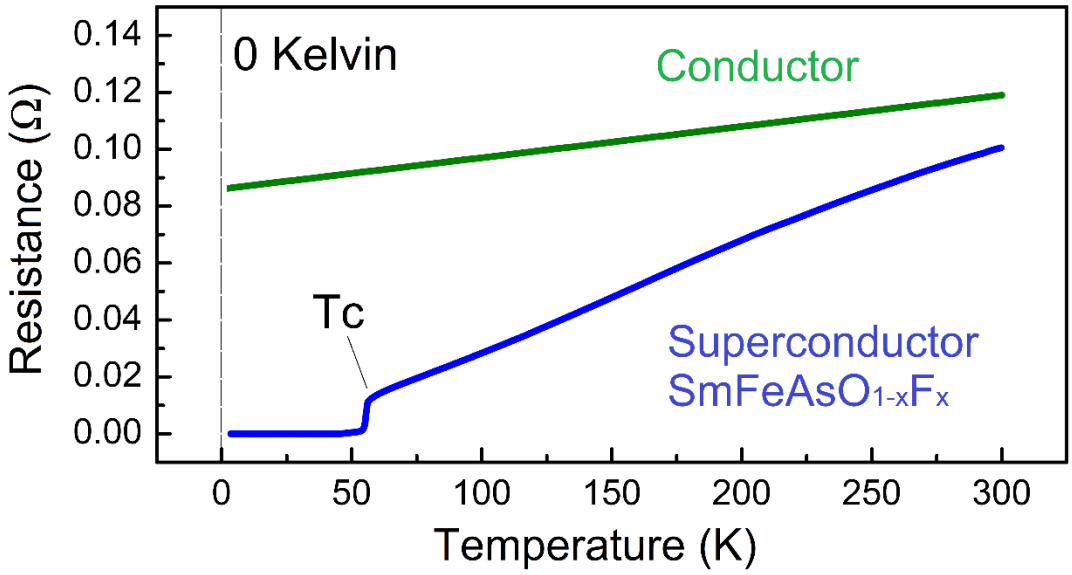

Figure 1-1. Resistance vs. Temperature curve.
In green, the typical R-T curve of an ordinary conductor like cooper; the electrical resistivity falls linearly as T → 0 K. However, the material never reaches the null electrical resistance. In blue, the compound $SmFeAsO_{1-x}F_x$. It follows the same behavior until temperature falls to T_c. Then, the electrical resistance sharply falls to zero, and the material enters to the superconducting state.

The magnetic response is not the same for all superconducting materials. Some of them lose their superconducting properties, in a sharp fall at a value H_c (see Fig. 1-2); these materials are called type I superconductors. When applying an external magnetic field H, the superconductor is in the Meissner state, and presents perfect diamagnetism, but when $H \geq H_c$ the material loses its superconducting properties and **M** falls to zero, even if the material is at T

< T_c. On the other side, *type II superconductors initially show the same perfect diamagnetism, but present two critical fields: at the lower critical field (H_{c1}) the material loses the Meissner state, but there is not a sharp fall of M; instead of that, the material remains as a superconductor, and M suffers a smooth fall, until H reaches the upper critical field (H_{c2}) (see Fig. 1-2) and the material finally returns to the normal state.* The region bounded by H_{c1} and H_{c2} is known as the mixed or vortex state. Iron-based superconductors, like $SmFeAsO_{1-x}F_x$, belong to this kind of superconducting materials.

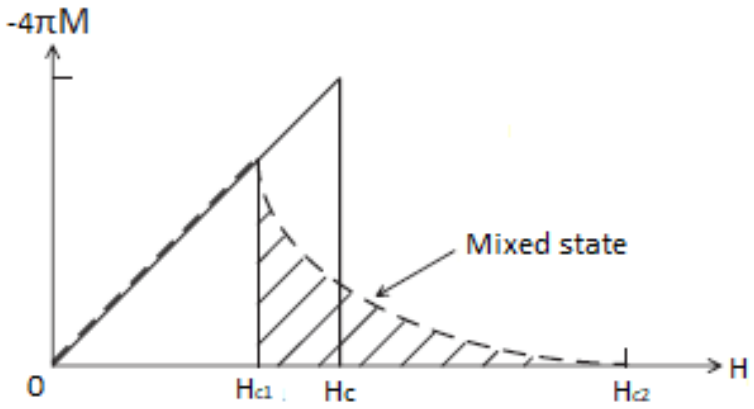

Figure 1-2. Reversible magnetization of type I and type II superconductors.
M-H graph of type I and type II superconductors. The solid line illustrates the reversible magnetization of type I superconductors. The dashed line illustrates the corresponding to type II superconductors. The striped region indicates the mixed state of type II superconductors.

As explained before, a superconductor in a Meissner state, expels the magnetic field from within, consequently, there are no currents in the bulk of the sample. Perfect diamagnetism is maintained in the bulk by surface currents, which produces a magnetic field in an orientation that cancels the magnetic flux inside the sample. The latter are called *supercurrents* and are confined to a thin shell on the surface of the material. The width of this shell, where the supercurrents flow, is known as the *penetration depth* (λ). Thus, λ measures the depth that H penetrates inside the material. It is usually expressed in length units (nm). The small scale of λ makes macroscopic samples appear as perfectly diamagnetic.

The concept of coherence length arises from the solution of the Ginzburg-Landau equations [28]. It was also proposed by Pippard [29] to introduce nonlocal effects in superconductivity. He proposed that the density of superconducting electrons n_s, (Copper pairs were unknown at that time), varies slowly with position, so appreciable changes in n_s occur within a distance that he called *coherence length* (ξ). From the point of view of the Ginzburg-Landau theory, ξ can be defined as the length in which the wave function of the Cooper pairs (ψ) decays from its bulk´s value to zero.

As we have already mentioned, there are two general kinds of superconductors; they are identified by the value of the Ginzburg-Landau parameter: $\kappa = \lambda/\xi$. In type I superconductors $\kappa <$

$1/\sqrt{2}$ (see Fig. 1-3.a). For type II superconductors $\kappa > 1/\sqrt{2}$ (see Fig. 1-3.b) The material $SmFeAsO_{1-x}F_x$ has a pronounced type II behavior characterized by $\kappa >> 1/\sqrt{2}$.

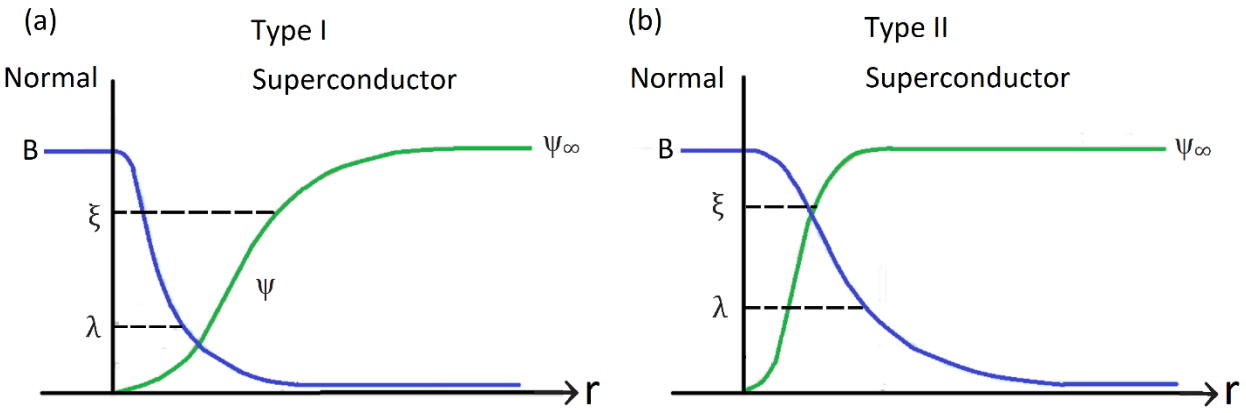

Figure 1-3. Penetration depth (λ) and coherence length (ξ). Type I and II superconductors.
a) Penetration depth (λ) and coherence length (ξ) in a type I superconductor. λ measures the depth that the applied magnetic field reach inside the material. ξ measures the length necessary for the order parameter ψ, to go from its bulk value ψ_∞ to zero. b) Type II superconductor, notice that λ > ξ.

1.3 Bibliography

The information in section 1.2. Basic concepts in superconductivity, is treated in the book:

A.C. Rose-Innes, E.H. Rhoderick. Introduction to superconductivity. Chapter. 2.4. Penetration depth. Pergamon. Second edition. 1994.

[1] R. de Bruyn Ouboter, Superconductivity: Discoveries during the early years of low-temperature research at Leiden 1908–1914, IEEE Trans. Magn., 23, 355–370 (1987).

[2] Meissner, W., Ochsenfeld, R. Ein neuer Effekt bei Eintritt der Supraleitfähigkeit. Naturwissenschaften 21, 787–788 (1933). https://doi.org/10.1007/BF01504252.

[3] F. London and H. London, Supraleitung und Diamagnetismus, Physica, 2, 341-354 (1935). https://doi.org/10.1016/S0031-8914(35)90097-0.

[4] V.L. Ginzburg, Nobel lecture: On superconductivity and superfluidity (what I have and have not managed to do) as well as on the "physical minimum" at the beginning of the XXI century, Rev. Mod. Phys., 76, 981–998 (2004). https://doi.org/10.1103/RevModPhys.76.981.

[5] H. Fröhlich. Theory of the Superconducting State. I. The Ground State at the Absolute Zero of Temperature. Phys. Rev. 79 845 (1950). https://doi.org/10.1103/PhysRev.79.845.

[6] E. Maxwell. Isotope Effect in the Superconductivity of Mercury. Phys. Rev. 78, 477 (1950). https://doi.org/10.1103/PhysRev.78.477.

[7] C. A. Reynolds, B. Serin, W. H. Wright, and L. B. Nesbitt. Superconductivity of Isotopes of Mercury. Phys. Rev. 78, 487 (1950). https://doi.org/10.1103/PhysRev.78.487.

[8] G.F. Hardy and J.D. Hulm. Superconducting silicides and germanides. Phys. Rev., 89, 884 (1953). https://doi.org/10.1103/PhysRev.89.884.

[9] A.A. Abrikosov. On the magnetic properties of superconductors of the second group. Sov. Phys.– JETP, 5, 1174–1182 (1957).

[10] J. Bardeen, L.N. Cooper, and J.R. Schrieffer. Microscopic theory of superconductivity. Phys. Rev. 106, 162–164 (1957). https://doi.org/10.1103/PhysRev.106.162.

[11] J. Bardeen, L.N. Cooper and J.R. Schrieffer. Theory of superconductivity. Phys. Rev. 108, 1175–1204 (1957). https://doi.org/10.1103/PhysRev.108.1175.

[12] L.P. Gor'kov. Microscopic derivation of the Ginzburg-Landau equations in the theory of superconductivity. Sov. Phys.– JETP, 9, 1364–1367 (1959).

[13] B. D. Josephson. Possible new effects in superconductive tunneling. Phys. Lett. 1, 251 (1962). https://doi.org/10.1016/0031-9163(62)91369-0.

[14] P. W. Anderson; J. M. Rowell (1963). "Probable Observation of the Josephson Tunnel Effect". Phys. Rev. Lett. 10 (6). https://doi.org/10.1103/PhysRevLett.10.230.

[15] L.R. Testardi, J.H.Wernick, and W.A. Royer. Superconductivity in Nb3Ge films above 22 K. Appl. Phys. Lett., 23, 480–482 (1973).

[16] L.R. Testardi, J.H.Wernick, and W.A. Royer. Superconductivity with onset above 23K in Nb-Ge sputtered films. Solid State Commun., 15, 1–4 (1974).

[17] F. Steglich, J. Aarts, C. D. Bredl, W. Lieke, D. Meschede, W. Franz, and H. Schäfer. Superconductivity in the Presence of Strong Pauli Paramagnetism: $CeCu_2Si_2$. Phys. Rev. Lett. 43 (25): 1892–1896. Doi:10.1103/PhysRevLett.43.1892.

[18] Little W.A. Possibility of Synthesizing an Organic Superconductor. Phys. Rev. 134, A1416 (1964). https://doi.org/10.1103/PhysRev.134.A1416.

[19] D. Jérome, A.Mazaud, M. Ribault, and K. Bechgaard. Superconductivity in a synthetic organic conductor (TMTSF)2PF6. J. Phys. Lett., 41, 201–204 (1980).

[20] E. B. Yagubskii, I.F. Shchegolev, V.N. Laukihin, L. Buravov. Pis'ma Zh. Eksp. Teor. Fiz.1984,39, 12. JETP Lett. 39:12 (1984).

[21] J.G. Bednorz and K.A. Müller. Possible high Tc superconductivity in the Ba–La–Cu–O system. Z. Phys. B, 64, 189–193 (1986). https://doi.org/10.1007/BF01303701.

[22] M.K. Wu, J.R. Ashburn, C.J. Torng, P.H. Hor, R.L. Meng, L. Gao, Z.J. Huang, Y.Q.Wang, and C.W. Chu. Superconductivity at 93K in a new mixed-phase, Y–Ba–Cu–O compound system at ambient pressure. Phys. Rev. Lett., 58, 908–910 (1987). https://doi.org/10.1103/PhysRevLett.58.908.

[23] A.F. Hebard, M.J. Rosseinsky, R.C. Haddon, D.W. Murphy, S.H. Glarum, T.T.M. Palstra, and A.P. Ramirez. Superconductivity at 18K in potassium-doped C60. Nature, 350, 600–601 (1991). https://doi.org/10.1038/350600a0.

[24] J.J. Capponi, J.L. Tholence, C. Chaillout, M. Marezio, P. Bordet, J. Chenavas, S.M. Loureiro, E.V. Antipov, E. Kopnine, M.F. Gorius, M. Nunez-Regueiro, B. Souletie, P. Radaelli, and F. Gerhards. High pressure synthesis and properties of the $HgBa_2Ca_{n-1}Cu_nO_{2n+2+\delta}$ (n=1–6). Physica C, 235–240, 146–149 (1994). https://doi.org/10.1016/0921-4534(94)91334-X.

[25] J. Nagamatsu, N. Nakagawa, T. Muranaka, Y. Zenitani, and J. Akimitsu. Superconductivity at 39 K in magnesium diboride. Nature, 410, 63–64 (2001). https://doi.org/10.1038/35065039.

[26] Yoichi Kamihara, Hidenori Hiramatsu, Masahiro Hirano, Ryuto Kawamura, Hiroshi Yanagi, Toshio Kamiya, Hideo Hosono. Iron-Based Layered Superconductor: LaOFeP. J. Am. Chem. Soc. 128 (31): 10012–10013. (2006). Doi:10.1021/ja063355c.

[27] Yoichi Kamihara, Takumi Watanabe, Masahiro Hirano, Hideo Hosono. Iron-Based Layered Superconductor $La[O_{1-x}F_x]FeAs$ (x = 0.05–0.12) with T_c = 26 K. Journal of the American Chemical Society. 130 (11): 3296–3297. (2008). Doi:10.1021/ja800073m.

[28] V. Ginzburg, L. Landau. On the Theory of superconductivity (In Russian). Zh. Eksp. Teor. Fiz. 20, 1064. (1950).

[29] A.B. Pippard. The coherence concept in superconductivity. Physica 19, 765-774 (1953). https://doi.org/10.1016/S0031-8914(53)80085-6.

2 Phenomenological theories in superconductivity

2.1 London theory of superconductivity

The Maxwell equations are insufficient to explain the magnetic state of a superconductor, for that reason, in 1935 Fritz and Heinz London proposed a theory that explains the Meissner effect [1]. In this phenomenological theory appeared the concept of *penetration depth of the magnetic field* inside a superconductor. The London theory is based on the *Two-fluid model*, proposed by C.J. Gorter and H.G.B. Casimir [2], in 1934. In this model, the free electrons in the crystal lattice are divided into two fluids, one composed by normal electrons, and the other composed by superconducting electrons. The normal fluid follows Ohm´s law: $\mathbf{J}_n = \sigma_n \mathbf{E}$, and the Drude model that determines the electrical conductivity: $\sigma_n = e^2 n_n \tau / m$, where the subscript n indicates normal state and n, τ, and m are the charge carriers' density, average dispersion time and the electron mass, respectively. The superconducting electrons, (at that time the Cooper pairs were an unknown concept), were proposed as a superfluid, no matter their fermionic nature, so electrons undergo a free acceleration related to the electric force[1]:

$$\boldsymbol{F}_e = m^* \frac{d\boldsymbol{v}_s}{dt} = -e^* \boldsymbol{E} \tag{2.1}$$

and the current density is given by

$$\boldsymbol{J}_s = -e^* n_s \boldsymbol{v}_s \tag{2.2}$$

The London brothers proposed that the magnetic field, in fact, penetrates a small depth inside the superconductor, calling it, the *penetration depth* (λ). With this idea, they deduced two equations which describe the electrodynamic properties of superconductors [1]. By taking the derivative of eq. (2.2):

$$\frac{d\boldsymbol{J}}{dt} = -e^* n_s \frac{d\boldsymbol{v}_s}{dt} \overset{from\ (2.1)}{\triangleq} \frac{e^{*2} n_s \boldsymbol{E}}{m^*} \tag{2.3}$$

Leaving $\boldsymbol{E}$ alone in the left side:

$$\boldsymbol{E} = \frac{m^*}{e^{*2} n_s} \frac{d\boldsymbol{J}}{dt} \tag{2.4}$$

This is the *First London equation*, where it was assumed that n_s and n_n are uniform and stationary (constant in space and time).

To explain the Meissner effect, the London brothers postulated the *Second London Equation*:

$$-\boldsymbol{B} = \frac{m^* c}{e^{*2} n_s} (\nabla \mathrm{X}\, \mathbf{J}) \tag{2.5}$$

[1] In this thesis CGS units are used, unless otherwise stated.

which implies that the previous history of the system does not matter (field cooling or zero field cooling), and the magnetic flux inside the sample always will be null. To account for the magnetic flux inside the sample, as in type II superconductors, it was necessary to wait for the Ginzburg-Landau equations. Equation (2.5) leads to the equation that determines the spatial variations of the magnetic induction $\boldsymbol{B}$ and the current density $\boldsymbol{J}$ in the superconductor. Using: $\boldsymbol{B} = \boldsymbol{H} - \cancel{4\pi \boldsymbol{M}}$ in Maxwell´s equation $\nabla \mathrm{X}\, \mathbf{H} = \frac{4\pi}{c}\boldsymbol{J} + \cancel{\frac{\partial \boldsymbol{D}}{\partial t}}$, it leads to: $\nabla \mathrm{X}\, \boldsymbol{B} = \frac{4\pi}{c}\boldsymbol{J}$ (2.6).

Putting the curl of eq. (2.6) in eq. (2.5): $-\boldsymbol{B} = \frac{m^* c}{e^{*2} n_s}\frac{c}{4\pi}[\nabla \mathrm{X}\, (\nabla \mathrm{X}\, \boldsymbol{B})]$ (2.7)

But, $\nabla \mathrm{X}\, (\nabla \mathrm{X}\, \boldsymbol{B}) = \nabla\, (\nabla \cdot \boldsymbol{B}) - \nabla^2 \boldsymbol{B} = -\nabla^2 \boldsymbol{B}$, hence eq. (2.7) is rewritten as:

$$\boldsymbol{B} = \frac{m^* c^2}{4\pi e^{*2} n_s}\nabla^2 \boldsymbol{B} \tag{2.8}$$

The square of the *London penetration depth* can be defined as[2]:

$$\lambda_L^2 = \frac{m^* c^2}{4\pi e^{*2} n_s} = \frac{m c^2}{8\pi e^2 n_s} \tag{2.9}$$

where nowadays[3] we know that m^* is twice the mass of the electron (m), and e^* is twice the electron´s charge (e). Thus, eq. (2.9) allows rewriting eq. (2.8) to obtain:

$$\nabla^2 \boldsymbol{B} = \frac{\boldsymbol{B}}{\lambda_L^2} \tag{2.10}$$

This equation describes the spatial variation of the magnetic induction inside the superconductor (see Fig. 2.1), $\boldsymbol{B}$ penetrates to a depth λ inside the sample.

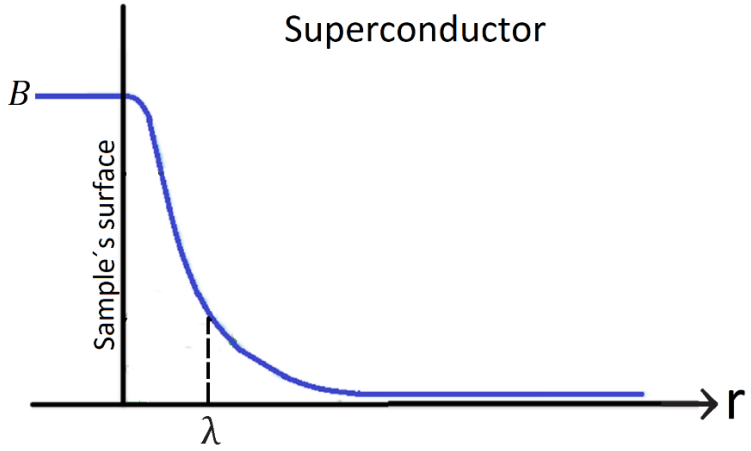

Figure 2-1. London penetration depth.

The figure illustrates the penetration of the magnetic flux, in the region near the surface of the sample. $\boldsymbol{B}$ penetrates to a depth λ inside the sample.

[2] In SI units: $\lambda_L^2 = \frac{m}{2\mu_0 e^2 n_s}$.

[3] When the London brothers proposed their theory, it was unknown that in the superconducting state the electrons are coupled in pairs (Cooper pairs).

From the definition of λ_L, The *First London equation* (2.4) can be rewritten as:

$$\boldsymbol{E} = \frac{4\pi\,\lambda_L^2}{c^2}\left(\frac{d\boldsymbol{J}}{dt}\right) \tag{2.11}$$

This is an equation for the evolution of the current density. Also, the *Second London equation* (2.5) can be rewritten as:

$$-\boldsymbol{B} = \frac{4\pi\,\lambda_L^2}{c}(\nabla \mathrm{X}\,\boldsymbol{J}) \tag{2.12}.$$

The First and the Second London equations are summarized by:

$$\boldsymbol{J} = -\frac{e^{*2}n_s}{m^*c}A \tag{2.13}$$

where A *is the magnetic vector potential*. Equation (2.4) can be derived taking the temporal derivative of eq. (2.13). The Second London equation (eq. 2.5) is derived by taking the curl of eq. (2.13) and using $\boldsymbol{B} = \nabla \mathrm{X}\,\boldsymbol{A}$. Finally, it is possible to find an equation that describes the spatial variation of the current density inside the superconductor (see appendix A).

$$\nabla^2\boldsymbol{J} = \frac{\boldsymbol{J}}{\lambda_L^2} \tag{2.14}.$$

This equation is an analogue to Eq. 2.10, and describes the spatial variation of electrical current density, in the superconductor material.

The London theory was the first successful approximation to the electrodynamics of a superconductor. Moreover, this theory introduced the concept of penetration depth, which is a fundamental parameter of any superconductor material. Later studies found deviations between experimental penetration depth and the value predicted by London (λ_L), and also a temperature dependence of λ. Even if the London brothers considered λ_L as a constant, it was the first time that a theory accounted for the role of a length scale in the superconducting properties.

2.2 Ginzburg-Landau theory of superconductivity

The Ginzburg-Landau theory was proposed in 1950 [3], this theory describes superconductivity from a phenomenological point of view, as a phase transition. The density of superconducting electrons is the order parameter used to describe superconductivity, (the concept of Cooper pair was unknown when the theory was proposed). The first postulate was:

$$\eta_s = \begin{cases} 0, & T > T_c \\ \neq 0, & T \leq T_c \end{cases} \tag{2.15}$$

or, by normalizing the order parameter:

$$\eta_2 = \begin{cases} 0, & T > T_c \\ 1, & T \leq T_c \end{cases} \tag{2.16}$$

where, by considering quantum mechanics concepts, $\eta_s = |\psi|^2$ and $\psi(r) = |\phi(r)|e^{i\phi(r)}$ is the wave function of the superconducting electrons. In fact, η_s=1 for $T << T_c$ and falls slowly to 0 as T tends to T_c, so that the total amount of electrons in the material is: $\eta_T = \eta_n - \eta_s$. On the other hand, near T_c, η_s tends approximates to 0 and *the thermodynamic free energy can be expanded in a power series of the order parameter* ψ:

$$F_s = F_{n0} + \alpha|\psi|^2 + \frac{\beta}{2}|\psi|^4 + \frac{|(-i\hbar\nabla - (e^*\mathbf{A}/c))\,\psi|^2}{2m^*} + \frac{\boldsymbol{H}^2}{8\pi} \tag{2.17}$$

where the energy of the electrons coupled to a magnetic field and the energy of the field itself are included. F_{n0} is the free energy density of the system in the normal state, with no magnetic field applied. $\alpha|\psi|^2 + \beta|\psi|^4$ is the series expansion for ψ. The last two terms of equation 2.17 are present only if there is an applied magnetic field, $\frac{\boldsymbol{H}^2}{8\pi}$ is the energy of the applied field and the remaining term is the energy of the canonical momentum, which is composed by the kinetic moment $-i\hbar\nabla$ and the magnetic moment $e^*\mathbf{A}/c$, where the vector potential $\mathbf{A}$ is defined as $B = \nabla \times \mathbf{A}$ The term[4] e^* is twice the electron charge, and m^* is twice the electron mass i.e., the mass of one Cooper pair. On the other hand, ψ is a complex function and ψ^* represents the conjugated of the Cooper pairs wave function. Now, let´s first consider the case of no applied magnetic field. With the purpose to find the equilibrium conditions of the ground state, it is necessary to take the derivative of 2.17 and made it equal to zero:

$$\frac{\partial}{\partial\psi^*}(F_s - F_{n0}) = \frac{\partial}{\partial\psi^*}(\alpha\psi\psi^* - \tfrac{\beta}{2}\psi^2\psi^{*2}) = \alpha\psi - \beta|\psi^2|\psi \tag{2.18}$$

$$= \psi(\alpha - \beta|\psi^2|) = 0 \tag{2.19}$$

Equation 2.19 has two solutions, ψ=0, and so, η_s=0 and the system is in the normal state. The second solution is:

$$\alpha - \beta|\psi^2| = 0 \;\Rightarrow -\frac{\alpha}{\beta} = |\psi^2| \tag{2.20}$$

$|\psi|^2$ is always positive, so α or β must have opposite signs. Further, these parameters are expressed in terms of the critical field and λ. Let´s choose α < 0 and β > 0. Then, the solution $|\psi|^2 = \frac{-\alpha}{\beta}$ is acceptable. The magnitude of $|\psi|^2$ varies, reaching a maximum inside the bulk in the absence of magnetic field. This maximum is called ψ_∞. Now, using eq. 2.20 in eq. 2.17 (there is no applied magnetic field), leading to the free energy density in the equilibrium state:

$$F_s - F_{n0} = \alpha|\psi|^2 + \tfrac{\beta}{2}|\psi|^4 = \alpha(\tfrac{-\alpha}{\beta}) + \tfrac{\beta}{2}(\tfrac{-\alpha}{\beta})^2 = -\frac{\alpha^2}{2\beta} \tag{2.21}$$

On the other side, superconductivity is destroyed in the presence of an intense magnetic field. This is called the *thermodynamic critical field* H_c, and its magnitude depends on the specific material. H_c is related to the free energy difference between the superconducting and normal

[4] When Ginzburg and Landau proposed their theory, it was unknown that in the superconducting state, the electrons are coupled in pairs, called Cooper pairs.

states, at zero field conditions. This energy is known as the *condensation energy density* (F^{conden}), the energy released when normal electrons pass to the superconducting state. Thus, it is possible to equal the energy associated with holding the magnetic field out the superconductor $\left(\frac{H_c^2}{8\pi}\right)$ with the condensation energy density (F^{conden}):

$$F^{conden} = F_{n0} - F_s = \frac{H_c^2}{8\pi} \tag{2.22}$$

Therefore, the superconducting state has a lower free energy, compared to the normal state. In fact, eq. (2.22) is the maximum difference between the free energy densities of the normal, and the superconducting state. Using eq. (2.22) and eq. (2.21), the thermodynamic critical field can be expressed in terms of the *parameters* α *and* β:

$$\frac{H_c^2}{8\pi} = \frac{\alpha^2}{2\beta} \tag{2.23}$$

The temperature dependence of the free energy, can be obtained by expanding α=α(T) around T_c and taking the first order term: α(T)= α´(t-1), with α´> 0 and t= T/T_c. Putting this into eq. 2.20:

$$|\psi|^2 = \frac{-\alpha}{\beta} = \frac{-\alpha'(t-1)}{\beta} = \frac{\alpha'(1-t)}{\beta} \tag{2.24}$$

If the penetration depth λ is defined in terms of the superconducting electrons density η_S, it is possible to determine the values of α and β. Taking eq. (2.9): $\lambda^2 = \frac{mc^2}{8\pi\eta_s e^2} = \frac{mc^2}{8\pi|\psi|^2 e^2}$, with η_s=|ψ|^2.

Then,

$$|\psi|^2 = \frac{mc^2}{8\pi\lambda^2 e^2} \tag{2.25}$$

On the other side, from eq. 2.20: $|\psi|^2 = \frac{-\alpha}{\beta}$, $\Rightarrow \alpha = -\beta|\psi|^2$.

Moreover, from eq. 2.23:

$$\beta = \frac{-4\pi\alpha^2}{H_c^2} \tag{2.26}$$

Then:

$$\alpha = -\frac{-4\pi\alpha^2}{H_c^2}|\psi|^2 \tag{2.27}$$

But $\eta_S = |\psi|^2$, $\Rightarrow\ 0 = \alpha(1 - \frac{4\pi\alpha\eta_s}{H_c^2})\ \Rightarrow\ \alpha = \frac{H_c^2}{4\pi\eta_s}$. As pointed out above, form eq. (2.9) η_s = |ψ|^2= mc^2/8πe^{2}λ^2. Thus, the value of α becomes:

$$\alpha = \frac{2H_c^2 e^2\lambda^2}{mc^2} \tag{2.28}$$

where H_c and λ depend on temperature. To obtain the value of β, substitute eq. (2.28) in eq. (2.26):

$$\beta = \frac{-4\pi\alpha^2}{H_c^2} = \frac{-4\pi}{H_c^2}\left(\frac{2H_c^2 e^2\lambda^2}{mc^2}\right) = \frac{-16\pi H_c^2 e^4\lambda^4}{m^2c^4} \tag{2.29}$$

2.2.1 **Ginzburg-Landau equations with an applied magnetic field.**

The free energy of a superconductor immersed in a magnetic field is given by eq. 2.17, with all its terms:

$$F_s - F_{n0} = \alpha|\psi|^2 + \frac{\beta}{2}|\psi|^4 + \frac{|(-i\hbar\nabla - (e^*A/c))\,\psi|^2}{2m^*} + \frac{H^2}{8\pi}$$

As it is known, the system tends naturally to the state of minimum energy. It has been mentioned before, that the normal state has a higher free energy compared to the superconducting state. This minimum energy state corresponds precisely to the superconducting state. With the purpose to find the minimum of the free energy, it is necessary to derive with respect to the vector potential A and setting it equal to 0.

$$\frac{\delta}{\delta \boldsymbol{A}}(F_s - F_{n0}) = \frac{\delta}{\delta \boldsymbol{A}}\left(\alpha|\psi|^2 + \frac{\beta}{2}|\psi|^4 + \frac{\left|\left(-i\hbar\nabla - \left(\frac{e^*\mathbf{A}}{c}\right)\right)\psi\right|^2}{2m^*} + \frac{H^2}{8\pi}\right) = \frac{\delta}{\delta \boldsymbol{A}}\frac{|(-i\hbar\nabla - (e^*\mathbf{A}/c))\,\psi|^2}{2m^*} + \frac{\delta}{\delta \boldsymbol{A}}\frac{H^2}{8\pi}=0 \tag{2.30}$$

After some manipulation (see appendix B), the first term of this expression can be rewritten as:

$$\frac{\delta}{\delta \boldsymbol{A}}\frac{|(-i\hbar\nabla - (e^*\mathbf{A}/c))\,\psi|^2}{2m^*} = \left[\frac{-i\hbar e^*}{2m^*c}(\psi\cdot\nabla\psi^* - \psi^*\cdot\nabla\psi) + \frac{2e^{*2}|\psi|^2\boldsymbol{A}}{2m^*c^2}\right]\cdot\frac{\delta \boldsymbol{A}}{\delta \boldsymbol{A}} \tag{2.31}$$

On the other side, the second term in Eq. 2.30 can be developed as follows:

$$\frac{\delta}{\delta \boldsymbol{A}}\frac{H^2}{8\pi} = \frac{\delta}{\delta \boldsymbol{A}}\frac{(\nabla X\boldsymbol{A})^2}{8\pi} = \frac{1}{4\pi}\,(\nabla X\boldsymbol{A})\cdot\left(\nabla X\frac{\delta \boldsymbol{A}}{\delta \boldsymbol{A}}\right) \tag{2.32}$$

Equations 2.31 and 2.32 can be substituted in Eq. 2.30:

$$0 = \left[\frac{-i\hbar e^*}{2m^*c}(\psi\cdot\nabla\psi^* - \psi^*\cdot\nabla\psi) + \frac{e^{*2}|\psi|^2\boldsymbol{A}}{m^*c^2}\right]\cdot\frac{\delta \boldsymbol{A}}{\delta \boldsymbol{A}} + \frac{[(\nabla XA)\cdot\left(\nabla X\frac{\delta \boldsymbol{A}}{\delta \boldsymbol{A}}\right)}{4\pi} \tag{2.33}$$

Where $(\nabla X\boldsymbol{A})\cdot\left(\nabla X\frac{\delta \boldsymbol{A}}{\delta A}\right) = \frac{\delta \boldsymbol{A}}{\delta A}\cdot[\nabla X(\nabla X\boldsymbol{A})]$, by using the vector identity: $\nabla\cdot(\vec{C}\,\mathrm{XB}) = \vec{B}^{\,\nabla X\boldsymbol{A}}_{\frac{\delta \boldsymbol{A}}{\delta A}}\cdot(\nabla\mathrm{XC}) - \mathrm{C}\cdot(\nabla\mathrm{XB})$. This simplification leads to:

$$\nabla X(\nabla X\boldsymbol{A}) = \frac{2\pi i\hbar e^*}{m^*c}(\psi\cdot\nabla\psi^* - \psi^*\cdot\nabla\psi) - \frac{4\pi e^{*2}|\psi|^2\boldsymbol{A}}{m^*c^2} \tag{2.34}$$

Nowadays, we know that the "superconducting electrons" are in fact Cooper pairs of electrons, and e^*= 2e and m^*= 2m. Moreover, by taking the right member of this expression equal to the current density in the superconductor, eq. (2.34) takes the form of the Ampère equation: $\nabla X(\nabla X\boldsymbol{A}) = \frac{4\pi}{c}\boldsymbol{J}$. Hence, the final form of the *First Ginzburg-Landau equation* is:

$$\boldsymbol{J} = \frac{ie\hbar}{2m}(\psi\cdot\nabla\psi^* - \psi^*\cdot\nabla\psi) - \frac{2e^2|\psi|^2\boldsymbol{A}}{mc} \tag{2.35}$$

This equation determines the current density inside a superconducting material, when an external magnetic field is applied. In a similar way, by minimizing the free energy respect to the order parameter, it is possible to find another Ginzburg-Landau equation.

Now, let´s take the functional derivative of Eq. 2.17 (the free energy of the superconductor), with respect to ψ:

$$\frac{\delta}{\delta\psi^*}(F_s - F_{n0}) = \frac{\delta}{\delta\psi^*}\left(\alpha|\psi|^2 + \frac{\beta}{2}|\psi|^4\right) + \frac{\delta}{\delta\psi^*}\left(\frac{\left|\left(-i\hbar\nabla - \left(\frac{e^*\mathbf{A}}{c}\right)\right)\psi\right|^2}{2m^*} + \frac{H^2}{8\pi}\right) \tag{2.36}$$

Then, equating to zero, it is obtained:

$$\alpha\psi + \beta|\psi|^2\psi + \frac{\left|\left(-i\hbar\nabla - \left(\frac{e^*\mathbf{A}}{c}\right)\right)\right|^2\psi}{2m^*} = 0 \tag{2.37}$$

Again, $e^* = 2e$ and $m^* = 2m$. Thus, the *Second Ginzburg-Landau equation* is:

$$\alpha\psi + \beta|\psi|^2\psi + \frac{1}{4m}(-i\hbar\nabla - \frac{2e\boldsymbol{A}}{c})^2\psi = 0 \tag{2.38}$$

In addition, it is possible to write a boundary condition that establishes that there are no currents through the surface of the sample:

$$\hat{\boldsymbol{n}} \cdot \left(-i\hbar\nabla - \frac{2e\boldsymbol{A}}{c}\right)\psi = 0 \tag{2.39}$$

where $\hat{\boldsymbol{n}}$ is a unit vector, normal to the surface of the sample. The set of equations 2.35, 2.38 and 2.39, are known as the *Ginzburg-Landau equations* for superconductivity. From these equations, it is possible to describe fundamental characteristics of type II superconductors like the critical fields, the penetration depth and the coherence length.

2.2.2 **Penetration depth**

The superconductors have two main characteristic lengths that determine their electromagnetic properties: the penetration depth (λ) and the coherence length (ξ). And both can be derived from the Ginzburg-Landau theory.

Let´s take eq. 2.35, which defines the current density inside a superconductor, in the presence of an applied magnetic field:

$$\boldsymbol{J} = \frac{ei\hbar}{2m}(\psi \cdot \nabla\psi^* - \psi^* \cdot \nabla\psi) - \frac{2e^2|\psi|^2\boldsymbol{A}}{mc}$$

Now, consider a weak applied field. Then, the variations of ψ in the space will be small. Hence, the equation above can be rewritten:

$$\mathbf{J} = -\frac{2e^2|\psi|^2\boldsymbol{A}}{mc} \tag{2.40}$$

The last equation is the same obtained by using the London theory (eq. 2.13), with $|\psi|^2 = \eta_s$. Equation (2.40) has been found considering the special case, in which ψ has only small variations in space. Hence, the London theory is a special case of the more general Ginzburg-Landau theory. By following the same procedure used in the London theory, the penetration depth results:

$$\lambda^2 = \left(\frac{mc^2}{4\pi e^2|\psi|^2}\right) \tag{2.41}$$

The penetration depth derived from the Ginzburg-Landau theory, accounts for the spatial variation of the magnetic flux density inside the material.

2.2.3 **Coherence length**

The coherence length (ξ) is a new important parameter of the superconducting state, which appears in the Ginzburg-Landau theory. It accounts for the spatial variation of the order parameter ψ (which is related to the number of Cooper pairs), and hence, for the variation of η_s. Taking eq. (2.38)

$$\alpha\psi + \beta|\psi|^2\psi + \frac{1}{4m}\left(-i\hbar\nabla - \frac{2e\boldsymbol{A}}{c}\right)^2\psi = 0$$

In the absence of an applied magnetic field, **A**=0 and ψ ϵ $\mathbb{R}$. With the purpose to minimize the energy, the above equation is normalized by $f = \frac{\psi}{\psi_\infty}$, where ψ_∞ is the value of the order parameter in complete absence of an applied magnetic field, and deep inside the volume of the sample.

$$\frac{\hbar^2}{2m|\alpha|}\frac{d^2f}{dx^2} + f + f^3 = 0 \tag{2.42}$$

The coherence length is defined by the first term, as:

$$\xi^2(T) = \frac{\hbar^2}{2m|\alpha(T)|} \tag{2.43}$$

Now let´s continue to see the physical meaning of the *Ginzburg-Landau coherence length* ξ. Putting eq. (2.43) in eq. (2.42), one obtains:

$$\xi^2\frac{d^2f}{dx^2} + f + f^3 = 0 \tag{2.44}$$

ξ measures the length over which the order parameter ψ changes from its maximum $\psi=\psi_\infty$, to ψ=0. This observation is clearer when considering the linear approximation of eq. (2.44), with

$f(x) = 1 + g(x),\ \ g(x) \ll 1$. This approximation implies that the order parameter has small variations around its equilibrium value. Then,

$$\xi^2 g^{''}(x) + (1 + g) - (1 + 3g + \cdots) = 0 \tag{2.45}$$

This last result leads to: $$g^{''} = \frac{2g}{\xi^2} \tag{2.46}$$

The form of eq. (2.46) suggest an exponential solution: $$g(x) = e^{-\sqrt{2}x/\xi(T)} \tag{2.47}$$

This last result shows that the order parameter varies in space in the range of ξ.

2.2.4 **The Ginzburg-Landau parameter**

The existence of type II superconductors was discovered in the 1930´s, when Mendelssohn´s group in Oxford, reported and incomplete Meissner effect at superconducting alloys. In a type I superconductor the material shows perfect diamagnetism (M=-H), while in type II superconductors, once H_{c1} is reached, the material remains diamagnetic, but M decreases with H. In this state (H_{c1} < H < H_{c2}) the field inside the sample is no more null.

As it has been pointed before, there exists a difference between both free energy densities of states: the normal and the superconducting ones. In the presence of a magnetic field, it can be written:

$$F_s - F_{n0} = \frac{-1}{8\pi}(H_c^2 - H^2) \tag{2.48}$$

where the first term of the right side of eq. (2.48) is the negative condensation energy of the material, and the second term is the positive magnetic energy density due to the applied magnetic field. This last term should be recalculated for type II superconductors. Let´s suppose a normal/superconductor interface. Then, the free energy density of the magnetic surface ($F^{mag,surface}$) is given by the difference, between the real free energy density, and the ideal case (type I), see Fig. (2-2):

$$F^{mag,surface} = -\int_0^\infty \frac{1}{8\pi} H^2 e^{-u/\lambda} du = \frac{-\lambda}{8\pi} H^2 \tag{2.49}$$

As can be seen, it depends on λ, the penetration of the magnetic field inside the sample. Now, if the quantity of superconducting electrons is reduced near the surface, the same happens with the condensation energy density. Thus, the surface condensation free energy density is given by:

$$F^{conden,surface} = \int_0^\infty \frac{1}{8\pi} H_c^2 e^{-u/\xi} du = \frac{\xi}{8\pi} H_c^2 \tag{2.50}$$

Thus, the total free energy density of a type II superconductor at the surface is:

$$F^{surface} = \frac{-1}{8\pi}(\lambda H^2 - \xi H_c^2) \tag{2.51}$$

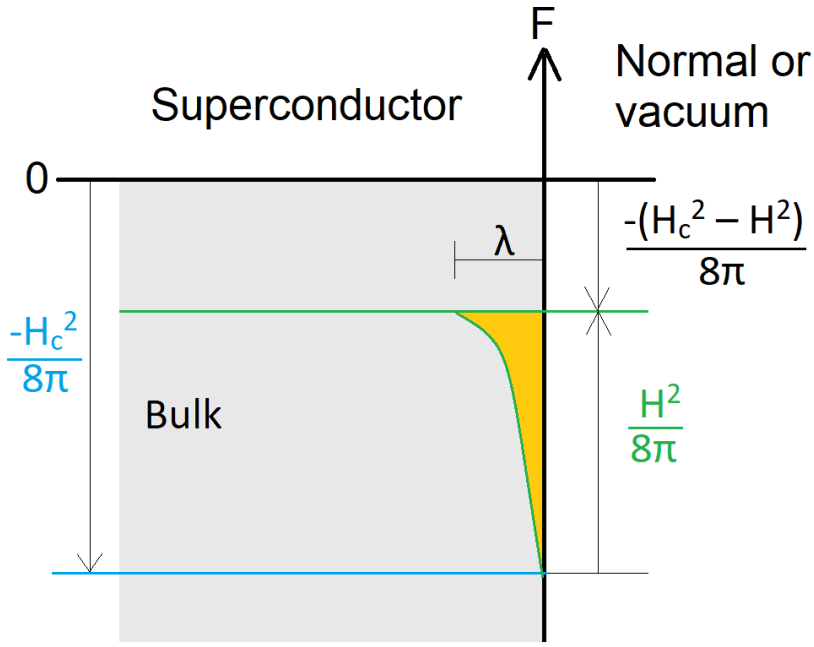

Figure 2-2. Free energy density in a superconductor.

Compared to the normal state, the free energy density in the bulk of the superconductor decreases due to the free condensation energy density (blue), and is raised by the magnetic free energy density (green). The difference between both is $-(H_c^2-H^2)/8\pi$ (eq. 2.48). However, close to the surface in the London region (orange), the free energy density of the magnetic surface is reduced (eq. 2.49). Similar considerations can be applied to the surface condensation free energy density (eq. 2.50). Thus, the total surface free energy density of a type II superconductor is given by eq. 2.51.

Type I superconductors have positive surface free energy, while type II superconductors have a negative surface energy. The sign of $F^{surface}$ depends on the value of the Ginzburg-Landau parameter.

$$\kappa = \frac{\lambda}{\xi} \tag{2.52}$$

This parameter related with the sign of the surface energy, defines the type of a superconductor:

$$\kappa = \begin{cases} < \frac{1}{\sqrt{2}}, & Type\ I \\ > \frac{1}{\sqrt{2}}, & Type\ II \end{cases} \tag{2.53}$$

2.2.5 **Magnetic flux quantization**

At the beginning of the previous section, it has been mentioned that a type II superconductor presents an incomplete Meissner effect when H > H_{c1}. Under this condition, B≠0 close to the surface, but also inside the material. With the aim of learn about this phenomenon, let´s consider a superconducting closed loop C, which is immerse in a weak magnetic field. Now, the order parameter can be written as:

$$\psi = |\psi| e^{i\phi} \tag{2.54}$$

where ϕ is the phase of ψ. Then, eq. 2.35

$$\boldsymbol{J} = \frac{ei\hbar}{2m}(\psi \cdot \nabla\psi^* - \psi^* \cdot \nabla\psi) - \frac{2e^2|\psi|^2\boldsymbol{A}}{mc}$$

can be rewritten as

$$\boldsymbol{J} = -\frac{e\hbar}{mc}|\psi|^2\nabla\phi - \frac{2e^2|\psi|^2\boldsymbol{A}}{mc} \tag{2.55}$$

$\boldsymbol{J}$ is null in C, then: $$\boldsymbol{A} = \frac{-\hbar}{2e}\nabla\phi \tag{2.56}$$

Integrating this last equation and using the Stokes theorem:

$$\oint_C \boldsymbol{A} \cdot dl = \iint_C \nabla X \boldsymbol{A}\, ds = \iint_C \boldsymbol{B}\, ds = \Phi \tag{2.57}$$

On the other hand, using eq. 2.56 in the above integral:

$$\oint_C \boldsymbol{A} \cdot dl = \frac{\hbar}{2e}\oint_C \nabla\phi = \frac{\hbar c}{2e}\Delta\phi = \Phi \tag{2.58}$$

$\Delta\phi$ corresponds to the phase variation of ψ after one circulation around C. To keep ψ as a single-valued function, we make $\Delta\phi$=2nπ, with n integer number. Then:

$$\Phi = \frac{2n\pi\hbar c}{2e} = n\Phi_0 \tag{2.59}$$

Hence, the magnetic flux is quantized. The quantum of magnetic flux is called fluxoid or fluxon:

$$\Phi_0 = \frac{\pi\hbar c}{e} = 2.0678 \cdot 10^{-7}\ gauss \cdot cm^2 \tag{2.60}$$

Flux quantization provides a way to demonstrate the existence of the Cooper pairs. Goodmann and Deaver [4] measured the flux trapped in a hollow cylinder; their results confirm the quantization of magnetic flux and demonstrate that the charge carrier in a superconductor is a pair of electrons.

Then, on type II superconductors the magnetic flux B penetrates in some regions of the material, while other regions remain superconducting. This is the so-called *Mixed State* or *Vortex State.* The last name refers to the fact that the magnetic flux penetrates the superconductor in

the form of flux tubes, called magnetic vortices. Although it will not be demonstrated, it is important to mention that, due to energetic considerations, in the vast majority of cases, each magnetic vortex in a superconductor holds one single fluxon.

2.2.6 **The vortex lattice**

As pointed before, for H > H_{c1}, the magnetic field applied to a type II superconductor penetrates inside the material in the form of magnetic vortices. For a low applied field (close to H_{c1}), there is a low density of vortices. On the other hand, if the applied field is intense (close to H_{c2}), the density of magnetic vortices inside the material will be high, and the vortices will be arrange in a lattice.

First, let´s deduce an expression for the upper critical field H_{c2}. Consider eq. 2.38 with the approximation $\frac{\psi}{\psi_\infty} < 1$, by keeping only the linear terms. Then, take $\boldsymbol{A}$= Hx $\hat{\boldsymbol{j}}$:

$$\alpha\psi + \frac{i\hbar}{4m}(-i\hbar\nabla - \frac{2eHx\hat{j}}{c})^2\psi = 0 \tag{2.38}$$

Later, introduce the frequency: $$\omega = \frac{2eH}{mc} \tag{2.61}$$

Then, after some manipulation: $$-\alpha\psi = (-\frac{\hbar}{4\mathrm{m}}^2\nabla^2 - \mathrm{i}\hbar\omega x\frac{\partial}{\partial y} + \mathrm{m}\omega^2\mathrm{x}^2)^2\psi \tag{2.62}$$

The last equation has the form of the Schrödinger equation for a harmonic oscillator potential. This problem has the solution:

$$\psi = e^{ik_y y}f(x) \tag{2.63}$$

With this solution, eq. 2.62 can be rewritten:

$$-\alpha f = e^{-ik_y y}\left(-\frac{\hbar^2}{4m}\nabla^2 - \mathrm{i}\hbar\omega x\frac{\partial}{\partial y} + \mathrm{m}\omega^2\mathrm{x}^2\right)e^{-ik_y y}f(x)$$

After some manipulation and making the variable change $\mathrm{x}_0 = \frac{-\hbar k_y}{2\mathrm{m}\omega}$

$$-\alpha f = -\frac{\hbar^2}{4m}\frac{\partial^2 f}{\partial x^2} + \mathrm{m}\omega^2(\mathrm{x}+\mathrm{x}_0)^2\mathrm{f} \tag{2.64}$$

which corresponds to a 1-D harmonic oscillator. This problem leads to the Landau levels separated by the cyclotron energy $\hbar\omega$. The resulting harmonic oscillator eigenvalues are:

$$-\alpha = \hbar\omega\left(n+\tfrac{1}{2}\right) \underbrace{=}_{n=0} \frac{\hbar\omega}{2} \underbrace{=}_{eq.\ 2.61} \frac{\hbar\mathrm{eH}}{2mc} \tag{2.65}$$

in which the smallest n corresponds to the applied field H that must be applied to break the Cooper pairs in the superconductor. Thus, taking H ≈ H_{c2}

$$H_{c2} = -\frac{2mc\alpha}{\hbar e} \underbrace{=}_{eq.\ 2.43} \frac{\hbar c}{2e\xi^2} \tag{2.66}$$

Finally $$H_{c2} = \frac{\Phi_0}{2\pi\xi^2} \tag{2.67}$$

This last equation is the well-known expression for the upper critical field of a type II superconductor. Although it is valid for some materials, in the case of iron-based superconductors, estimations made with eq. 2.67 have proven to be inaccurate. Thus, a more complex analysis is necessary, and this topic will be dealt with again in the chapter 6.

Now that we have deduced an expression for H_{c2}, let´s go back to the vortex lattice. Considering the case in which: H is very close to H_{c2}, then the nucleation of the magnetic vortex inside the bulk can be studied with help of a linearized Ginzburg-Landau equation

$$\left(\frac{\nabla}{i} - \frac{2\pi \boldsymbol{A}}{\Phi_0}\right)^2 \psi = -\frac{2m\alpha}{\hbar^2}\psi = \frac{\psi}{\xi^2(T)} \tag{2.68}.$$

Then, taking a convenient vector potential $$A_y = Hx \tag{2.69}$$

Eq. 2.68 is rewritten as $$\left[-\nabla^2 + \frac{4\pi i}{\Phi_0} Hx \frac{\partial}{\partial y} + \left(\frac{2\pi H}{\Phi_0}\right)^2 x^2\right]\psi = \frac{\psi}{\xi^2} \tag{2.70}$$

the effective potential depends only on x, then the solution is of the type:

$$\psi = e^{ik_y y} e^{ik_z z} f(x) \tag{2.71}.$$

However, real superconductors are finite. Thus, the effect of surfaces must be considered. To understand the arrangement of these vortices across the material, consider a narrow thin film with thickness *d* << ξ, immersed in an applied field H > H_{c2}. In the case of one single border, the optimum value of k_y imply that the minimum of the effective potential is ξ away from the surface. In the case of a narrow film of a few hundred nanometersness thick, the effective potential will be determined by the superposition of the potentials related with each border surface (see Fig. 2-3). Thus, if d < $d_c \sim 2\xi$, the minimum of the effective potential is located in the mid-plane of the film. For a thick film (d >> d_c), a superposition solution of the type

$$\begin{aligned} \psi &= e^{ik_y y} f(x) + e^{-ik_y y} f(-x) \\ &= cos\big(k_y y[f(x) + f(-x)]\big) + i\ sen\ \big(k_y y[f(x) + f(-x)]\big) \end{aligned} \tag{2.72}$$

is expected.

Equation 2.72 indicates currents circulating around nodes (meaning vortices) along the mid-plane, at every point for which $cos\ (k_y y)$ =0, at intervals $\Delta y = \frac{\Phi_0}{H(d-d_c)}$. Thus, the solution has periodicity in the *y* direction. For a thick film (bulk sample), there are an infinite number of solutions of the form

$$\psi_k = e^{iky} f(x) = e^{iky} e^{\frac{-(x-x_k)^2}{2\xi^2}} \tag{2.73}$$

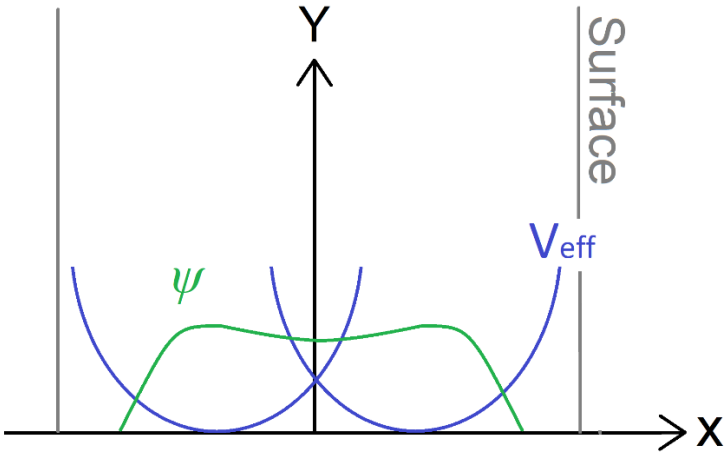

Figure 2-3 Narrow thin film.
Order parameter function (green) and superposition of the effective potential (blue) in a narrow thin film.

As soon as H < H_{c2}, the minimum of the free energy solutions is such that the sample is filled by nodes (each node has one vortex). Moreover, it is expected that a periodic lattice of nodes has lower free energy than a random array. In conclusion, if every ψ_k solution has same weight, there will be periodicity in the x direction. Thus,

$$H\Delta x\Delta y = \Phi_0 \tag{2.74}$$

and each unit cell of the periodic lattice has one fluxon.

2.3 Bibliography

The information of this chapter is treated in the book:

Michael Tinkham. Introduction to superconductivity. McGraw-Hill, Inc. Second Edition. 1996.

[1] F. London and H. London. The electromagnetic equations of the supraconductor. Proc. Roy. Soc. (London), A 149, 71 (1935). Physica A 2, 341 (1935). https://doi.org/10.1098/rspa.1935.0048.

[2] C.J. Gorter, and H.G.B. Casimir. Zur thermodynamik des supraleitenden zustandes. Phys. Z. Vol 35, 963, 1934.

[3] V. Ginzburg and L. Landau. On the Theory of superconductivity (In Russian). Zh. Eksp. Teor. Fiz. 20, 1064-1082. (1950).

[4] W. Goodmann, B.S. Deaver. Detailed Measurements of the Quantized Flux States of Hollow Superconducting Cylinders. Phys. Rev. Lett. 24, 870. (1970). https://doi.org/10.1103/PhysRevLett.24.870.

3 Magnetic properties of type II superconductors

3.1 Magnetic states of type II superconductors

As explained before, in the case of type II superconductors immersed in a magnetic field, the magnetic flux penetrates the material in the form of flux tubes, called magnetic vortices. Therefore, the superconducting state is greatly modified by the presence of these vortices, which effects can be observed in the *magnetization curves*: Magnetization vs. Temperature (M-T) and Magnetization vs. Magnetic Field (M-H), the latter also called *hysteresis loops*. For the reason exposed above, the present work is focused on the study of the magnetization curves, which provide a large amount of information about the behavior of the main parameters of superconductivity. In relation to $SmFeAsO_{1-x}F_x$, it is a High Temperature Superconductor (HTS) with a pronounced type II behavior. Thus, the study of the magnetization curves will provide a description of the superconductor under a magnetic field. Depending on the magnitude of H, a type II superconductor can be in one of three states:

1) **Meissner state.** Type II present the Meissner effect, when the applied magnetic field is $0 < H < H_{c1}$. In this state, the applied magnetic field penetrates only a small distance inside the material (penetration depth λ), over a thin superficial shell of some nanometers in thickness. The magnetic flux in the bulk of the material is null (**B**=0, perfect diamagnetism) and the behavior of the material is described by eq. 1.1-1.4.

2) **Mixed state** (also known as vortex state). When the magnetic field applied to a type II superconductor exceeds the lower critical field (H_{c1}), the superconductor transits from the Meissner state to a mixed state: The Meissner state is lost, and the bulk of the material is penetrated by fine vortices of quantized magnetic flux, surrounded by regions of superconducting material. Thus, the bulk of the material is a normal/superconducting mixed region. The mixed state holds for $H_{c1} < H < H_{c2}$. In contrast, type I superconductors lose superconductivity completely when its unique critical field H_c is reached.

The magnetization measurement of from a type II superconductor in the vortex state, is formed by the sum of two terms: The *Reversible* or *Equilibrium magnetization*, and the *Irreversible magnetization*. The equilibrium magnetization (M_{eq}) is related with surface-like currents and is controlled by the repulsive vortex-vortex interaction. On the other side, the irreversible magnetization (M_{irr}) is related with the volume currents associated with the vortex pinning. Both will be explained in depth shortly.

3) **Normal state.** As the applied field increases over H_{c1}, type II superconductors experiment a gradual decay of the magnetic response. Close to the upper critical field (H_{c2}), the

vortex lattice turns into a more populated, rigid and periodic structure called the *Abrikosov´s vortex lattice*, due to the more intense vortex-vortex interaction. At this point, the material is fully invaded by magnetic vortices. However, complete suppression of superconductivity does not occur until an upper critical field (H_{c2}) is reached. H_{c2} can be very high (tens of teslas), and in the case of $SmFeAsO_{1-x}F_x$ it is expected to be around 100 T or even higher. Then, the complete sample returns to the normal state. If the magnetic field is canceled, the material recovers the superconductivity. In contrast, type I superconductors transit directly from the Meissner to the normal state, once H_c is reached.

3.2 Equilibrium magnetization

The equilibrium magnetization (M_{eq}) comes from the shielding currents on the surface of a superconductor, and provides information about the fundamental parameters of superconductivity: H_{c1}, H_{c2}, λ, and ξ. In 1957, Abrikosov proposed that in the mixed state magnetic vortices appear subject to a repulsive vortex-vortex interaction; M_{eq} describes the vortex dynamics in the absence of vortex pinning [1], which implies an almost defect-free material.

The Lorentz force ($\mathbf{F}_L$) over one single vortex is null at an ideal type II superconductor. Moreover, $\mathbf{F}_L \propto \mathbf{J}_{local}$ and thus to Curl(**B**) through Maxwell equations. Then, **B** has the same value at any point in the specimen, except in a region to the surface determined by the London penetration depth $\lambda_L(T)$. In addition, B only depends on the applied field H and not on the way the field has been increased from zero to its final value. This implies an equivalence between the so called *Field cooled* (FC) and *Zero field cooled* (ZFC) vortex state [2]. In some way, this means a reversible process in the magnetization curves.

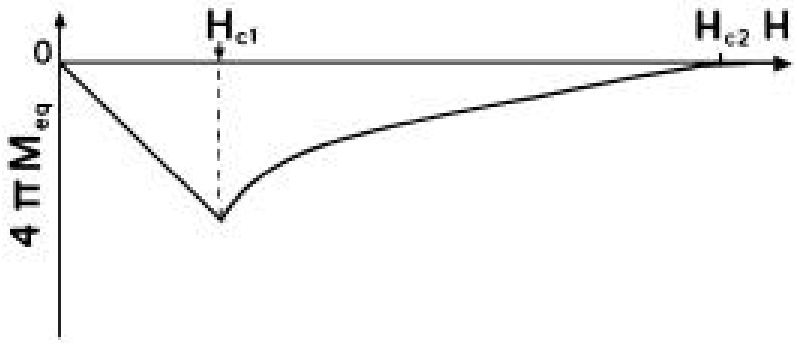

Figure 3-1. Equilibrium magnetization of type II superconductors.
The lower (H_{c1}) and upper (H_{c2}) critical fields are indicated. Notice the negative value of M_{eq}.

Fig. 3-1 presents M_{eq} of type II superconductors. For 0 < H < H_{c1}, M_{eq} follows the linear relation [2]:

$$M_{eq} = -\frac{H}{4\pi} \tag{3.1}$$

In analogy with Meissner region at type I superconductors, M_{eq} has a discontinuity in H_{c1}. This critical field points to the creation of the first magnetic vortex, and the beginning of the Shubnikov or mixed state. This state occurs between H_{c1} and H_{c2}; in this region M_{eq} decays slowly, with a logarithmic tendency described by [2]:

$$4\pi \left[\frac{\partial M_{eq}}{\partial H}\right]_{H_{c2} \gg H \gg H_{c1}} = \frac{-H_{c1}}{2H\ ln(\kappa)} \tag{3.2}$$

with $H_{c1} = \frac{\Phi_0\ \ln(k)}{4\pi\lambda^2}$. And close to H_{c2}:

$$4\pi \left[\frac{\partial M_{eq}}{\partial H}\right]_{H \to H_{c2}} = \frac{-H_{c2}}{(2\kappa^2-1)\beta} \tag{3.3}$$

with $\beta \approx 1$. M_{eq} is due to surface-like currents, and is controlled by the repulsive vortex-vortex interaction. Equations 3.1-3.3 give a general view of the equilibrium magnetization. The following sections will deepen in the vortex dynamics in the absence of vortex pinning (equilibrium magnetization). The study of vortex pinning and irreversible magnetization is left to the end of the chapter.

3.3 Single vortex behavior and lower critical field H_{c1}

When the applied magnetic field exceeds the lower critical field H_{c1}, the superconductor transits from Meissner state to a mixed state. This critical field points to the creation of the first magnetic vortex, and the beginning of the mixed state (see Fig. 3-1). Thus, the bulk material is penetrated by fine vortices of quantized magnetic flux, leading to a normal/superconducting mixed region. As the applied field increases over H_{c1}, type II superconductors experiment a gradual decay of the magnetic response.

In the regime of low H, close to H_{c1}, the separation between vortices is larger than λ. Hence, the vortex-vortex interaction is negligible and the single vortex approximation describes well the behavior of the magnetization of type II superconductors.

The first vortex penetrates when $G_s^{no\ vortex} = G_s^{1st\ vortex}$. Moreover, $G = F - \frac{H}{4\pi}\int B\ dr$, thus $G_s = F_s$ in the absence of magnetic field, leading to

$$F_s = F_s + \epsilon_1 L - \frac{H_{c1}}{4\pi}\int B\ dr \tag{3.4}$$

where the term $\epsilon_1 L$ is the vortex energy per unit length and L is the thickness parallel to the applied field. Considering that the vortex carries one single fluxon

$$F_s = F_s + \epsilon_1 L - \frac{H_{c1}\Phi_0 L}{4\pi} \tag{3.5}$$

leading to:

$$H_{c1} = \frac{4\pi\epsilon_1}{\Phi_0} \tag{3.6}$$

Thus, the lower critical field depends linearly on the vortex energy per unit length ϵ_1. The calculation of ψ or ϵ_1 requires the solution of the nonlinear Ginzburg-Landau equations:

$$\boldsymbol{J} = \frac{ei\hbar}{2m}(\psi \cdot \nabla\psi^* - \psi^* \cdot \nabla\psi) - \frac{2e^2|\psi|^2\boldsymbol{A}}{mc} \tag{2.35}$$

and

$$\alpha\psi + \beta|\psi|^2\psi + \frac{1}{4m}(-i\hbar\nabla - \frac{2e\boldsymbol{A}}{c})^2\psi = 0 \tag{2.38}.$$

Unfortunately, this system requires numerical solutions. Here is enough to say that ψ can be approximated by the function (see appendix C)

$$\psi \approx \tanh\frac{\nu r}{\xi} \tag{3.7}$$

with $\nu \sim 1$. As a result, ψ → 0 as r→ 0, while ψ→ ψ∞, for r > ξ. This behavior can be seen in Fig. 3-2. It can be seen that ξ corresponds nearly to the radius of the magnetic vortex. For r=λ, the order parameter ψ has reached the saturation value ψ∞. Thus, the spatial variations of the order parameter are very pronounced in type II superconductors.

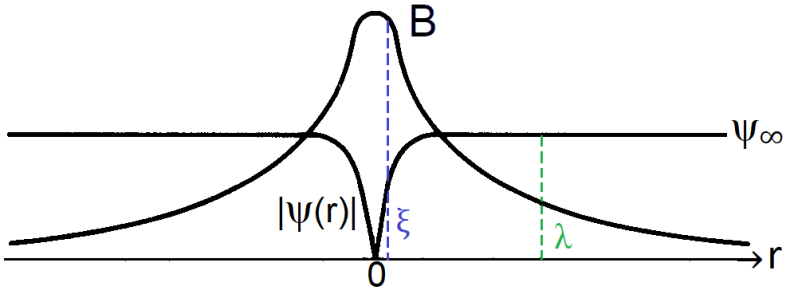

Figure 3-2. Isolated vortex.
Spatial variations of ψ and the magnetic flux density B.

However, a useful analytical result can be obtained if we consider the London limit: λ >> ξ or equivalently $\kappa = \lambda/\xi >> 1$. This condition is fulfilled by some high temperature superconductors like $SmFeAsO_{1-x}F_x$. In this case, when ψ → ψ∞ very rapidly, hence, the material behaves as a London superconductor. Except in a very small region with radius=ξ, around the vortex core. Then, we can approximate $\psi = constant = 1$. Thus, outside the core is possible to apply the London equation:

$$\frac{4\pi\lambda^2}{c}\nabla X\boldsymbol{J}+\boldsymbol{B}=\hat{\boldsymbol{z}}\,\Phi_0\delta(\boldsymbol{r}) \tag{3.8}$$

where the equation has been matched to a delta function centered at the vortex core, to account for the vortex core. $\hat{\boldsymbol{z}}$ is the unit vector in the direction of the vortex´s longitudinal axis. Combining eq. (3.7) with Maxwell eq. $\nabla X\boldsymbol{J}=\frac{4\pi}{c}\boldsymbol{J}$, one obtains: $\lambda^2\big(\nabla X(\nabla X\boldsymbol{B})\big)+\boldsymbol{B}=\hat{\boldsymbol{z}}\Phi_0\delta(\boldsymbol{r})$. Thus, following the procedure used for the London theory:

$$\nabla^2\boldsymbol{B}-\frac{\boldsymbol{B}}{\lambda^2}=-\frac{\Phi_0}{\lambda^2}\Phi_0\delta(\boldsymbol{r}) \tag{3.9}$$

This is a well-known result of the London theory, but with the addition of a delta function in the right side of the equation. The analytic solution to eq. (3.9) is:

$$\boldsymbol{B}(r)=\frac{\Phi_0}{2\pi\lambda^2}K_0\left(\frac{r}{\lambda}\right) \tag{3.10}$$

where K_0 is a Hankel function of order zero. This solution decays as $e^{\frac{-r}{\lambda}}$ for r >> ξ and diverges as $ln\left(\frac{\lambda}{r}\right)$ if r⟶ 0:

$$B(r)=\begin{cases}\frac{\Phi_0}{2\pi\lambda^2}\left(\frac{\pi\lambda}{2r}\right)^{1/2}e^{-r/\lambda}, & r\to\infty\\ \frac{\Phi_0}{2\pi\lambda^2}\left[ln\left(\frac{\lambda}{r}\right)+0.12\right], & r\to 0\end{cases} \tag{3.11}$$

3.4 Energy per unit length of an isolated vortex and lower critical field

In the previous section, an expression was found for the lower critical field H_{c1} (eq. 3.6) in terms of the energy per unit length, ϵ_1. Nevertheless, the value of ϵ_1 was not given due to the difficult of solving the non-linear Ginzburg-Landau equations. However, in the special case where κ >> 1, it is easier to determine ϵ_1 value of an isolated vortex. In turn, this result will provide an expression for H_{c1} in terms of the Ginzburg-Landau parameter κ, meaning the penetration depth λ and the coherence length ξ.

Let´s consider an isolated vortex in a bulk superconductor. If the core of the vortex is ignored, the important terms of G-L free energy (see eq. 2.17) are the magnetic field energy (first term in the right of eq. 3.12) plus the kinetic energy density. Thus, the energy per unit length of an isolated vortex is

$$\epsilon_1=\frac{1}{8\pi}\int(\boldsymbol{B}^2+\lambda^2|\nabla X\boldsymbol{B}|^2)dS \tag{3.12}$$

where the second term in at right member is the kinetic energy of the current density. In this London limit, ψ⟶ ψ∞, Eq. (3.12) can be expanded as:

$$\epsilon_1=\frac{1}{8\pi}\int|\boldsymbol{B}|\Phi_0\delta(\boldsymbol{r})dS+\frac{\lambda^2}{8\pi}\oint\boldsymbol{B}X(\nabla X\boldsymbol{B})\,dl \tag{3.13}$$

The first integral is zero because the origin r=0 is omitted. The integral over the outer perimeter (for r=R⟶ 0) is null. But the integral over the inner perimeter (around the core vortex) gives:

$$\epsilon_1 = \frac{\lambda^2}{8\pi}\left[\boldsymbol{B}\frac{dh}{dr}2\pi r\right]_{\xi} \approx \left(\frac{\Phi_0}{4\pi\lambda}\right)^2 \ln(\kappa) \tag{3.14}$$

where $\frac{dh}{dr} = \frac{\Phi_0}{2\pi\lambda^2 r}$ was used. This result can be substituted in eq. (3.6) to obtain the lower critical field:

$$H_{c1} = \frac{\Phi_0}{4\pi\lambda^2} ln\left(\frac{\lambda}{\xi}\right) \tag{3.15}$$

this is the well-known expression for the upper critical field of type II superconductors. This last equation, with the addition of a constant in the logarithmic term to account for the vortex core, is very important in the analysis of the experimental results of this work.

3.5 Vortex-vortex interaction

For H $\rightarrow H_{c2}$, the distance between vortices gets shorter, and interaction between vortices occurs (Fig. 3-3). The vortex-vortex interaction determines the region H_{c1} < H < H_{c2} in Fig. 3-1. Also, eqs. (3.2) and (3.3) are derived for the vortex dynamics in the absence of pinning. Let´s continue with the case κ >> 1. In this case, the medium is linear and it is possible to use superposition of fields. Then, the magnetic field due to two identical vortex lines is:

$$\boldsymbol{h}(\boldsymbol{r}) = [h(|\boldsymbol{r} - \boldsymbol{r}_1|) + h(|\boldsymbol{r} - \boldsymbol{r}_2|)]\hat{k} \tag{3.16}$$

With $\boldsymbol{r}_1$ and $\boldsymbol{r}_2$, the positions of the vortex cores. Using eq. 3.12, the total increase of free energy per unit length can be calculated:

$$\Delta F = \frac{\Phi_0\, h(\boldsymbol{r}_1)}{4\pi} + \frac{\Phi_0\, h(\boldsymbol{r}_2)}{4\pi} \tag{3.17}$$

The first term is the sum of two identical individual line energies. The second term is the increase in the free energy, due the interaction of both vortex lines. Thus, the force exerted on the second vortex line by the first one (in the direction $\hat{\imath}$) is calculated by taking the derivative of the second term of eq. (3.17):

$$f_{2x} = -\frac{\Phi_0}{4\pi}\frac{\partial h(\boldsymbol{r}_2)}{\partial x_2} \tag{3.18}$$

By rewriting the eq. (3.18) in a vector form and using the Maxwell eq. $\nabla X\boldsymbol{h} = \frac{4\pi \boldsymbol{J}}{c}$, one obtains: $f_2 = \boldsymbol{J}_1(\boldsymbol{r}_2)\hat{\boldsymbol{j}}\, X\, \frac{\Phi_0\, \hat{\boldsymbol{k}}}{c}$. The flux has the same direction in both vortices, and thus, the force between them is repulsive. This result can be generalized to the force exerted by all vortices over one given vortex line:

$$f = \boldsymbol{J}\, X \frac{\Phi_0}{c} \tag{3.19}$$

$\boldsymbol{J}$ is the total supercurrent density due to all other vortices (and any transport current if there is one) at the position of a given vortex.

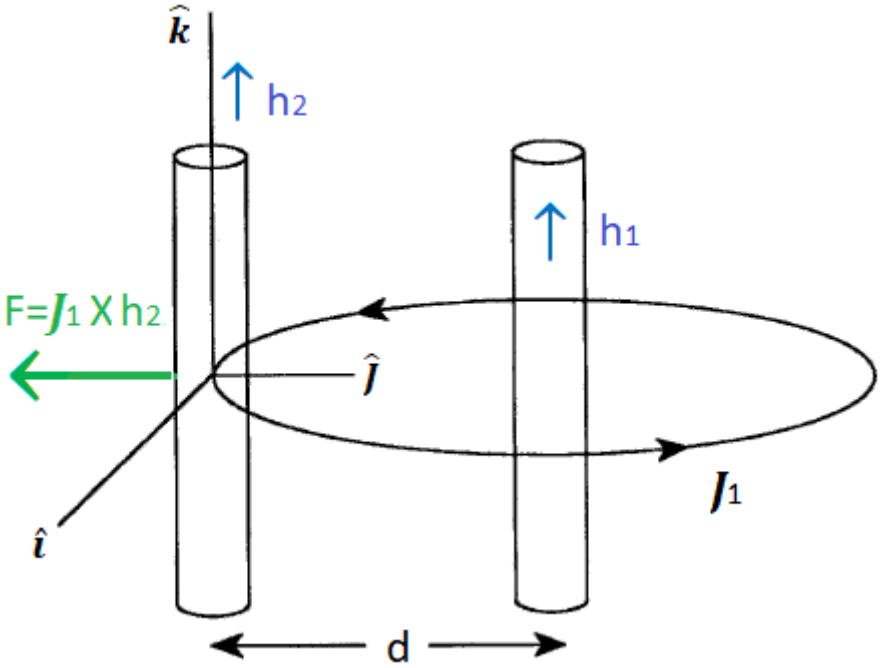

Figure 3-3. Vortex-vortex repulsive interaction.
The force exerted by vortex line 1 on vortex line 2 is caused by the magnetic field h_2 (of vortex 2), and the current density $\boldsymbol{J}_1$ (of vortex 1). If the vortex lines are too far separated, $\boldsymbol{J}_1$ from vortex 1 will not interact with h_2, and the interaction between vortices is considered null.

In addition to the vortex-vortex interaction, vortices can be fixed to the imperfections of the crystal lattice (pinning) and have oscillations around their longitudinal axis. These three phenomena are the basis of the flux creep theory, a model for understanding the vortex dynamics inside a type II superconductor. Section 3.7 explores the subject of pinning in more detail, while flux creep theory was used to interpret the experimental results of critical fields and the critical current density.

3.6 Vortex interaction near the upper critical field

If the applied magnetic field is high, close to the upper critical field H_{c2}, the vortices are closely packed. Then, for an applied field close to H_{c2} the cores do not touch but occupy most of the sample volume. Thus, it can be assumed that the magnetic flux across the sample is nearly uniform. However, in this limit the London approximation is not correct, and the solution requires the Ginzburg-Landau equations. Nevertheless, it is possible to simplify the problem, by

considering that $\frac{\psi}{\psi_\infty} < 1$ for H $\rightarrow H_{c2}$. This condition means that the density of Cooper pairs diminish considerably. Thus, it is possible to neglect the higher order term in:

$$\alpha\psi + \cancel{\beta|\psi|^2\psi} + \frac{i\hbar}{4m}(-i\hbar\nabla - \frac{2e\boldsymbol{A}}{c})^2\psi = 0 \tag{2.38}$$

The result is a linearized Ginzburg-Landau equation. Hence, it is possible to use the well-known general solution proposed by Abrikosov (for an applied field close to H_{c2}):

$$\psi = \sum_n c_n e^{inqy} e^{-\frac{(x-x_n)^2}{2\xi^2}} \tag{3.20}$$

Abrikosov proved that in this regime the magnetization M is proportional to $|\psi|^2$:

$$B = H + 4\pi M = H\ - \frac{H_{c2}-H}{(2\kappa^2-1)\beta_A} \Rightarrow M = -\frac{H_{c2}-H}{4\pi\,(2\kappa^2-1)\beta_A} \tag{3.21}$$

where $\beta_A = \frac{\langle\psi^4\rangle}{\langle\psi^2\rangle^2} \geq 1$. Notice that the factor $(2\kappa^2 - 1) = 0$, for $\kappa = \frac{1}{\sqrt{2}}$, is the criterion to separate type I and II superconductors, as has been previously mentioned in section 2.2.4.

Equation (3.21) indicates a linear decrement of diamagnetism as H grows, reaching a normal state at H_{c2}=H. Moreover, the decay of diamagnetism is slower for smaller values of β_A. From an energetic point of view, this implies that a smaller β_A coefficient corresponds to a lower free energy, and hence, to a more stable lattice. For a triangular lattice of vortices, β_A=1.16, and for a squared lattice, β_A=1.18. Thus, the vortices in the mixed state at high applied magnetic fields will order into a triangular lattice[5].

3.7 Irreversible magnetization and Bean model of a critical state

In a more realistic approximation, the imperfections in the material pin the vortex lines. Thus, a single vortex is subjected to a pinning force by the structural defects of the material. And there is also a magnetic vortex-vortex pressure. As this pressure is lower than the pinning force, the vortices stay fixed in space. Otherwise, vortices are depinned. The pinned vortices induce electrical currents flowing through the volume of the material. In turn, these pinning currents induce a new non-equilibrium magnetization term M_{irr}, so that the measured signal is M= M_{eq} + M_{irr}. The commonly reported critical current density (J_c), is due to these volume currents.

The fact that magnetic vortices are pinned over the volume of the sample implies that the magnetization will depend on the previously applied magnetic fields, meaning that M_{irr} leads to the appearance of magnetic hysteresis on magnetization plots. In materials like iron-based

[5] Initially, Abrikosov proposed the square lattice. Later, Kleiner et al. demonstrated that the triangular lattice is a system with the less free energy [3]. However, nowadays the triangular lattice is known as Abrikosov´s lattice.

superconductors, the M_{irr} signal can be intense, screening M_{eq}. In that case, the magnetic signal measured will display hysteresis loop, like the one of Fig. 3-4.

A hysteresis loop can be divided in regions. For example, the *virgin magnetization* or *first magnetization* [4] is defined as the region for which the sample has not been previously exposed to a magnetic field, under the condition that H < H^*. The *full penetration field* H^* [2] is the applied field required for a magnetic vortex to reach the center of the sample. The virgin magnetization gives information about the Meissner state, H_{c1} and H^*.

For H > H^*, and if the applied field is strong enough, the magnetic hysteresis disappears and the loop closes in a single curve. This point is called the irreversibility field (H_{irr}). For H < H_{irr}, the magnetic vortices are fixed in their positions inside the material. If H > H_{irr}, the vortices will not be pinned anymore; they will move freely, in a similar way to the condition of equilibrium magnetization. H_{irr} is a key point that influences the behavior of multiple parameters of the mixed state including the upper critical field H_{c2}, and the intra- and intergranular critical current densities, J_{intra} and J_c. The critical fields H_{c1} and H_{c2} are illustrated in Fig. 3-1, the virgin magnetization and H^* can be seen on Fig. 3-4. H_{irr} is shown in Fig. Fig 6-13 of chapter 6.

To determine the influence of the applied magnetic field and the temperature on the vortex dynamics is difficult. For this reason, phenomenological models have been developed, the simplest of which is the Bean model. In this model, J_c is considered constant. This simple model gives a rough approximation to the vortex dynamics, the magnetic flux and the current density in the material [5].

As mentioned before, M_{eq} can be screened by the M_{irr}. Hence, the former will be omitted. With the hypothesis that J_c=constant, M_{irr} can be defined as

$$M_{irr} = \frac{M^+ - M^-}{2} \tag{3.22}$$

where $M^+$and M^- are the upper and lower branches of the hysteresis loop. Thus, M_{irr} is defined by the vertical height of the loop. The model also allows calculating the critical current of the superconductor. With this purpose, let´s remember that the *magnetization is the sum of the magnetic dipoles per unit volume induced by the current loops in the sample*:

$$M_{irr} = \frac{1}{V}\int_{r^*}^{R} SdI \tag{3.23}$$

where the volume (cylindrical sample) is $V = \pi L R^2$, with R the radius of the sample, $dI = J_c L\, dr$, and $S = \pi r^2$. This leads to

$$M_{irr} = \frac{1}{\pi L R^2}\int_{r^*}^{R} \pi r^2 J_c L\, dr = \frac{J_c R}{3}\left(1 - \frac{r^{*3}}{R^3}\right) \tag{3.24}$$

Considering that $r^*$is the depth inside the sample so that $r^* = R(1-h)$, with $h = \frac{H}{H^*}$, and $H^* = J_c R$, the irreversible magnetization can be written as $M_{irr} = \frac{J_c R}{3}$ (SI) or $M_{irr} = \frac{J_c R}{30}$ in CGS units. Thus, the critical current density J_c is

$$J_c = \frac{30\, M_{irr}}{R} \tag{3.25}$$

A detailed explanation about the different critical currents of $SmFeAsO_{1-x}F_x$ can be found in the chapter of experimental results. At the moment, it is necessary to say that the last equation gives the magnitude of the highest current density that flows across the superconductor, I mean the intergranular critical current density. This value is an important parameter for technological applications. The hysteresis cycle predicted by the Bean model is illustrated in the Figure 3-4. The characteristic of this loop is that the maximum (or the minimum) of the magnetization is a horizontal line (M+ or M-).

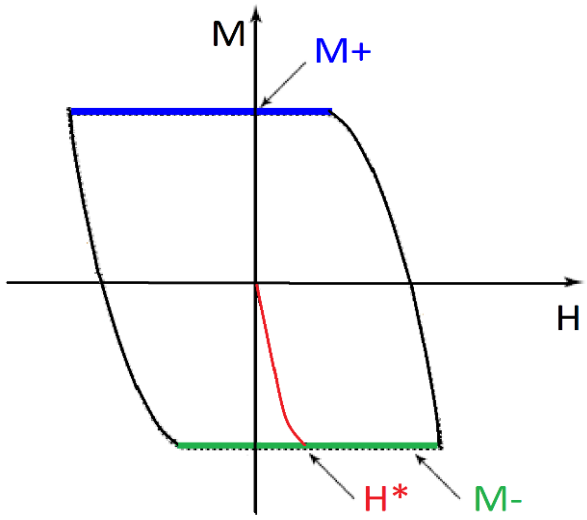

Figure 3-4. Hysteresis cycle predicted by the Bean model.
The virgin magnetization, also called first magnetization (orange) is limited by the full penetration field (H^*). The vertical branches are often called reversal magnetization. The horizontal branches are known as the upper (M+, in blue), and the lower branch (M-, in green).

3.7.1 **Bean exponential model**

The Bean model simplifies the complexity of vortex dynamics and allows determining J_c in an easy manner. Nevertheless, it does not fit well with observed behavior in HTS, including the iron-based superconductors. To avoid this issue, more complex models have been proposed, in which the critical current is not a constant anymore. Each of these models defines the dependence of J_c with regards to the applied magnetic field. From all the modified Bean models, the exponential decay of J_c(H), known as the exponential model, is the one that fits the best the experimental behavior of $SmFeAsO_{1-x}F_x$ [4,6]. With the purpose of calculating the magnetization, J_c of eq. (3.24) cannot be considered a constant anymore [6], leading to

$$M = \frac{-1}{10R^2}\int_0^R J(H(r))r^2 dr \tag{3.26}$$

with

$$J_c(r) = J_0 e^{\frac{-|H(r)|}{H_0}} \tag{3.27}$$

where J_0 and H_0 are constants that depend on the temperature and the material, and R is the radius of the sample. From eqs. (3.26) and (3.27), it is possible to find an expression for the critical current density in analogy with eq. (3.25), but this time the deduced expression is more complex

$$J(r) = \frac{J_0 e^{-h}}{\left(1-(R-r)/r_0 e^{-h}\right)} \tag{3.28}$$

where $h(r)$ is

$$h(r) = \frac{H}{H_0} + ln\left(1 - \frac{R-r}{r_0} e^{-\frac{H}{H_0}}\right) \tag{3.29}$$

and

$$r_0 = \frac{10 H_0}{4\pi J_0} \tag{3.30}.$$

As can be seen from eq. (3.28) and (3.29), the size of the sample affects the critical current density. This model also provides an expression for the full penetration field H^*, and its dependence on the size of the sample

$$H^* = H_0 \ln(1 + \frac{r}{r_0}) \tag{3.31}.$$

Figure 3-5 illustrates a real hysteresis loop for a $SmFeAsO_{1-x}F_x$ sample. The contrast with Fig. 3-4 is evident: there are no flat regions due to the field dependence of J_c.

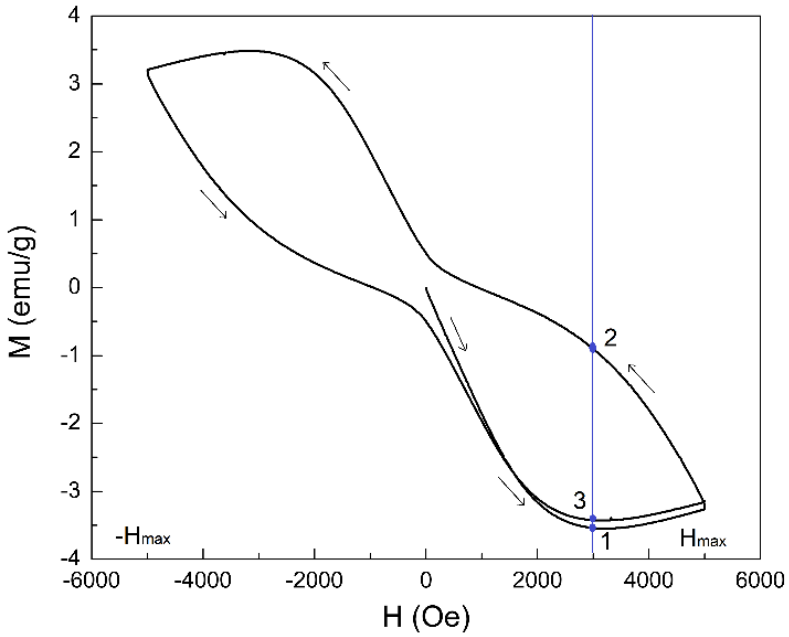

Figure 3-5. Hysteresis cycle of $SmFeAsO_{0.91}F_{0.09}$.
Sample with particle size r_g=1680 nm. The arrows indicate if H is increasing or decreasing. H is the same at points 1 and 2; however, the magnetization is quite different, so this graph illustrates a wide hysteresis cycle.

3.7.2 Magnetic hysteresis cycle

To explain the magnetic hysteresis, suppose a material is initially in a null applied magnetic field H=0. Later, H → H_{max} (the highest applied field), and back, H → -H_{max}. Finally, the field goes to zero. This is a complete hysteresis cycle. Type II superconductors present magnetic hysteresis; this means that M depends on a previously applied magnetic field. Fig. 3-5 illustrates a complete hysteresis cycle with five quadrants, measured from a sample of $SmFeAsO_{0.91}F_{0.09}$, with r_g=1680 nm. The arrows indicate if the applied magnetic field is growing or decreasing.

The blue line at H=3000 Oe intersects the loop three times: number 1 points to the magnetization M_1 when the sample is exposed for the first time to a field of H=3000 Oe (virgin magnetization). In 2, the sample has already reached $H_{max} < H_{c2}$ and is immersed in a decreasing magnetic field, the magnetization at this point (M_2) is being close to zero, so $M_2 \neq M_1$. The figure illustrates a wide hysteresis loop. In 3, the sample has experienced the complete hysteresis cycle and is immersed in an increasing magnetic field, just as in number 1, but this time the previous exposure to H affects the magnetization of the sample (due to vortex pinning), so then $M_3 \neq M_1$.

3.8 Blibliography

The topics of this chapter are treated in the book:

Michael Tinkham. Introduction to superconductivity. McGraw-Hill, Inc. Second Edition. 1996.

[1] A.A. Abrikosov. On the Magnetic Properties of Superconductors of the Second Group. JETP, Vol. 5, No. 6, p. 1174 (1957).

[2] S. Senoussi, F. Pesty. Magnetization of organic superconductors: influence of defects. Studies of High Temperature Superconductors: Diverse Superconducting Systems and Some Miscellaneous Applications, vol. 37, Nova Science Publishers, Huntington, NY, USA, 2001.

[3] W.H. Kleiner, L.M. Roth, S.H. Autler. Bulk Solution of Ginzburg-Landau Equations for Type II Superconductors: Upper Critical Field Region. Phys. Rev. 133, A1226 (1964). https://doi.org/10.1103/PhysRev.133.A1226.

[4] P. Chaddah, G. Ravi Kumar, A.K. Grover, C. Radhakrishnamurty, G.V. Subba Rao. Critical state model and the magnetic behavior of high T_c superconductors. Cryogenics, Volume 29, Issue 9, September 1989, 907-914. https://doi.org/10.1016/0011-2275(89)90204-X.

[5] C.P. BEAN (1962). Magnetization of Hard Superconductors. Phys. Rev. Lett. 8, 250. https://doi.org/10.1103/PhysRevLett.8.250.

[6] S. Senoussi, C. Aguillon and P. Manuel. The origin of the low field peak in the hysteresis cycle of high-Tc oxides and the influence of magnetic pinnings. Physica C 175 (1991) 202-214. https://doi.org/10.1016/0921-4534(91)90254-V.

4 Introduction to particle size effects on the superconducting properties

Nanoscale structured materials have exhibited new and exceptional properties, which are unexpected in a macroscopic scale. Many of these outstanding properties can be attributed to finite size effects, quantum size effects, and surface effects. In superconductivity, the finite size effects are manifested in some physical properties, which include: critical temperature, superconducting gap, lower and upper critical fields, Meissner state as well as the critical state [1,2]. The size dependence of these properties will be observed at different length scales which go from the mesoscopic to the nanometric scale.

The effects of reducing the particle size in type I superconducting materials have been studied since the second half of the XX century. These phenomena include changes in the fundamental parameters, like the penetration depth and the coherence length, but also, other parameters like the critical current density and the critical fields of the superconductor are affected by the size of the superconductor.

However, for type II superconductors, there is scarce information available, and most of the size effects were studied in thin films and single crystals. The lack of information is probably due, to the difficulty in controlling the growth of the particles in materials like cuprates or iron-based superconductors. These families of HTS are granular materials with a layered crystalline structure.

This chapter gives a short introduction to the already known effects related to particle size, and establishes a comparison for the experimental results obtained in the present work.

4.1 Granularity and size effects

The critical fields and critical currents are determined by the penetration depth (λ) and the coherence length (ξ), which can be in the range of a few nanometers up to hundreds of nanometers (depending on the superconducting material), and the finite size effects on those physical properties might be observed in particles with mesoscopic dimensions. As a matter of fact, the influence of the effective size of the sample on the magnetic properties has been well established in various theoretical and experimental works for various superconducting materials [3-7]. In some of these works *granularity* has been pointed out as one of the most important characteristics that influences the superconducting properties of the HTS.

The meaning of *granularity* can be explained as follows: It is supposed that a sintered pellet is formed by multiple superconducting grains, joined by intergranular links. Thus, the pellet can be seen as a chain of *Josephson junctions* (links). These junctions are composed by two superconducting grains, separated by a non-superconducting barrier. In this case, the barrier is the proper boundary between two coupled grains [8]. When the Josephson junctions break, either by increasing the temperature, by a high enough applied magnetic field or by the effect of milling, the sample can be seen as a group of individual grains.

The parameters referring to a property of the sample considered as one single interconnected entity are called *inter*. For example, the *intergranular critical current density* (J_c) corresponds to the maximum current that can flow across the grains, over the whole sample. On the opposite site, the parameters of the sample considered as a group of decoupled grains, are called *intra*. For example, the *intragranular critical current density* (J_{intra}) corresponds to the currents inside each single grain in the sample [9,10]. Thus, *the concept of granularity is closely related with the effective size of the superconductor*.

The nature of the links between grains is very important on how granularity affects the superconducting properties of the material. For example, while in the intermetallic Low Temperature Superconductors (LTS) junctions between grains would have a Superconductor-Normal Metal-Superconductor character, in HTS they would have a Superconductor-Insulator-Superconductor one. The latter makes easy to break the intergrain coupling, and, as a result, a polycrystalline sample of a HTS has low values of critical current densities [11,12]. This is known as the *weak-link problem*, and is the main difficulty faced to use cuprates and iron-based superconductors in technological applications.

4.2 Transition critical temperature

Quantum size effects are observed as the suppression of superconductivity and have been related to destabilization of the superconducting gap or the Cooper pairs themselves [3], a phenomenon predicted by Anderson in 1960 [13]. Nevertheless, there is evidence that under some circumstances Cooper pairs are not destabilized but strengthened, because the surface effect can give place to a better electron-phonon coupling [14].

In type I superconductors with reduced particle size, the variation of the transition critical temperature (T_c) is governed mainly by a competition between Surface Effects (SE) and Quantum Size Effects (QSE). As the particle size gets smaller, the surface/volume ratio increases and the surface effects cause a phonon softening [14-16]. At the same time, a small particle size leads to a discretization of the energy levels, reducing the effective density of states at the Fermi level and also T_c [3].

On the other hand, HTS like iron-based compounds and cuprates, have a granular nature, so that the intergranular coupling and strain effects, have also an important role in the behavior of T_c. In the conventional MgB_2 (C-doped) type II superconductor, it was found that T_c decreases with r_g [17]. The present work is not focused on the size dependence of T_c, but it is important to mention that a significant shift in the values of T_c was not found for r_g in the range between 220-1680 nm.

4.3 Penetration depth and coherence length

Intrinsic superconducting properties are modified by the size of the particles that form the sample: the magnetic penetration depth λ, and the superconducting coherence length ξ. Therefore, it makes sense to expect changes in other superconducting properties when the sample dimensions reach the order of magnitude of λ or ξ.

The penetration depth measures how deep inside the sample the applied magnetic field can penetrate, so this length is very important for the behavior of the critical fields of a superconductor. On the other side, ξ is related to the value of the superconducting order parameter (ψ) and determines if there are non-local effects. Many early studies were focused on how these parameters are affected by the mean free path (*l*) of the superconducting electrons in the material.

In type I superconductors, where ξ is of the order of hundreds of nm, changes in the mean free path of the superconducting electrons can be achieved by the introduction of atomic impurities. This is known as the dirty limit (Pippard), and accounts for non-local effects. The coherence length is modified, after Pippard, as [18]:

$$\frac{1}{\xi} = \frac{1}{\xi_0} + \frac{1}{l} \tag{4.1}.$$

where the intrinsic coherence length (ξ_0) is defined by the superconducting energy gap at zero temperature, and can be defined as the "size" of a Cooper pair. The values of ξ and ξ_0 coincide at T=0. An alternative way to change *l* is to reduce the particle size r_g. This implies that ξ is reduced as r_g becomes smaller. It has been shown that the type I superconductor changes to a type II behavior, in the case of small particles [3].

On the other case, type II superconducting materials usually have very small values of ξ (a few nanometers), and then, it is highly probable that these materials are in what is known as the clean limit ($l > \xi$). There is a relation between λ_{eff} and ξ; λ_{eff} increases when the particle size is reduced, leading to a decrease in ξ. This can be seen in eq. (4.2) [4]:

$$\lambda_{eff} = \lambda_0 \left(\frac{\xi_0}{\xi}\right)^{1/2} \tag{4.2}.$$

This equation is used in the present work, to have an estimation of ξ_{eff} as a function of the particle size r_g. In both types of superconductors, the effective coherence length for a given particle size defines the penetration depth [4,18] and affects other important features.

4.4 Magnetization and critical fields

The reduction of the size of the superconducting particles also has effects on the macroscopic properties like the magnetization; for example, it is well known that the demagnetizing field is affected by the grain size r_g. In the case of superconductors with r_g smaller than λ, the Meissner effect is vanished or is very limited, due to the increase in the penetration depth. This means that the penetration of the magnetic field inside the sample is easier, so that it floods the interior of the sample for lower magnitudes of the applied field.

The critical field H_{c1} decreases with particle size; lower r_g values lead to a smaller surface area, so the intensity of the surface shielding currents would decrease, making easier the vortex entrance [19]. This explanation is in agreement with the well-known calculation of the size dependence of the diamagnetic susceptibility, within the framework of the Ginzburg-Landau theory [20]

$$\chi = -\left(\frac{1}{4\pi}\right)\frac{r_g^2}{10\lambda(T)^2} \tag{4.3}$$

Equation (4.3) holds for small r_g. Thus, the term r_g^2 decreases rapidly while λ increases, leading to a fast decrease of χ.

The full penetration field H^* (see chapter 3) is also affected by the shrinkage of the sample. In the specific case of the cuprates, some theoretical works have shown that when the volumetric current decreases exponentially with the applied field, then, H^* depends on r_g following a logarithmic law [21]

$$H^* = H_0 \ln\left(1 + \frac{r_g}{r_0}\right) \tag{4.4}$$

4.5 The irreversibility field

In the case of elementary superconductors, like Nb nanoparticles, the irreversibility field H_{irr} decreases with r_g (H_{irr} was defined in chapter 3). However, this dependence has irregularities for some small values of size, in which H_{irr} actually increases [22]. The study of H_{irr} in HTS began in 1987, when Müller and his colleagues identify the irreversibility line of $La_{2-x}Ba_xCuO_4$ [23]. The effect of size on H_{irr} has been also reported; The irreversibility line of $Bi_2Sr_2Ca_2Cu_3O_x$/Ag was studied in tapes of small dimensions, and it was found that it changes following a power law dependence $H_{irr} \sim r_g^{0.13}$; on the other hand, the properties of H_{irr} in bulk material and single

crystals was compared with no significant differences [24]. These examples clarify that the behavior of H_{irr} depends on each specific material.

This observation also indicates that the critical current density must depend on the particle size of the material. In MgB_2 (C-doped), which is the conventional superconductor with the highest T_c (39K), and is also a type II superconductor, it was found that H_{irr} increases as r_g decreases, but this tendency is reversed if the particle size continues diminishing [17]. However, there is no much more information available in this regard, and the specific properties of the iron-based superconductor studied in this work ($SmFeAsO_{1-x}F_x$) are different from those of the materials mentioned above. For this reason, the dependence of $H_{irr}(r_g)$ is studied in this thesis.

When considering the simplest case (see Bean model, chapter 3), the irreversible magnetization does not show a dependence on r_g. Nevertheless, the magnetic signal measured in VSM experiments of HTS shows a decrease with reduced particle size [25]. In an effort to explain this, some theoretical models suggest that the magnetization (M) depends on the particle size in materials where J_c depends on H (see Bean exponential model in chapter 3). In the case of HTS, like cuprates and iron-based superconductors, an exponential decay of J_c with the applied magnetic field H has been proposed. From these ideas result that M depens on H and r_g

$$M_{irr}^{+}(H \geq 0) = \frac{J_c(H)\, r_g}{30}\left[1 - \frac{r_g}{4r_0}e^{-h} + \frac{r_g^2}{10r_0^2}e^{-2h}\right] \quad \text{and}$$

$$M_{irr}^{-}(H \geq H^{*}) = \frac{J_c(H)\, r_g}{30}\left[1 + \frac{r_g}{4r_0}e^{-h} + \frac{r_g^2}{10r_0^2}e^{-2h}\right] \quad (4.5)$$

where M_{irr}^{+} and M_{irr}^{-} are the decreasing and increasing field branches of the hysteresis loop. The constant r_0 is defined as:

$$r_0 = \frac{10H_0}{4\pi J_0} \quad (4.6)$$

with H_0 and J_0 are constants that depend on the temperature [21]. This model fits particularly well with experimental magnetization curves when r_g is reduced down to the order of magnitude of λ.

The study of the relation between the upper critical field H_{c2} and r_g, is important in order to allow the technological uses of HTS. It is known that the upper critical field is inversely related to the coherence length (see chapter 2), as can be seen from the equation

$$H_{c2} = \frac{\Phi_0}{2\pi\xi^2} \quad (4.7).$$

This result is true for many materials, like the elementary superconductors. Furthermore, as it has been mentioned before, the reduction of size entails a decrease of ξ. Then, it would be reasonable to conclude that the effect of reducing the particle size, is an increase of H_{c2}. However, the experimental observations refute this statement. On the contrary, H_{c2} of type II superconductors tends to decrease as r_g gets smaller. This has been observed in materials with important technological applications, like Nb_3Sn [26, 27] and MgB_2 [16].

Nonetheless, this behavior has not been corroborated in structurally more complex materials, like layered cuprates or iron-based superconductors. In the particular case of $SmFeAsO_{1-x}F_x$, H_{c2} reaches a value too high for a direct M-H measurement; it has been estimated that H_{c2} must be in the range of 80-100 T for bulk material. Nothing has been said about H_{c2}as a function of $H_{c2}(r_g)$, this justifies important relation is studied in the present work.

4.6 Critical current density

The critical current density J_c is the maximum current density that can flow across the sample without dissipation. It is determined fundamentally by the vortex-vortex interaction and by the flux pinning, defined as the interaction between the microstructure of the material with the magnetic vortex in the superconductor. In LTS, a smaller particle size provides a higher concentration of structural features that act as vortex pinning centers, resulting in an enhanced J_c [3,27]. Grain boundaries are the most common feature that favors a higher J_c, but also dislocations, micro-cracks, and other defects can behave as pinning centers.

These observations have been verified in LTS like NbTi, which was one of the first materials used to build superconducting magnets. In materials belonging to the A15 group, including V_3Si, Nb_3Sn, Nb_3Ge, Cs_3C_{60}, and others, it is well known that the pinning force, and, in consequence, J_c are strongly influenced by r_g. In the particular case of Nb_3Sn, the total pinning force depends on particle size as $F_{pinning} \sim (r_g)^{-1}$ [27].

The discovery of HTS created the hope of superconducting cables with T_c above the boiling point of nitrogen. Nevertheless, the influence of grain boundaries on J_c of granular materials, like cuprates and iron-based superconductors, is contrary to the description given above; comparisons between J_c measurements performed on single crystals and polycrystalline samples, demonstrate that the latter values are many orders of magnitude smaller than those obtained for single crystals. This observation suggests that grain boundaries cause a large decrease of J_c in polycrystalline samples.

Hence, in polycrystalline HTS, the grain boundaries act as superconducting barriers between grains, negatively affecting superconductivity. So, the polycrystalline sample forms a chain of superconducting grains coupled by Josephson junctions, the so-called "weak link problem" [28-30]. Grain boundaries with pronounced misorientation angles, cannot form a continuous current path all across the sample, and do not contribute to the intergranular critical current density J_c.

As a result of the weak link problem, the strategy to enhance J_c in HTS is focused in trying to vanish the effect of Josephson junctions, by means of the manufacture of nearly single crystalline materials, in which the misorientations at the boundaries must be as small as possible [29,31].

4.7 Bibliography

[1] B. Mühlschlegel. Superconductivity of small particles. Phys. B 203 (3) (1994) 444–447. https://doi.org/10.1016/0921-4526(94)90094-9.

[2] H. Zeller, I. Giaever. Superconductivity in very small particles. Physica 55 (1971) 173–185. https://doi.org/10.1016/0031-8914(71)90250-3.

[3] S. Bose, P. Ayyub, A review of finite size effects in quasi-zero dimensional superconductors. Rep. Prog. Phys. 77 (11) (2014). https://doi.org/10.1088/0034-4885/ 77/11/116503 116503.

[4] M. Tinkham, Penetration depth, susceptibility, and nuclear magnetic resonance infinitely divided superconductors. Phys. Rev. 110 (1958) 26–29. https://doi.org/10. 1103/PhysRev.110.26.

[5] S. Senoussi, F. Pesty. Magnetization of organic superconductors: influence of defects. Studies of High Temperature Superconductors: Diverse Superconducting Systems and Some Miscellaneous Applications, vol. 37, Nova Science Publishers, Huntington, NY, USA, 2001.

[6] R.W. Cohen, B. Abeles. Superconductivity in granular aluminum films. Phys. Rev. 168 (1968) 444–450. https://doi.org/10.1103/PhysRev.168.444.

[7] V. Blanco-Gutiérrez, M.J. Torralvo-Fernández, M. Alario-Franco. Particle size effect on the superconducting properties of $YBa_2Cu_3O_{7-x}$ particles. Dalton Trans. 46 (2017) 11698–11703, https://doi.org/10.1039/C7DT01974B.

[8] Chaddah et al. Critical state model and the magnetic behavior of High-T_c superconductors. Cryogenics 29 (9) (1989) 907 – 914. doi:https://doi.org/10.1016/0011-2275(89)90204-X.

[9] A. Yamamoto, A.A. Polyanskii et al. Evidence for two distinct scales of current flow in polycrystalline Sm and Nd iron oxypnictides. Supercond. Sci. Technol. 21 (2008) 095008 (11pp). Doi:10.1088/0953-2048/21/9/095008.

[10]. E.S. Otabe, M. Kiuchi, S. Kawai, Y. Morita, J. Ge, B. Ni, Z. Gao, L. Wang, Y. Qi, X. Zhang, Y. Ma. Global and local critical current density in superconducting $SmFeAsO_{1-x}F_x$ measured by two methods. Physica C: Superconductivity, Volume 469, Issue 21, 1 November 2009, Pages 1940-1944. https://doi.org/10.1016/j.physc.2009.06.013.

[11] J. Cheng, H. Li, S. Liu, J. Huang, Y. Chen, P. Hsu, Z. Wu, C. Wang, M. Lan. Size effect on superconductivity and magnetism of $MoSr_2YCu_2O_{8-\delta}$. J. Phys. 97 (1) (2008). https://doi.org/10.1088/1742-6596/97/1/012270.

[12] D.A. Balaev, S.V. Semenov, M.I. Petrov, Correlation between magnetoresistance and magnetization hysteresis in a granular high-Tc superconductor: Impact of flux compression in the intergrain medium. J. Supercond. Novel Magn. 27 (6) (2014) 1425–1429. https://doi.org/10.1007/s10948-014-2491-6.

[13] P. Anderson. Theory of dirty superconductors. J. Phys. Chem. Solids 11 (1) (1959) 26–30. https://doi.org/10.1016/0022-3697(59)90036-8.

[14] P. Townsend, S. Gregory, R.G. Taylor. Superconducting behavior of thin films and small particles of aluminum. Phys. Rev. B 5 (1972) 54–66. https://doi.org/10.1103/PhysRevB.5.54.

[15] W.L. McMillan. Transition Temperature of Strong-Coupled Superconductors. Phys. Rev. 167, 331. 1968. https://doi.org/10.1103/PhysRev.167.331.

[16] J.M. Dickey, Arthur Paskin. Size and Surface Effects on the Phonon Properties of Small Particles. Phys. Rev. B 1, 851. 1970. https://doi.org/10.1103/PhysRevB.1.851.

[17] B. J. Senkowickz el al. Nanoscale grains, high irreversibility field, and large critical current density as a function of high energy ball milling time in C-doped magnesium diboride. doi:10.1088/0953-2048/21/3/035009. https://doi.org/10.1088/0953-2048/21/3/035009.

[18] E.A. Lynton. Superconductivity. Chapter 4.4. London: Methuen and Co. Ltd. Second edition. 1964.

[19] N. Morozov, E.Zeldova, M. Konczykowskib, R.A. Doyle. Geometrical and distributed surface barriers in $Bi_2Sr_2CaCu_2O_8$. Physica C: Superconductivity, Volume 291, Issues 1–2, 15 November 1997, Pages 113-131. https://doi.org/10.1016/S0921-4534(97)01666-3.

[20] B. Mühlschlegel, D.J. Scalapino R. Denton. Thermodynamic Properties of Small Superconductors. Phys. Rev. B 6, 1767 (1972). https://doi.org/10.1103/PhysRevB.6.1767.

[21] S. Senoussi, C. Aguillon, P. Manuel. The origin of the low field peak in the hysteresis cycle of high-T_c oxides and the influence of magnetic pinnings. Physica C 175 (1991) 202-214. https://doi.org/10.1016/0921-4534(91)90254-V.

[22] Sangita Bose. Size Effects in Nanostructured Superconductors. Ph.D. thesis. Department of Condensed Matter Physics and Material Science. Tata Institute of Fundamental Research Mumbai. July 2007.

[23] K.A. Müller, M. Takashige, J.G. Bednorz. Flux trapping and superconductive glass state in La_2CuO_{4-y}:Ba. Phys. Rev. Lett. 58, 1143, (1987). https://doi.org/10.1103/PhysRevLett.58.1143.

[24] Qiang Li, M. Suenaga, T. Freltoft. Sample size effect on the determination of the irreversibility line of high-Tc superconductors. Appl. Phys. Lett. 64, 250 (1994). doi: 10.1063/1.111519.

[25] John R. Clem, Vladimir G. Kogan. Theory of the Magnetization of Granular Superconductors: Application to High-T_c Superconductors. Japanese Journal of Applied Physics, Volume 26, Supplement 26-3, Part 2. doi:10.7567/jjaps.26s3.1161.

[26] W. Schauer, W. Schelb. Improvement of Nb_3Sn high field critical current by a two-stage reaction. IEEE Transactions Magnetics, Vol. Mag-17, No. 1, January 1981. DOI: 10.1109/TMAG.1981.1060900.

[27] S. Ochiai, K. Osamura. Influence of grain size and upper critical magnetic field on global pinning force of bronzed-processed Nb_3Sn compound. Acta Metallurgica, Volume 34, Issue 12, December 1986, Pages 2425-2433. https://doi.org/10.1016/0001-6160(86)90145-8.

[28] C. S. Pande, R.A. Masumura. Grain Boundary and size effects in high and low transition temperature superconductors. Materials Science and Engineering B32 (1995) 247-253. https://doi.org/10.1016/0921-5107(95)03015-8.

[29] P. Sunwong, J.S. Higgins, Y. Tsui, M. J. Raine and D.P. Hampshire. The critical current density of grain boundary channels in polycrystalline HTS and LTS superconductors in magnetic fields. Supercond. Sci. Technol. 26 095006 (2013). doi:10.1088/0953-2048/26/9/095006.

[30] D. Dimos, P. Chaudhari, J. Mannhart, F. K. LeGoues. Orientation Dependence of Grain-Boundary Critical Currents in $YBa_2Cu_3O_{7-\delta}$ Bicrystals. Phys. Rev. Lett. Vol. 61, No. 2, 1988. https://doi.org/10.1103/PhysRevLett.61.219.

[31] D.C. Larbalestier et al. Weak links and the poor transport critical currents or the 123 compounds. Physica C: Superconductivity, Volumes 153–155, Part 3, June 1988, Pages 1580-1585. https://doi.org/10.1016/0921-4534(88)90426-1.

5 Experimental methods

5.1 X-Ray diffraction and Bragg´s law

X-Rays were discovered by Wilhelm Röntgen in 1895 [1]. The name comes from their unknown nature at that time. The development of X-Ray diffraction motivated the study of Solid-State Physics and the understanding of chemical bonding. The Coulombic force is used to produce X-Rays; A tungsten filament inside an evacuated tube is heated by a small AC voltage (5-15 V) to produce electrons. A second voltage (5-80 kV) between the filament and a metallic target (anode) accelerate the electrons, which hit the target, losing their kinetic energy almost instantly: Thus X-Ray radiation is emitted in all directions, with variable energies, depending on the number of collisions necessary to stop the electrons. The differences of energy are responsible for the continuous spectrum or Bremsstrahlung.

X-ray diffraction allows the study of the internal structure of matter. Diffraction occurs when waves scattering from an object and cause interference, constructive or destructive, with each other. The geometrical condition for X-Ray diffraction in real space was named Bragg´s law, to honor W.L. Bragg, who showed that crystallographic planes reflect X-Rays as mirrors causing the diffraction patterns. Now, be θ the incident angle of two parallel rays, and λ the wavelength of the incident X-Rays. The interplanar spacing *d* causes a difference of length in the path followed by the ray scattered by the first plane and the ray scattered by the second plane. As can be seen in Figure 5-1.a, the path length difference is $2d\sin(\theta)$. Constructive interference between diffracted X-Rays waves, occurs when the path difference is equal to a multiple of λ, and Bragg´s law is written

$$2d\sin\theta = n\lambda, \quad n \in \mathbb{N} \tag{5.1}$$

In this way, Bragg´s law describes interference caused by the periodicity of the crystal lattice forms a diffraction pattern like the one shown in Figure 5-1.b.

5.2 Scherrer´s equation

An important issue in nanoscience is to determine the size of the structures of interest. An X-Ray beam is formed by many rays with the same incident angle θ_B (Bragg´s angle), and others with angles of incidence slightly different from θ_B. Inside the crystal there will be planes that scatter the incident rays; the interference will be constructive for θ_B and partly destructive for other incident angles. This causes the broadening of the peaks in the diffraction pattern, as the crystallite size decreases. A more detailed explanation can be found in [2].

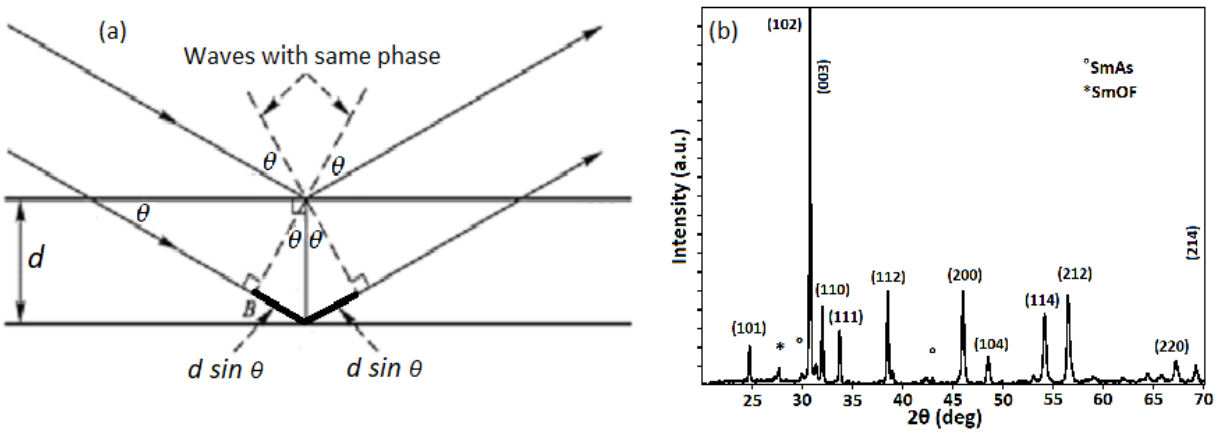

Figure 5-1. Bragg´s law and X-Ray Diffraction pattern of $SmFeAsO_{1-x}F_x$.

a) The successive crystallographic planes reflect X-Rays as mirrors, producing constructive interference in the diffracted rays. The incident and diffracted angle (θ) are the same, while the inter-planar distance is d. b) X-ray diffraction pattern of $SmFeAsO_{0.91}F_{0.09}$, produced with a source Cu-Kα_1= 1.540598 Å.

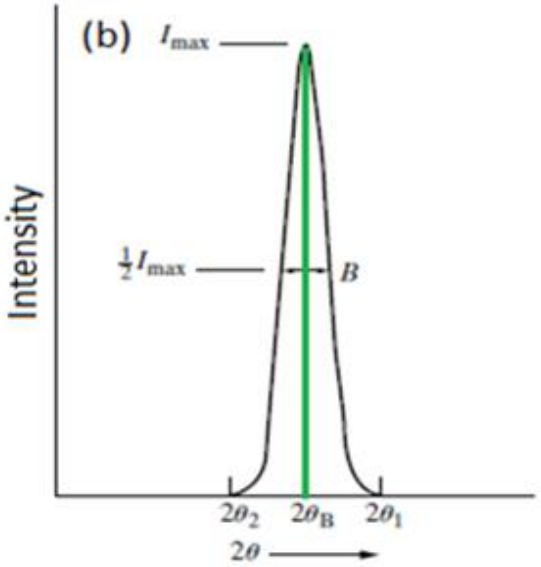

Figure 5-2. Scherrer´s law. Diffraction peak profile.

Ideal case without broadening (green), where all the diffraction processes occur at exactly θ_B, and real case in black (from $2\theta_1$-$2\theta_2$). Illustration was taken from [2].

Figure 5-2 shows the profile of an ideal (green line) and a real (black line) diffraction peak. The interval ($2\theta_1$, $2\theta_2$) increases as the number of crystallographic planes decreases, with a corresponding increase in the width of the peaks in the diffraction pattern for smaller particles. Scherrer´s law is written

$$t = \frac{k\,\lambda}{B\cos\theta_B} \tag{5.2}$$

where B is the Full Width at Half Maximum (FWHM) and k~0.9 is a factor that accounts for the shape of the sample. Hence, Scherrer´s equation relates the average crystallite size *t*, with the broadening (FWHM) of the peaks in the diffraction pattern.

5.3 Scanning electron microscopy (SEM)

A scanning electron microscopy (SEM) has a high vacuum electron column. At the top is an electron gun that produces an electron beam, with the aid of an acceleration voltage. The beam is conducted across the column by a set of electromagnetic lenses, to a chamber where the sample is placed. The lenses also focus the electron beam over the sample (see Figure 5-3.a). Then, the scan coils deflect the electron beam with the purpose to scan the surface of the sample. The energy of the electrons (0- 30 keV) depends on the acceleration voltage, and determines the penetration of the beam ($\sim 10^{-6}$ m) and the excitation volume in the sample. The resolution of the instrument is determined by the diameter of the beam (0.5-1 µm), the beam current (probe current ~ 1 pA-1 µA), which measures the number of electrons that hit the sample in one second, the convergence angle of the beam´s tip 2α (0.001 -0.05 rad), and the work distance W (10^{-4}-10^{-2} m), see fig. 5-3.b. Beam interacts with the atoms of the sample to produce: Secondary electrons, created by inelastic scattering of beam´s electrons with the atoms of the sample. Characteristic X-Rays, created in the same way and gives information about the chemical elements present in the sample. Backscattered electrons (BSE) are beam electrons scattered by the sample, with energy similar to their incident energy. SEM, images are formed mainly by secondary electrons, but it is also possible to interpret the BSE signal to form an image of the surface of the sample. The highest magnification in SEM is around 200,000X and its best resolution is around 1 nm.

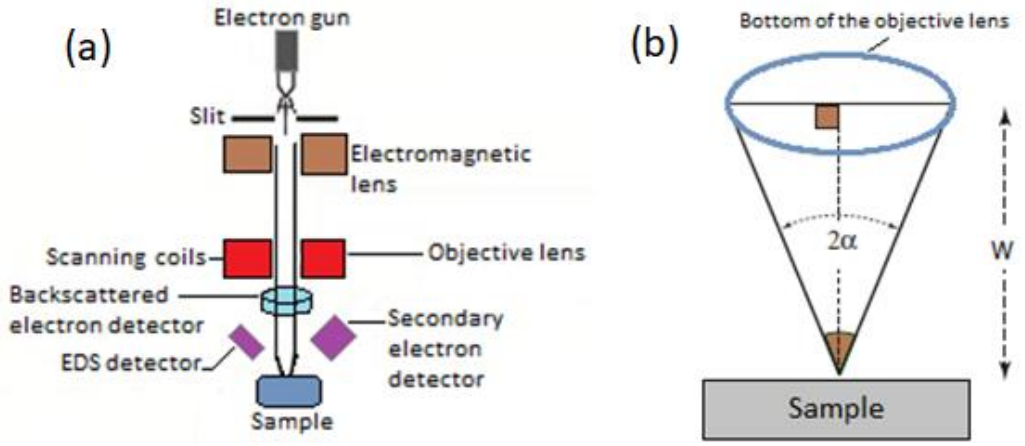

Figure 5-3. Diagram of a Scanning Electron Microscope (SEM).
a) Diagram of a SEM. b) Detail of the electron beam´s tip, the work distance (W), and the convergence angle of the electron beam over the sample.

5.4 Vibrating Sample Magnetometer (VSM)

A vibrating sample magnetometer (VSM) allows the measurement of the magnetic moment of the sample. It was invented independently in 1956, by G.W. Van Oosterhout [3] and S. Foner [4]. It is the basic instrument used to characterize the magnetic properties of superconductors. The physical principle behind the VSM is Faraday´s law. The sample is carefully centered between a pair of pickup coils. These coils are mounted on the poles of an electromagnet (see Figure 5-4.a) that generates a uniform magnetic field H. For superconducting characterization, the described experimental arrangement is set inside a helium cryostat fitted between the magnet poles. The measurement of the magnetic moment is performed by oscillating the magnetized sample between the detection coils. This induces a change in the magnetic flux through the coils, generating a voltage (V_{VSM}) on them. According to Faraday´s law:

$$V_{VSM} = n_c\, n_w \iint \frac{\partial B}{\partial t}\, dA \tag{5.3}$$

where n_c is the number of detecting coils, n_w is the number of loops in each coil, A is the area enclosed by a single loop and *B* is the magnetic induction in the sample. This voltage signal is proportional to the magnetic dipole moment of the sample, and also to the vibration amplitude and frequency of the sample. Usually, the electromagnet is capable to generate very strong magnetic fields, whereby superconducting magnets are used. A VSM is well suited for measurements on magnetically hard or semi-hard materials, allowing the study of hysteresis cycles. The instrument used in this work has a sensitivity <10^{-6} emu. Thus, it allows performing measurements on soft magnetic materials also. The helium cryostat is capable to manage temperatures from 1.8 to 400 K, facilitating the study of superconducting samples.

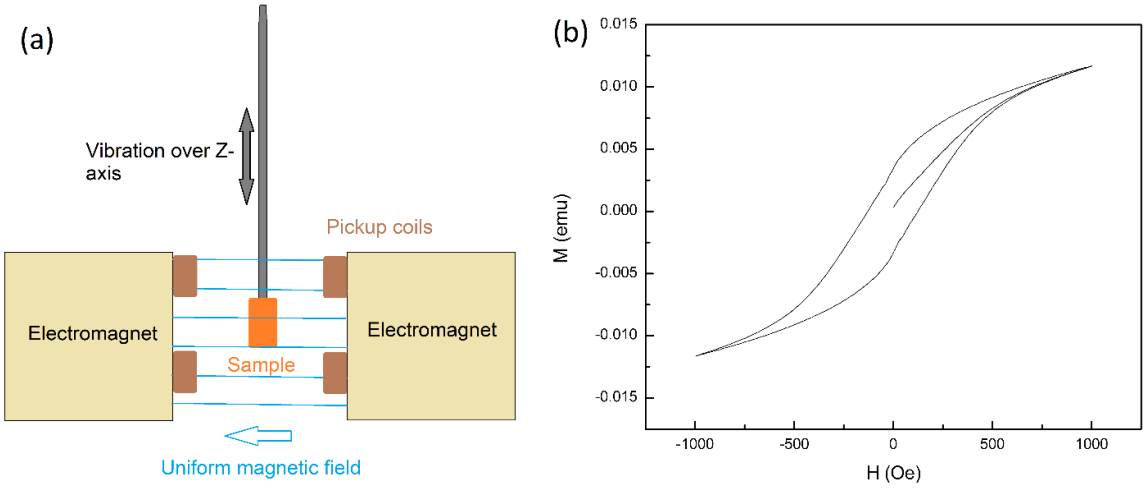

Figure 5-4. VSM diagram and hysteresis cycle.

a) Detail of the experimental mounting of a sample in a VSM. b) Hysteresis loop of a sample of $SmFeAsO_{0.91}F_{0.09}$, measured with a VSM in the Physics Department, CINVESTAV.

The Figure 5-4.b shows a magnetic hysteresis loop, measured from a randomly oriented powder sample of $SmFeAsO_{0.91}F_{0.09}$. The X-axis corresponds to the applied magnetic field (H), while the Y-axis represents the magnetization of the sample (M). It can be appreciated that for $T>T_c$, the magnetization of the sample is ferromagnetic, and in consequence, superconductivity is absent.

5.5 Bibliography

The information about X-Ray diffraction (XRD) is treated in the books:

B.D. Cullity, S.R. Stock. Elements of X-Ray diffraction. Chapter 1, Properties of X-Rays. Third edition. Pearson new international edition. Pearson Education Limited. 2004.

Charles Kittel. Introduction to Solid State Physics. Chapter 2, Wave diffraction and the reciprocal lattice. Eight edition. John Wiley and Sons, Inc. 2005.

The information about Scanning electron microscopy (SEM) is treated in the books:

Joseph I. Goldstein, Dale E. Newbury, Joseph R. Michael, Nicholas W.M. Ritchie, John Henry J. Scott and David C. Joy. Scanning electron microscopy and X-Ray microanalysis. Springer Nature, fourth edition. 2018.

And introduction to TEM, SEM and AEM. Physical Principles of Electron Microscopy. Ray F. Egerton. Springer. 2005.

The information about Vibrating Sample Magnetometer (VSM) is treated in the next sources:

David Jiles. Introduction to Magnetism and Magnetic Materials. Section 3.1.5. Vibrating-Sample magnetometer (VSM). Springer-Science+Business Media. 1991.

Website of Quantum Design: https://www.qdusa.com/products/dynacool.html.

[1] Elsevier Publishing Company. Physics 1901-1921. Nobel lectures, including presentation speeches and laureates' biographies. Amsterdam, 1967.

[2] B.D. Cullity, S.R. Stock. Elements of X-Ray diffraction. Chapter 5, Diffraction III: Real samples. Third edition. Pearson new international edition. Pearson Education Limited. 2004.

[3] Van Oosterhout, G.W., Klomp, C.J. On the effect of grinding upon the magnetic properties of magnetite and zinc ferrite. Appl. sci. Res. 9, 288–296 (1961). https://doi.org/10.1007/BF02921815.

[4] S. Foner. Vibrating Sample Magnetometer. Review of Scientific Instruments 27, 548 (1956). https://doi.org/10.1063/1.1715636.

6 Experimental results and discussion

The iron-based superconductors (IBSC) were discovered in 2008[6] by Hosono et al [1]. At that time it was a surprise, because it was supposed that iron atoms would prevent superconductivity. IBSC are non-conventional superconductors, which means that the coupling mechanism of Copper pairs, is not explained by the BCS theory. For this reason, the study of IBSC is of great scientific interest. Moreover, these type II superconducting materials have attracted attention, due to its high critical temperature up to 58.1 K [3], and high upper critical field (H_{c2}), which has been estimated to be over 80 T [4,5]. However, other characteristics like material anisotropy and a strong pinning potential make this material a candidate for technological applications.

The chemical compound $SmFeAsO_{1-x}F_x$, is part of the IBSC family REFeAsOF (with RE=Rare Earth), also known as 1111-type superconductors, due to the chemical composition of the parent compound SmFeAsOF (without doping). This work is focused on its superconducting properties and how they evolve as the particle size (r_g) is reduced. With this purpose, polycrystalline samples of $SmFeAsO_{1-x}F_x$ were synthesized[7] by a one-step solid-state reaction. Phase identification was carried out by using X-Ray diffraction (XRD), confirming $SmFeAsO_{1-x}O_x$ as the main phase with very small traces of SmAs and SmOF.

Later, the sample was divided in different pieces. These were manually ground for different periods of time, with the purpose to obtain a set of samples of the same material, but with different particle sizes. The particle size of each sample was determined by microstructural observations, realized on a Jeol 7401 microscope (SEM). The dependence of DC electrical resistance on the temperature was measured for the sample with r_g = 1680 nm, by the four-probe method, on a Quantum Design PPMS Dynacool equipment, in the range 3-100 K. In this way, a T_c of around 56.1 K was found.

The characterization of the magnetic properties of the complete set of samples was performed in a vibrating sample magnetometer (Quantum Design PPMS Dynacool). Magnetization vs. Temperature (M-T) curves were obtained for different applied magnetic fields. Also, Magnetization vs. Applied Magnetic Field (M-H) measurements were done for different temperatures. By analyzing these data, it was possible to study as a function of r_g, the changes in the main properties of the superconducting state: lower critical field (H_{c1}), full penetration field (H^*), Meissner state, penetration depth (λ) and coherence length (ξ), irreversibility field (H_{irr}), upper critical field (H_{c2}), decoupling critical current density (J_D), intragranular critical current density (J_{intra}) and intergranular critical current density (J_c).

[6] The same scientific group published about an iron-based superconductor in 2006 [2], but it is generally accepted the year 2008 as the date of discovery for these kind of materials.

[7] The superconducting samples were elaborated in the Physics Department of CINVESTAV Zacatenco.

6.1 Synthesis of $SmFeAsO_{1-x}F_x$

Polycrystalline samples of $SmFeAsO_{0.91}F_{0.09}$ were synthesized by a one-step solid-state reaction [5]. The chemical precursors were: Fe_2O_3, SmF_3, Fe and Sm in the form of powders. The quantities of each species were set to a stoichiometric ratio[8] of 1:1:1:1 for Sm, Fe, As, and O. The used amounts of oxygen and fluorine must add 1 mole. An additional reduction of oxygen was considered because of the ineluctable oxidative process of all the chemical precursors due to the oxygen present in the atmosphere. All these starting materials were mixed by manual grinding, inside a glove box filled with highly pure argon atmosphere (99.999 % purity), by using a pestle and a mortar made of agate, during a hundred minutes. Later, the powder thus produced was compressed under 10 Ton with the help of a hydraulic press, to form pellets. These pellets were covered with an envelope of tantalum and evacuated inside a quartz ampoule. Pellets inside the sealed ampoule were heated to 500 °C for 12 hours and 950 °C for 48 hours. After the synthesis process, the furnace was allowed to cool in a natural way[9]. The pellets obtained can be seen in Fig. 6-1. Afterward, pellets were divided into different pieces, each of them was ground for a specific period of time with the purpose to obtain samples with different particle sizes.

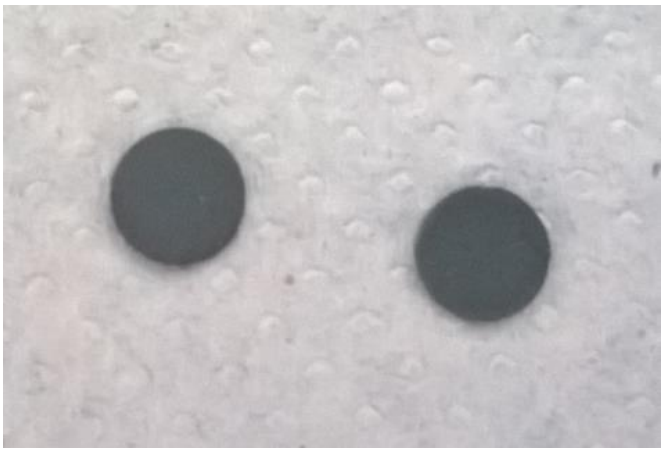

Figure 6-1. Pellets of $SmFeAsO_{0.91}F_{0.09}$.

6.2 Phase identification

Phase identification was carried out by using X-Ray diffraction (XRD) on a Rigaku Smart Lab Diffractometer[10], equipped with a copper tube of K_α radiation λ_{XRD} = 1.5406 Å. The diffraction pattern of a sample synthesized in the Physics Department of CINVESTAV Zacatenco is presented in Fig. 6-2. This sample was elaborated with a nominal composition of fluorine of 0.2; however,

[8] For a detail view of calculations see appendix D.
[9] Some illustrations of the process can be seen in appendix E
[10] Phase identification was carried out in the Physics Department, CINVESTAV Zacatenco.

due to evaporation, the quantity present in the final compound is lower. In spite of the presence of small traces of other phases, SmAs and SmOF, this is a high-quality material to realize this study. The data obtained from the X-Ray diffractometer was analyzed with the Match! v3.4 (Demo version).

The phase identification of the complete set of samples with different particle size was realized in a diffractometer Bruker D8 Advance Eco Diffractometer[11] equipped with a similar copper tube ($K_{\alpha 1}$). The experimental diffraction patterns of the samples with different particle sizes are shown in Fig. 6-3. The diffraction patterns of two similar samples of $SmFeAsO_{1-x}F_x$ with different fluorine contents, show a small shift in the position of the main peaks [6, 7]. As can be seen in figure, no clear shift in the positions of any of the peaks is detected in the diffraction patterns of the samples here studied; this is an indication that the manual grinding done after the sintering process does not produce a change in the fluorine content of the samples. Therefore, any change in the superconducting properties of the material is caused by the decrease of the particle size. Figure 6-3 indicates a broadening of the peaks of the diffraction pattern (this can be clearly seen in the main peaks) as the particle size goes to smaller values, this is due to a decrease in the crystallite size of the sample. However, there is no clear shift in the positions of any of the peaks in the diffraction patterns, this point is discussed in more detail in section 6.4.

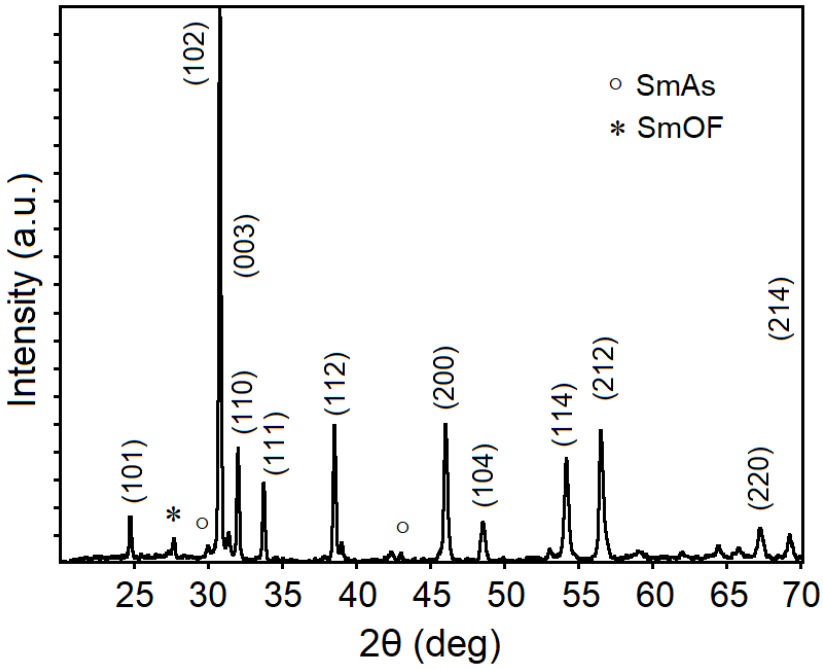

Figure 6-2. Diffraction pattern of $SmFeAsO_{1-x}F_x$.

Diffraction pattern of $SmFeAsO_{1-x}F_x$ obtained from a sample selected to realize the study. The main peak is identified with the Miller indices (102). In the region 25° < 2θ < 30°, there are two small peaks related with small traces of SmAs (°) and SmOF (*).

[11] This study was carried out in the Chemistry Department, CINVESTAV Zacatenco.

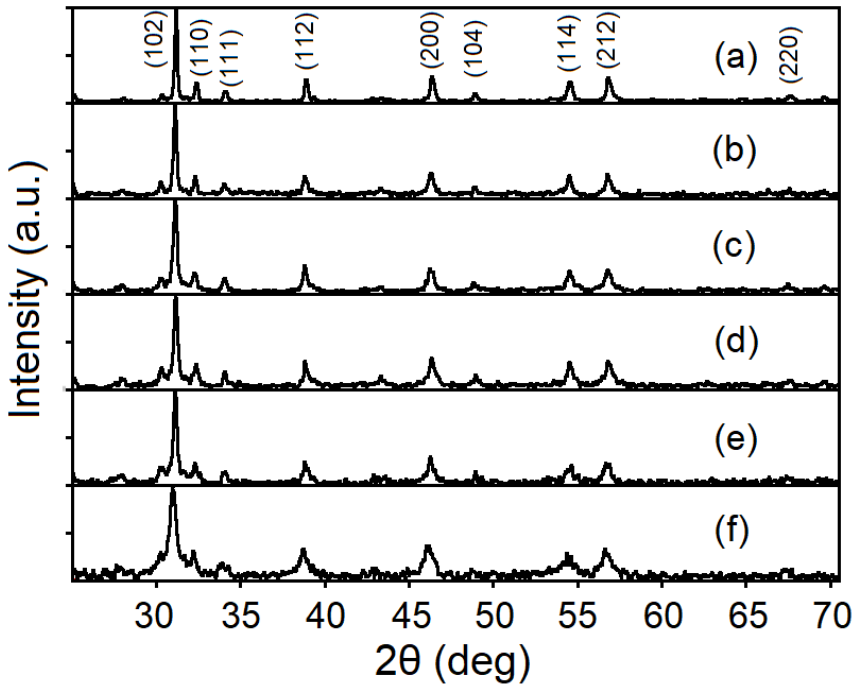

Figure 6-3. Experimental X-Ray diffraction patterns.

Samples with r_g of: a) 1680 nm, b) 550 nm, c) 470 nm, d) 405 nm, e) 345 nm and f) 220 nm. There is no clear shift in the positions of any of the peaks in the diffraction patterns.

In Table 1, the crystallite sizes are reported for all samples. These were calculated with Match! v3.4 (Demo version), and a reference pattern from LaB_6 was used. However, it is important to say that the crystallite size no necessarily correlates with the particle size in our samples, and the present work is focused on changes produced by the particle size.

Particle size (r_g) nm	Standard deviation of r_g (σ nm)	Crystallite size nm
1680	215	116
550	77	100
470	53	58
405	54	52
345	41	49
220	30	--

Table 1. Particle size and Crystallite size of different samples.

The values of r_g and the crystallite size do not match: The particle size defines the effective size of the sample, while the crystallite size is related with the broadening of the peaks ($2\theta \sim 31°$) observed in the diffraction patterns of Fig. 6-2. Most of the times r_g > crystallite size.

The sample with particle size r_g=220 nm was not available at the time of the study. However, the significant broadening of the main peak in Fig. 6-3.f as compared to Fig. 6-3.e indicates that the crystallite size of this sample must be smaller than the 49 nm of the sample with r_g=345 nm. The values of both columns do not math: The particle size defines the effective size of the sample. It can be related with the fundamental parameters of superconductivity, like the penetration depth and the coherence length. On the other side, the crystallite size is related with the broadening of the main peak ($2\theta \sim 31°$) observed in the diffraction patterns of Fig. 6-3.

6.3 Micro-structural analysis and average particle size

With the purpose to determine the average particle size (r_g *diameter*) of each sample after different grinding times, many micrographs of each sample were taken (see Fig. 6-4). The images were gridded in a similar way as Fig. 6-4.e. By gridding the micrographs, it is easier to keep track of which ones have already been measured, and thus avoid measuring the same particle twice. The diameter was measured as the distance between two edges of the particle, as indicated by the small orange lines in Fig. 6-4.e. The particles are considered as spheres. *In the case of elongated particles, the size was taken the length*. There are some theoretical works that support the spherical approximation [8,9]. Micrographs were taken in a microscope model Jeol 7401 (SEM), while the diameter of the particles was measured with the aid of the software ImageJ v1.51. It was found that the distribution of particle size is approximately normal (see Fig. 6-4).

The average particle size r_g of each sample was determined as the *mode* of its particle size distribution (a hundred measurements for each sample); as can be seen in Fig. 6-5, r_g matches the peak´s position of the normal distribution (in blue) superimposed on the particle size distribution, for the sample with r_g= 220 nm. The experimental values of r_g and the related standard deviation (σ) are given in Table 1 (see section 6.2).

On the other side, the micrographs of Fig. 6-4 clearly show that as the grinding time increases, the particle size decreases. The microstructure of the as-sintered sample is shown in Fig. 6-4.a. It consists of a distribution of blocks composed by coalesced grains. r_g of this sample is 1680 nm. A grinding of 5 minutes produced a sample with separated grains of heterogeneous shapes and sizes, as can be seen in Fig. 6-4.b. The average particle size is r_g= 550 nm in this case. Fig. 6-4.c shows the sample with 30 minutes of grinding, in which the particles (grains) are smaller and more homogeneous size, with r_g= 345 nm. Figure 6-4.d shows a sample with 90 minutes of grinding, with r_g= 220 nm. The samples with 10 and 20 minutes of grinding time have particles with r_g= 470 and 405 nm, respectively. Figure 6-4.e is a gridded amplification of (d).

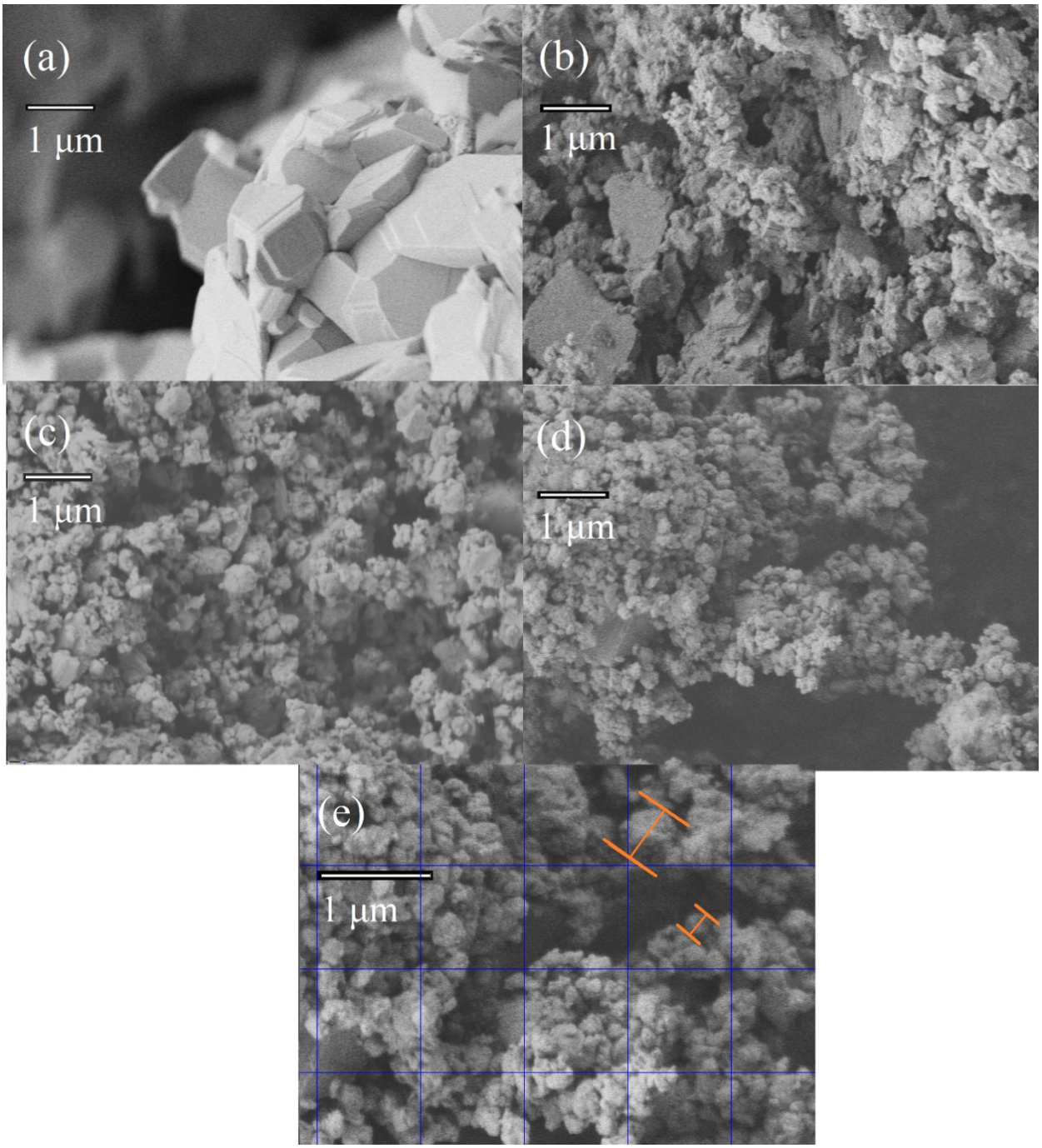

Figure 6-4. SEM micrographs.

Micrographs of the complete set of samples. (a) Sample not ground to reduce its particle size (r_g=1680 nm). (b) Sample with grinding of 5 min, r_g=550 nm. (c) Sample with a grinding of 30 min, r_g=345 nm. (d) Sample with a grinding of 90 min, r_g=220 nm. A decrease in particle size with increasing grinding time can be appreciated. (e) Gridded amplification of (d). It was used to ease the measurement of the particle sizes.

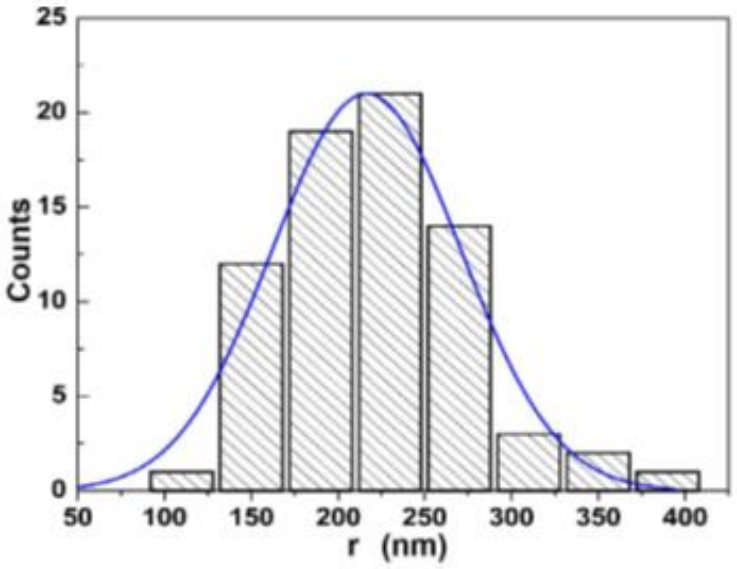

Figure 6-5. Histogram of the particle size distribution.
Sample with 90 minutes of grinding. It can be seen that the particle size distribution can be approximated by a normal distribution. The similarity between the experimental and theoretical distribution (blue line) is evident.

The accepted value of λ, at T=0 K, for $SmFeAsO_{1-x}F_x$, is around 205 nm [10, 11], so the samples with the smallest r_g have a size which is close to the magnitude of the penetration depth, or, at least, they have the same order of magnitude. It is expected that significant changes occur in the properties of the superconducting state of bulk materials, when r_g tends to the characteristic lengths of a superconductor, λ and ξ, or when this size is even smaller.

6.4 Fluorine concentration

The as-sintered sample has a nominal content of fluorine of x=0.2, so this material should have a formula: $SmFeAsO_{0.8}F_{0.2}$. However, during the thermal treatment of the sintering process, the low pressure inside the quartz tube and the high temperatures applied, favor the evaporation of fluorine. Hence, it is expected that the actual amount of fluorine in the final compound is lower than x=0.2. The overlapping between the characteristic x-ray lines for Fe ($L_{\alpha1}$=0.705 keV) and F ($K_{\alpha1}$=0.677 keV) makes difficult to realize a quantitative analysis of the fluorine content by means of energy dispersive X-Ray spectroscopy (EDS). Then, the actual fluorine content of the sample was determined by comparison of the experimental T_c value with the T_c-x phase diagram of samples synthesized in a similar way [12]. This gave a fluorine content of x=0.09, which is close to the optimal doping for the superconductivity in this material.

The fluorine content after grinding was verified. The position of the main peak of each sample can be found in Table 2. These peaks do not show a systematic shift with grinding time (see Fig. 6-6), which would be indicative of a loss of fluorine; instead, the position is randomly

shifted by less than 0.06 in 2θ. Then, it can be concluded that the fluorine content of the sample is not affected by the smooth grinding applied to reduce the size.

Particle size (r_g) nm	Position of the main peak (°)
1680	31.19
550	31.12
470	31.14
405	31.16
345	31.14
220	31.24

Table 2. Position of the main peak of the diffraction pattern.

The shift of the position of the main peaks is inconsistent with a gradual loss of fluoride due to grinding.

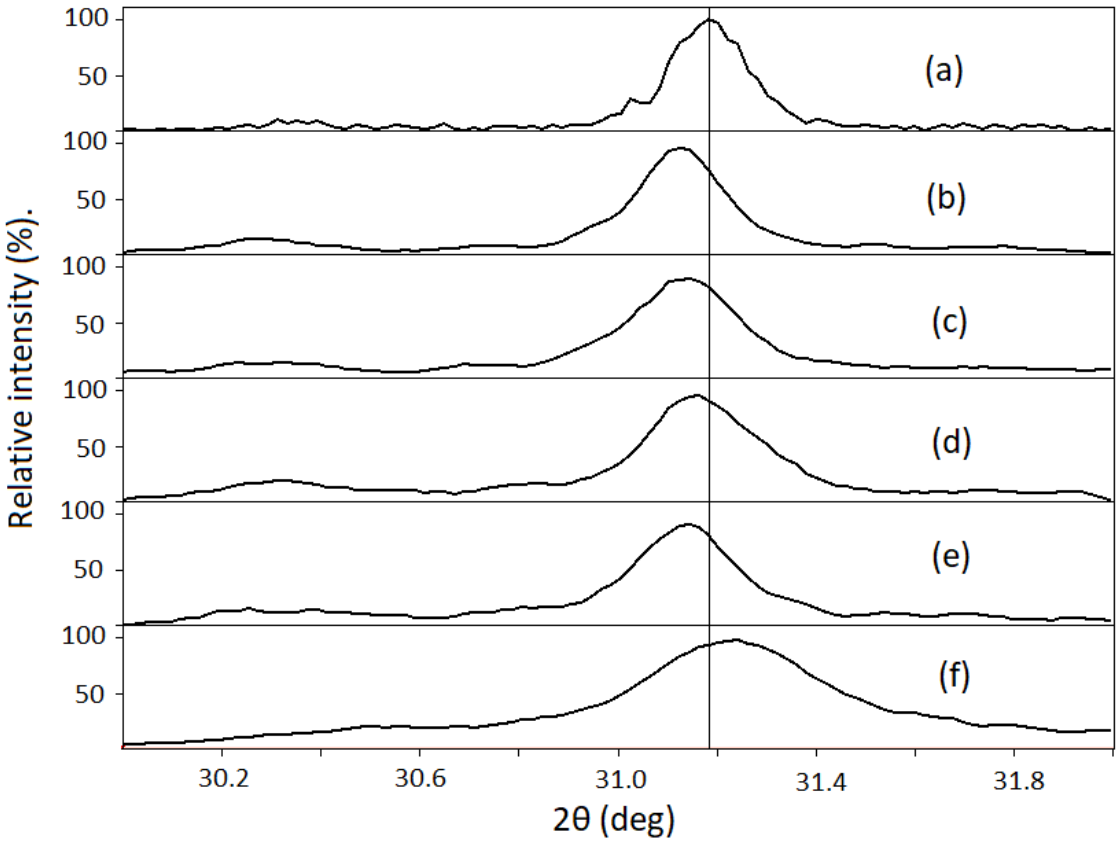

Figure 6-6. X-Ray diffraction patterns for three different particle sizes.

(a) r_g=1680 nm. Peak centered at 31.19°. (b) 550 nm. Peak at 31.12°. (c) 470 nm. Peak at 31.14°. (d) 405 nm. 31.16°. (e) 345 nm. Peak at 31.14°. (c) 220 nm. Peak at 31.24°. The shift of the position of the main peaks is inconsistent with a gradual loss of fluoride due to grinding.

6.5 Electrical properties

The electrical resistance was measured over a range of temperatures, from 3 to 300 K (appendix E has some pictures about it). This experiment was performed only in the sample that was not ground to reduce its particle size (r_g = 1680 nm, as-sintered sample); because the powders compressed into pellets, do not allow reliable measurement of the electrical resistance. This is due to the defective electrical contact between the grains in the compressed sample.

The iron-based superconductors are one of the two main families of compounds that exhibit High-T_c superconductivity, similar to the cooper based superconductors, they are characterized by a layered crystal structure. However, the parent compounds of cuprates are Mott insulators, while in the iron-based superconductors, parent compounds are metals. Fig. 6-7 shows the electrical resistance as a function of the temperature, for the as-sintered sample of $SmFeAsO_{0.91}F_{0.09}$. As can be seen, for the region above T_c, the resistances decrease with temperature, following a linear tendency, which is characteristic of High-T_c superconductors. The onset of the superconducting phase transition is indicated by the abrupt fall to zero, of the electrical resistance at T_c^{onset} = 56.1 K. The ΔT_c transition width (90-10%) is 2 K.

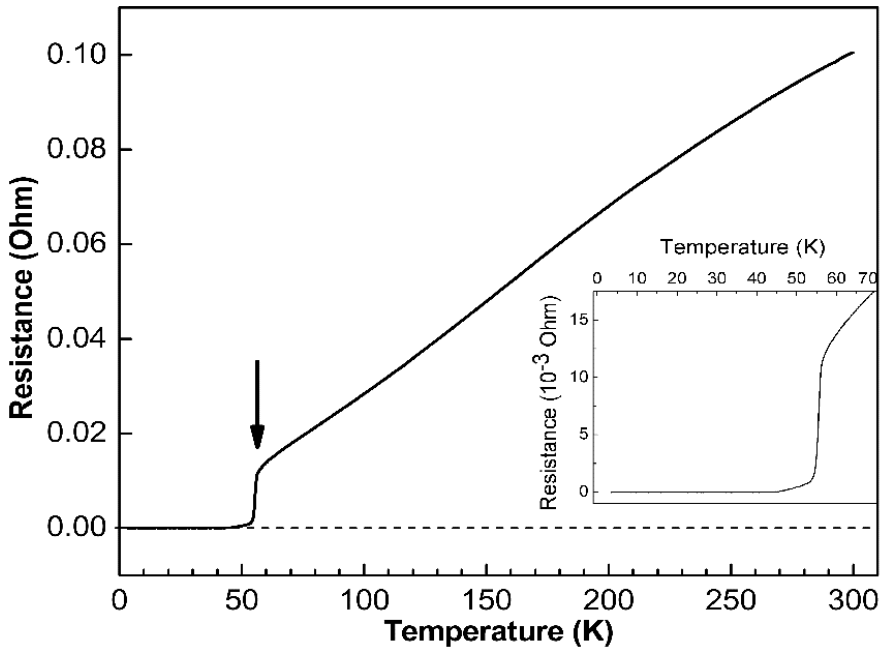

Figure 6-7. Resistance vs. Temperature graph.

Sample of $SmFeAsO_{0.91}F_{0.09}$ (r_g = 1680 nm). The arrow points to the onset of the superconducting transition at T_c^{onset} = 56.1 K. The resistance decreases with temperature, following a metallic behavior. The inset is focused on the low temperature region, The ΔTc transition width (90-10%) is 2 K.

6.6 Effect of the particle size on the magnetic properties of $SmFeAsO_{1-x}F_x$

The main purpose of this work is to analyze the changes in the magnetic properties of the superconducting state of $SmFeAsO_{0.91}F_{0.09}$, when r_g is reduced. Then, it is necessary to explain briefly the effect of the magnetic field in the superconducting state. The measurements were performed in the Physics Department, CINVESTAV Zacatenco. In pursuance of isolating the diamagnetic part of the measurement, the ferromagnetic contribution was subtracted from the corresponding graphs measured under T_c. The detail procedure is explained in appendix F. Also, appendix E includes some pictures of the experimental procedure followed to perform the magnetic measurements.

6.6.1 **Experimental Magnetization vs. Temperature curves**

The Magnetization vs. Temperature (M-T) curves were produced from polycrystalline samples of $SmFeAsO_{0.91}F_{0.09}$, under a low applied magnetic field of 100 Oe. The curves for each sample of different r_g are shown in Fig. 6-8.a. The superconducting nature of the samples is revealed by the diamagnetic behavior of the curves. It can be seen that the signal weakens as r_g decreases, in agreement with previous experimental and theoretical works [8,13]. As a matter of fact, when r_g has the same order of magnitude of λ, a strong suppression of M is observed, according to the already known scaling formula [13] (see also eq. 4.3):

$$M \sim (R/\lambda)^2 \tag{6.1}$$

where R is the radius of the particles in the sample. The inset in Fig. 6-8.a shows that there is no appreciable variation in T_c, which in some way, confirms the invariance in the fluorine content of the samples ground to reduce the particle size. Fig. 6-8.b shows the M-T curves for the as-sintered sample, measured at H=100 and 1000 Oe. The granular character of the sample is revealed by the presence of two transitions. The first one is observed around 19 K, and is called the intergranular transition. It corresponds to the presence of Josephson junctions that couple the individual grains in the sample. It is considered that for temperatures ~20 K or above, the grains in the sample of $SmFeAsO_{0.91}F_{0.09}$ are decoupled, and the magnetic signal measured by the VSM corresponds to the sum of the individual magnetic responses, coming from each particle in the sample.

The transition observed around 56 K is called intragranular (see chapter 4.1), and is determined as the temperature at which the magnetization falls to negative values, and the material becomes diamagnetic. It corresponds to the transition of the individual superconducting grains, from the normal state into the superconducting state [14-16]. The Intragranular transition determines the critical temperature of the material, usually reported in books and journals as T_c. In Fig. 6-8.b, it can be seen that the magnetic signal becomes diamagnetic around 58.8 K. However, the critical temperature of the material must be verified also by R-T measurements.

6.6.2 **Magnetization vs. Magnetic field curves**

Isothermal magnetization was measured in the four quadrants (a complete hysteresis cycle) to study the hysteresis cycle (M-T curves). It was done for the complete set of samples for various ranges of applied magnetic field (H) and at different temperatures (T). The complete hysteresis loop can be divided in regions; for example, the first quadrant of the loop is called *virgin magnetization* region, and gives information about the Meissner state, H_{c1} and H^*. However, the loop also allows to determine H_{irr} and gives information to determine H_{c2}, ξ, λ, J_D, J_{intra} and J_c.

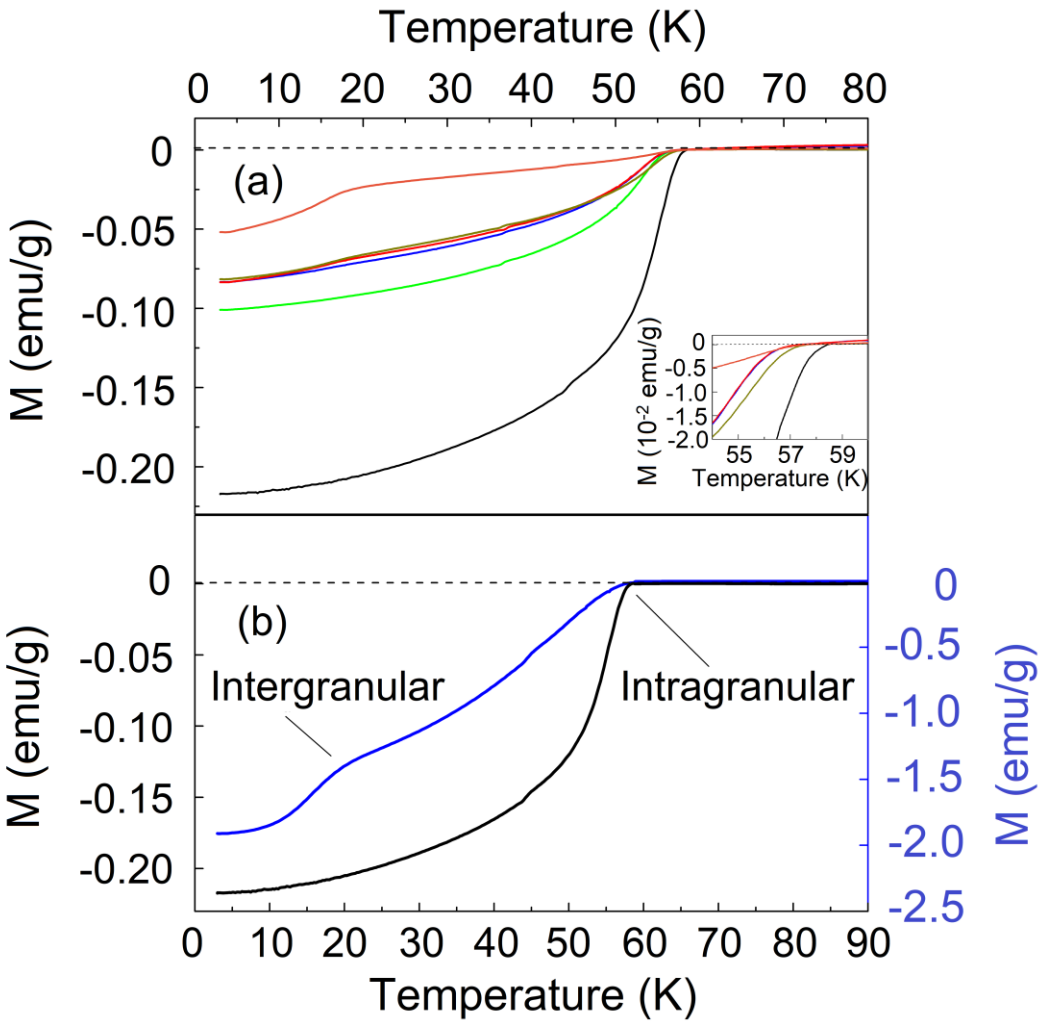

Figure 6-8. Magnetization vs. Temperature curves, for different particle sizes.
(a) Applied field H=100 Oe. From the bottom up Black-particle size of 1680 nm, green-550 nm, blue-470 nm, red-405nm, dark green-345 nm, orange-220 nm. The inset is focused around T_c, the variation of T_c is small. (b) Particle size of 1680 nm. H=100 Oe (black), there is a simple transition around 58 K (intragranular). In blue, the same sample with H=1000 Oe, a second transition appears around 19 K (intergranular). For temperatures above the intergranular transition (~19 K) the grains in the sample are decoupled.

6.6.3 **Virgin magnetization, lower critical field and full penetration field**

Virgin magnetization or *initial magnetization*, is defined as the magnetization region for which the sample has not been previously exposed to a magnetic field, and under the condition that H < H^*, where H^* is the *full penetration field* [8] (see chapter 3.7). H^* is defined as the magnitude of the applied magnetic field, when it reaches the center of the sample.

Figure 6-9 shows the virgin magnetization curves in the range of 0-0.5 T, taken at 20 K. It starts with a linear dependence at low fields, that later bends to the X-axis, for higer values of applied field. The minimum of this curve corresponds to the maximum of magnetization (in absolute value), and is related to H^*. As observed, the graph shows a minimum indicating a strong field dependence on J_c, which is usually described by a modified Bean model as in the cuprates [17, 18]. It is important to observe how the magnitude of M tends to zero, as r_g goes to zero too.

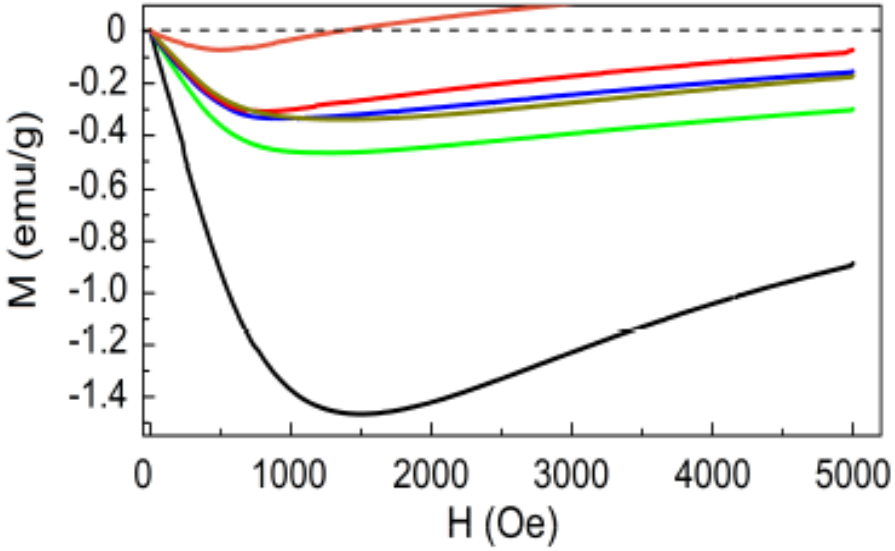

Figure 6-9. M vs. H. Virgin magnetization.

Applied field H= 0 ⟶ 0.5 T. From the bottom up: Black, particle size of 1680 nm; green,550 nm; blue, 470 nm; red, 405 nm; dark green, 345 nm; orange, 220 nm. The curves were taken at 20 K, so it is expected that the measured signal corresponds to intragranular magnetization. M decreases with r_g*, as does the minimum of M, which is related to* H^*.

As usual, the magnitude of H_{c1} was measured as the end of the linear trace in these curves [10]. With this purpose, in the region of the virgin magnetization around the origin the value of H_{c1} was determined carefully (see Fig. 6-10) as the point where the linear tendency (blue line) leaves the experimental points. The H_{c1} values for each r_g are reported in Table 3. As can be seen, the value of H_{c1} diminishes for shorter values of r_g, and in fact, H_{c1} scales with r_g^2. This is in agreement with the well-known calculation of the size dependence of the diamagnetic susceptibility, within the framework of the Ginzburg-Landau theory [19, 20], which predicts that, under weak fields, the susceptibility changes with the particle size as

$$\chi = \frac{{r_g}^2}{4\pi * 10\lambda^2(T)} \tag{6.2}$$

This quadratic dependence is explained as follows: in the Meissner state, the surface currents prevent the entry of the magnetic field (vortices) inside the bulk of the superconductor. As r_g gets smaller, the superficial area in which surface currents flow also decreases, facilitating the entrance of magnetic vortices. Thus, H_{c1} can be reached for lower values of applied magnetic field. This behavior can be observed in Fig. 6-11.

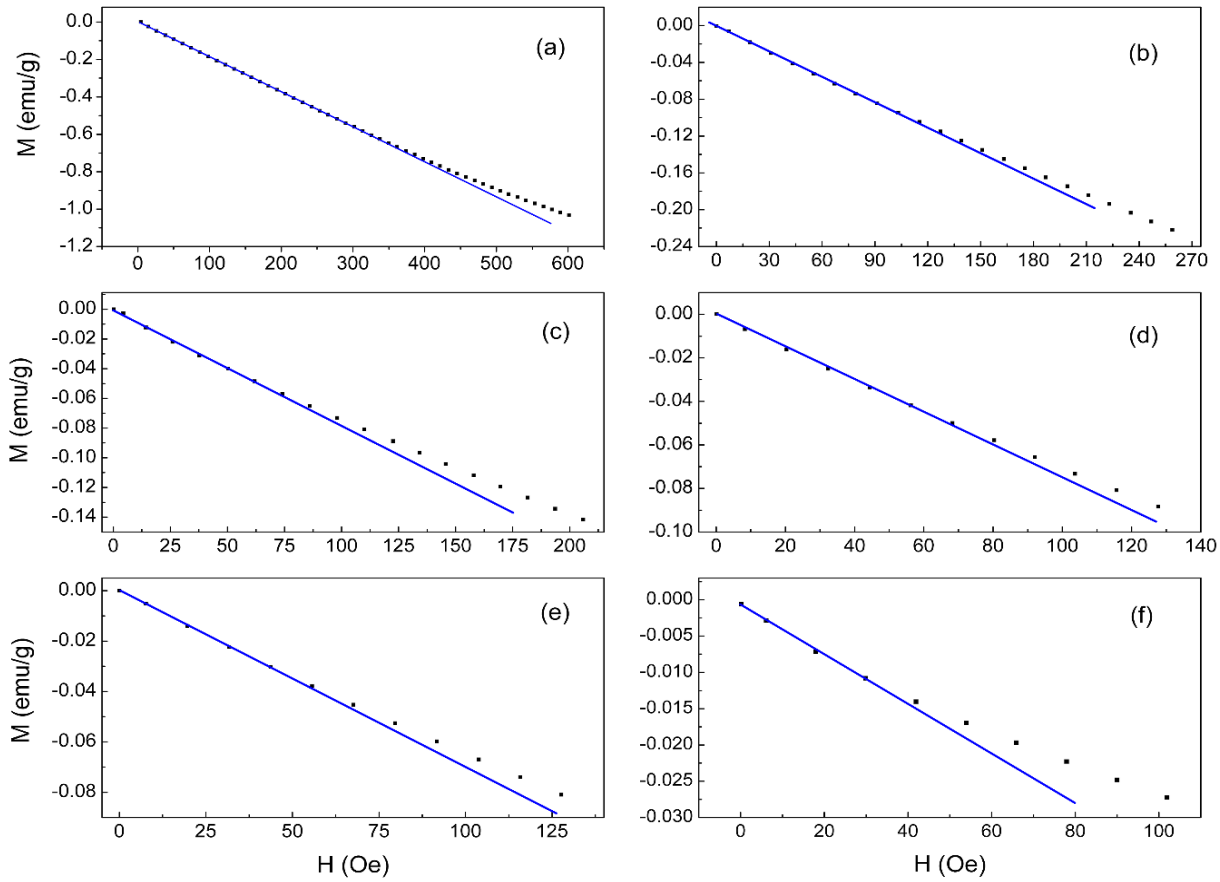

Figure 6-10. Experimental H_{c1}.

M-H curves in the Virgin magnetization region and low H. The point where linear tendency (blue line) leaves the experimental points is considered the experimental value of H_{c1}. (a) r_g=220 nm. (b) r_g=345 nm. (c) r_g=405 nm. (d) r_g=470 nm. (e) r_g=550 nm. (f) r_g=1680 nm.

Particle size (r_g) nm	H_{c1} Oe	H^* Oe
1680	395	1570
550	130	1190
470	85	910
405	70	835
345	55	780
220	30	510

Table 3.Lower critical field and full penetration field.

$SmFeAsO_{0.91}F_{0.09}$ samples. Temperature=20 K. The average particle size (r_g) was estimated from SEM micrographs. The lower critical field (H_{c1}) and the full penetration field (H^*) were measured directly from the virgin magnetization region.

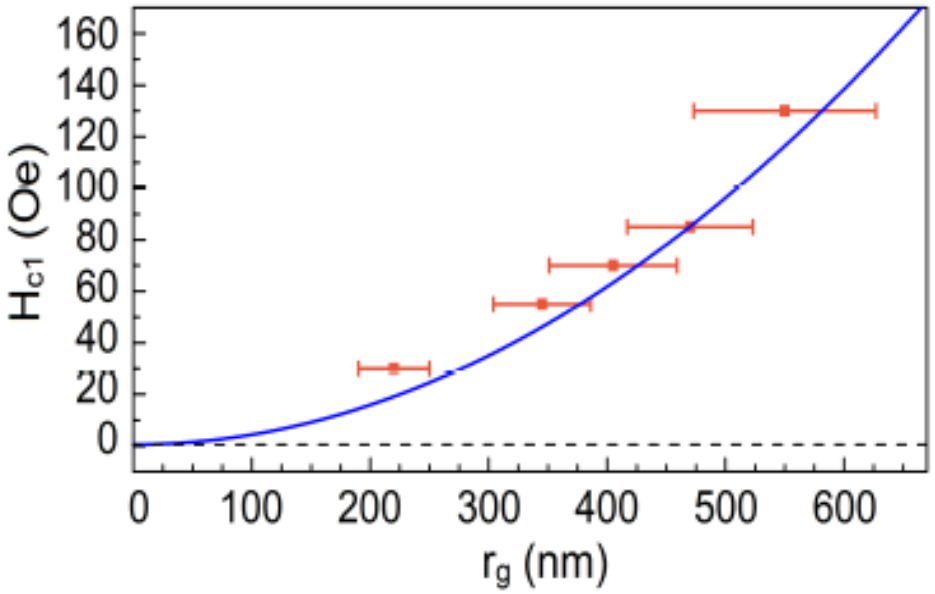

Figure 6-11. Lower critical field (H_{c1}) vs r_g.

The particle size dependence of H_{c1} exhibit a power law behavior. Experimental points are adjusted (blue line) to a quadratic power law: $H_{c1} \sim r_g^2$. The lines in orange indicate the confidence interval for each particle size r_g.

The virgin magnetization region ends when the applied magnetic field reaches the full penetration field (H^*). At this point, the magnetic vortices have invaded the whole sample. If the applied field increases, the density of vortices will increase, and at the same time, the volume of the sample that remains superconducting (not invaded by vortices) will decrease. As a consequence, the absolute value of the magnetization will decay as H increases over H^*. For this reason, the minimum in the virgin magnetization curve is correlated with H^*. The values of H^* are reported in Table 3 for the complete set of samples with different r_g. The magnitude of H^* goes to lower values as r_g tends to zero. For the case of the cuprates superconductors, some

theoretical works have shown that when the volumetric currents decrease exponentially with the applied field, H^* depends on the particle size following a logarithmic law [21]

$$H^* = \ln(1 + \frac{r_g}{r_0}) \tag{6.3}$$

For $SmFeAsO_{1-x}F_x$, the variation of H^* related to r_g also follows a logarithmic law (see Fig. 6-12). The experimental data fit (6.3) well; Thus, the behavior in iron-based superconductors is similar to that found in the cuprates.

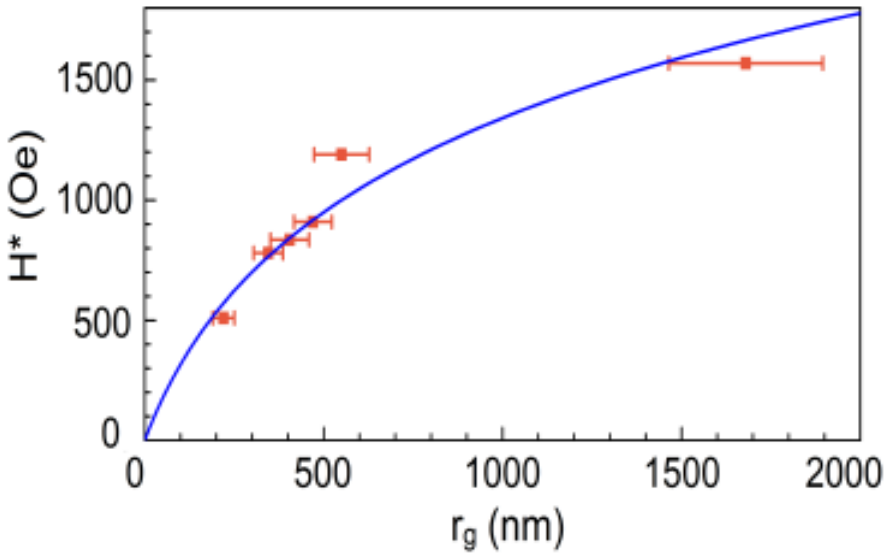

Figure 6-12. Full penetration field (H*) vs. r_g.
Temperature=20 K. Experimental data are adjusted to [21]: $H^* = H_0 ln(1 + \frac{r_g}{r_0})$. The blue line was calculated with H_0=709.97 Oe and r_0=178 nm.

6.6.4 **Anisotropy and particle size distribution**

It is important to clarify that the material studied in the present work is a randomly oriented powder, so that, the experimental magnetic measurements present an averaging effect over different crystallographic directions. For this reason, the values of H_{c1} and H^*, obtained from these measurements, are approximately an average of H_{c1}^c and H_{c1}^{ab} or H_c^* and H_{ab}^*, respectively; but for smaller particles, the magnetic response associated to the currents in the *ab* planes (SmFeAsO has an orthorhombic crystalline structure, which changes to tetragonal by including fluorine [3]) should dominate [22].

The influence of the particle size distribution on the magnetic response has been studied in polycrystalline superconducting samples with a platykurtic size distribution. The diamagnetic signal from a few bigger particles dominates the signal over the rest of small particles [19,23]. Moreover, we have shown that $H_{c1} \sim r_g^2$. Then, we should expect that bigger particles have a

higher H_{c1}. As a result, the H_{c1} determined from a sample with a platykurtic particle size distribution will be more representative of the bigger particles than of the smaller ones. In the present case, as can be observed in Fig. 6-5, long grinding times make the particle size more homogeneous, for this reason, the experimental values of H_{c1} should not be so affected by the particle size distribution, except for the sample with an average size of r_g = 550 nm, where the presence of particles bigger than the average are present. A similar behavior is expected for H^*.

6.6.5 **Effective coherence length**

Different methods have been employed to determine the basic microscopic superconductor parameters [10, 24]. However, for the specific case of powder samples, it is not possible to use the Werthamer-Helfand-Hohenberg approximation (WHH), to calculate the upper critical field H_{c2}, and the magnitude of ξ from electrical measurements. This is due to the defective electrical contacts between the grains that form the sample. For this reason, another method is proposed to determine the effective coherence length (ξ_{eff}) for the set of samples with different r_g values.

The experimental values obtained for H_{c1} were used to calculate the effective coherence length (ξ_{eff}) for each r_g as follows: The effective penetration depth in a type II superconductor is related to the effective coherence length by means of the relation

$$\lambda_{eff} = \lambda \sqrt{\frac{\xi_0}{\xi_{eff}}} \tag{4.2}$$

The Ginzburg-Landau theory for superconductivity defines H_{c1} in terms of λ_{eff} through the equation [25, 26]:

$$H_{c1} = \left(\frac{\Phi_0}{4\pi\lambda_{eff}^2}\right)\left[\ln\left(\frac{\lambda_{eff}}{\xi_0}\right) + 0.5\right] \tag{6.4}$$

By substituting eq. (4.2) into (6.4), H_{c1} can be expressed in terms of ξ_{eff}

$$H_{c1} = \frac{\Phi_0}{4\pi\lambda^2\frac{\xi_0}{\xi_{eff}}}\left[\ln\left(\frac{\lambda}{(\xi_0\,\xi_{eff})^{1/2}}\right) + 0.5\right] \tag{6.5}$$

This new equation can be reordered in an expression for $\xi_{eff} = \xi_{eff}(H_{c1}, \xi_0, \lambda)$. The experimental values of H_{c1} for each r_g, together with the known values for ξ_0 and λ can be used to solve numerically ξ_{eff} for each r_g. In these calculations, the constant values used are Φ_0 = 2.0678 x 10^{-7} gauss cm^2, λ= 220 nm [10] and ξ_0= 2.5 nm [10,11]. The calculated values for ξ_{eff} are shown in Table 4. It can be observed that ξ_{eff} gets shorter as the particle size diminishes and the calculated values are in the accepted range [27, 28].

There is not a clear interpretation for the reduction of ξ_{eff} as the particle size decreases. Even in the case of Type I superconductors, evidence has been found suggesting that for the case of small size superconductors, ξ depends not only on the grain size r_g, but also on the density of states [29]. In the case of HTS, in the clean limit (as in $SmFeAsO_{1-x}F_x$), $\xi < l$, (with l the electron mean-free path), the picture is even more uncertain. However, the quadratic dependence of ξ_{eff} on r_g (see Table 4 and Fig. 6-13) agrees with the model proposed by Fiolhais and Birman [30], in which the decrease of ξ with r_g, is related to the discretization of the energy levels at the nanoscale.

Particle size (r_g) nm	H_{c1} Oe	H^* Oe	ξ_{eff} nm	Ground state energy (E_1) meV
1680	395	1570	ξ_0=2.5	3.6
550	130	1190	1.87	25.5
470	85	910	1.17	21.9
405	70	835	0.94	23.7
345	55	780	0.72	25.0
220	30	510	0.37	31.6

Table 4. Effective coherence length (ξ_{eff}) and ground state energy (E_1).
$SmFeAsO_{0.91}F_{0.09}$ samples. Temperature=20 K. r_g, H_{c1} and H^* are the same as in Table 3. The effective coherence length (ξ_{eff}) was calculated as of H_{c1}. In turn, E_1 was calculated from ξ_{eff} values.

As in most nanoscale solid state systems, important quantum size effects arise in small superconductors. For type I superconductors, the energy spectrum changes from an initially continuous to a discrete energy spectrum. The quantum confinement of the wave vector leads to the appearance of discrete energy levels [31]. The same phenomenon is expected in type II superconductors, but in this case, it has been proposed that a scalar Higgs-like field is present in the superconducting region [32]. The fluctuations of this field are negligible except for small superconductors (r_g = λ), where fluctuations between the superconductor walls originate a new ground state, leading to a discretization of the energy spectrum for particles in the mesoscopic scale. It is also expected that this new ground state increases over superconducting condensation energy. Following this idea, an expression for the ground state energy of a mesoscopic type II superconductor can be obtained [30]:

$$E_1 = \frac{3\sqrt{2}\pi^2 \hbar c \xi}{2r_g^2} \tag{6.6}$$

where *c* is the speed of light and ξ is the coherence length. From eq. (6.6), a quadratic dependence of ξ on r_g can be inferred. Moreover, as mentioned before, the calculated values for ξ_{eff} follow this quadratic behavior, as can be seen in Fig. 6-13, and in the results of Table 4. This means that the present experimental results support the model proposed by Fiolhais et al [30]. Nevertheless, this must be valid only for small particles; for big enough particles, ξ_{eff} should reach its maximum value ξ_0=2.5 nm. Taking $\xi=\xi_{eff}$ in eq. (6.6), we can use the values of Table 4 and

calculate the energy of the ground state E_1 for each r_g. The results are shown in Table 4. The value of E_1 for r_g = 1680 nm was estimated with $\xi_{eff}=\xi_0$ =2.5 nm. As can be seen E_1 increases for shorter values of r_g between 470 to 220 nm (inset of Fig. 6-13), following a nearly linear tendency (blue line).

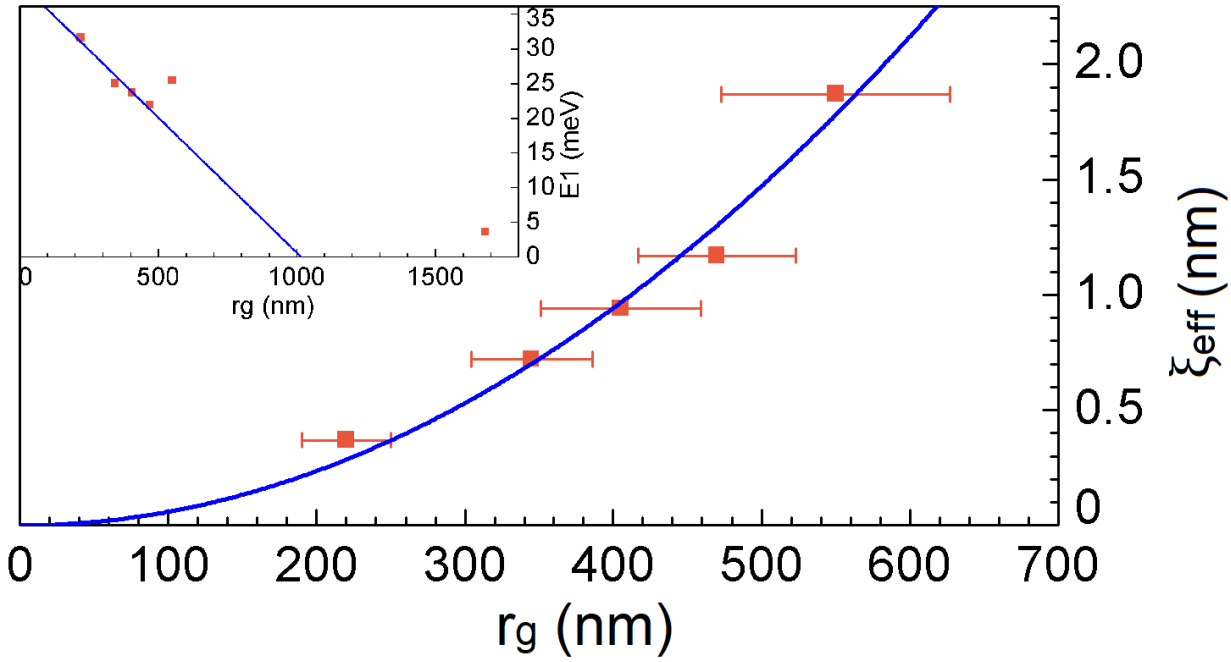

Figure 6-13. Effective coherence length (ξ_{eff}) vs. r_g.
The calculated values of ξ_{eff} follow a quadratic power law: $\xi_{eff} \sim r_g^2$ (blue line). The inset shows ground state energy (E_1) vs. r_g. There is a linear tendency for 220 .$\leq r_g \leq$470 nm (blue line).

6.6.6 **Irreversibility field**[12]

The irreversibility field (H_{irr}) introduced in chapter 3.7 points to the boundary between the vortex glass/liquid regions. Above H_{irr}, flux pinning vanishes and the magnetic vortices can move easily from one pinning center to another [33], the result being that the hysteresis loop closes. Then, H_{irr} can be determined as the point where the upper and lower branches join, and the loop becomes reversible [34-36]. For H ≥ H_{irr}, the electrical transport current presents dissipation and J_c drops. Therefore, H_{irr} limits the range of practical applications [37]; for example, the manufacture of high-magnetic field magnets requires superconducting materials with a high value of H_{irr}. On the other hand, H_{irr} depends on the flux pinning strength and the magnetic anisotropy of the material, but also on the thickness of the film or the average powder particle size of the sample [38, 40].

H_{irr} was determined directly from the M-H experimental curves as the point where the hysteresis loop closes. Figure 6-14 illustrates the procedure for the sample with r_g=1680 nm. The

[12] For reasons of practicality, SI units are used in some cases in the sections related with vortex pinning.

compound $SmFeAsO_{1-x}F_x$ has a very high value of $H_{c2}(0)$; therefore, H_{irr} must be also high, so that the hysteresis loop was measured at T= 50 K and H_{max}= 7 T, facilitating the observation of H_{irr}. This procedure was repeated for the complete set of samples. In this way, the behavior of H_{irr} is studied as the particle size decreases from r_g=1680 nm, down to when r_g reaches the scale of the penetration depth (λ=220 nm). The results can be found in Table 5. The measured H_{irr} for the sample with larger particle size is similar to the accepted magnitudes for H_{irr} near T_c in this same material [40].

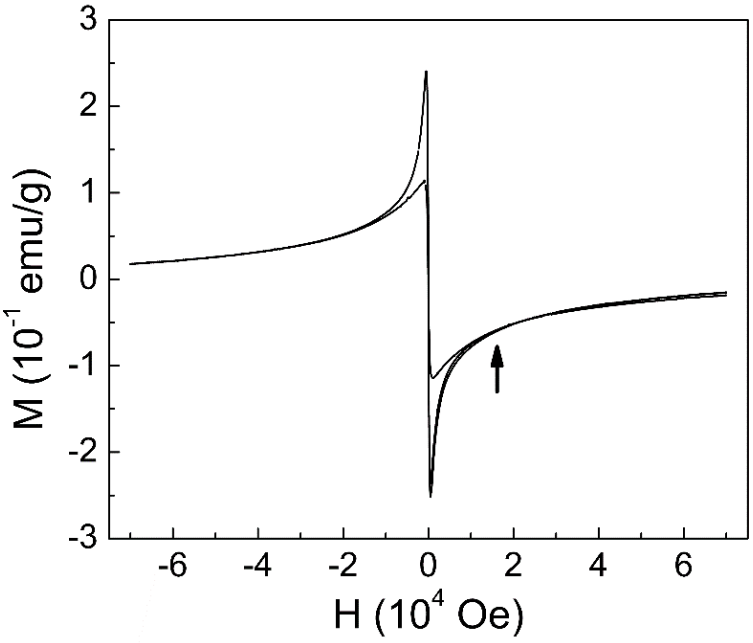

Figure 6-14. Determination of the irreversibility field H_{irr}.
M-H curve of a sample of $SmFeAsO_{0.91}F_{0.09}$. r_g= 1680 nm. -7 T ≤ H ≤ 7 T. The curve was measured at T= 50 K, with the sample in the superconducting state. The arrow indicates the point where the hysteresis loop closes.

Particle size (r_g) nm	H_{irr} (Oe)	H_{c2}(50 K) (T)	H_{c2}(O) (T)
1680	15874	22	107
550	12175	10.8	52.5
470	9921	7	34
405	9109	5.9	28.7
345	8235	4.9	23.2
220	7161	3.8	18.5

Table 5. Irreversibility field (H_{irr}) and upper critical field (H_{c2})
$SmFeAsO_{0.91}F_{0.09}$ samples. The experimental values of H_{irr} were obtained by direct measurement from the M-H curves (T=50 K). H_{c2}(50 K) was calculated as of H_{irr}. In turn, H_{c2}(0) was estimated from H_{c2}(50 K) values.

Figure 6-15 shows the graph of the experimental values obtained for $H_{irr}^{(3-2\gamma)/2} \approx H_{irr}^{1/3}$ vs. r_g, with γ=1.165. As can be seen, the values of $H_{irr}^{1/3}$ for $220 \leq r_g \leq 550$ nm follow a decreasing linear tendency with r_g. This is in agreement with the limit for small particles (correlation length $L > r_g$) of the flux creep model proposed by Matsushita [38,41-43]

$$H_{irr}^{\frac{3-2\gamma}{2}} = \frac{K}{T}\left[1 - \left(\frac{T}{T_c}\right)^2\right]^m \tag{6.7}$$

with

$$K = \frac{4.23 g^2 A\, r_g}{\zeta\, Ln\left(\frac{B a_f \nu_0}{E_c}\right)} \tag{6.8}$$

where a_f is the fluxoid spacing, ν_0 is the oscillation frequency of the flux bundle, ζ is a constant that depends on the type of the pinning center, E_c is the electric field criterion, g is a constant proportional to the anisotropy of the coherence length and the dimensionality of the sample, m is a numerical parameter related to the magnetic field dependence of the creep-free critical current density, and r_g is the thickness of the thin film or the average diameter of the particles in the case of powder samples [38, 44]. A is a constant related with the dimensionality of the sample [45].

Then, the effect of reducing the particle size is a decrease in H_{irr}. As can be seen in Fig. 6-15, for big enough particles that reach the pinning correlation length (like r_g=1680 nm), the influence of flux creep is less relevant and the linear tendency decreases. Thus, $H_{irr}^{1/3}$ tends to its bulk value, and of course the same happens for H_{irr}. The dotted line is a guide to illustrate this point. The observed behavior can be explained by the collective flux creep theory: it establishes that vortex thermal activation is stronger in small particles [42], but is less relevant as the particle size increases. The inset shows H_{irr} vs. r_g, for $220 \leq r_g \leq 550$ nm. The irreversibility field follows a power law dependence on r_g, in agreement with eqs. (6.7) and (6.8) (see inset of Fig. 6-15) raised to the third power.

The anisotropy of the material is also related with the strength of the vortex pinning. It has been observed that introducing nano-scale columnar defects, the anisotropy caused by the layered structure of the material is reduced, and the intergranular critical current density J_c increases, due a more intense magnetic vortex pinning [46,47].

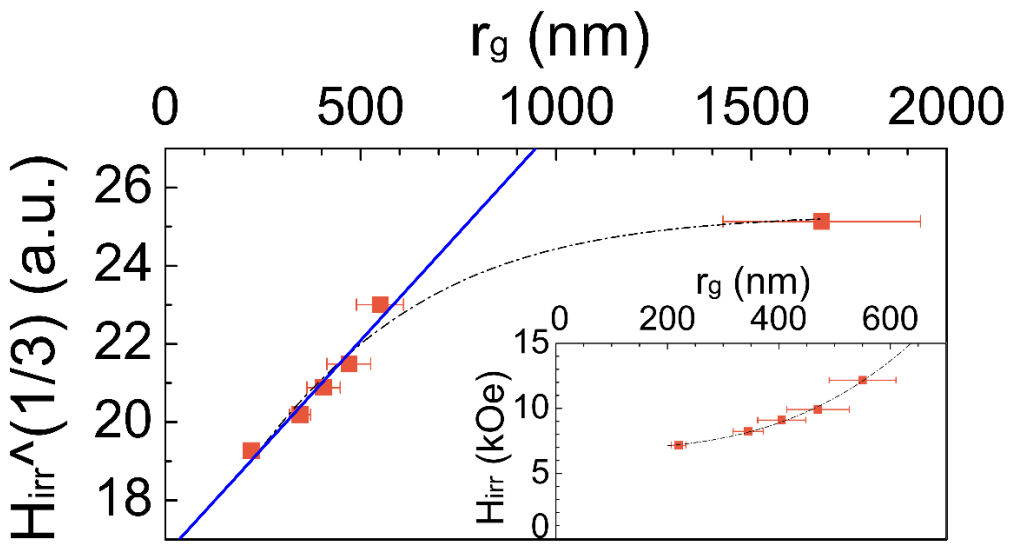

Figure 6-15. Cubic root of the irreversibility field ($H_{irr}^{1/3}$) vs. r_g.
The experimental values of $H_{irr}^{(3-2\gamma)/2} \approx H_{irr}^{1/3}$ for small particles (for $220 \leq r_g \leq 550$ nm) follow a decreasing linear tendency diminishing with r_g (blue line). For big enough particles (r_g=1680 nm), this tendency changes and $H_{irr}^{1/3}$ reaches a saturation value (dotted line). The inset shows H_{irr} vs. r_g, for $220 \leq r_g \leq 550$ nm. The irreversibility field follows a cubic power law, in agreement with eq. (6.7) and (6.8) raised to the cube. The dotted lines are guides for the eyes.

6.6.7 **Upper critical field**

An applied magnetic field destroys superconductivity by breaking the Cooper pairs in two different ways. One, via the orbital pair breaking effect, related with the Lorentz force acting on the charge of the paired electrons (Cooper pair) with opposite momenta. The second mechanism for destruction of superconductivity is the Pauli pair breaking mechanism, also known as spin/paramagnetic effect. It consists in the alignment of the spin singlet of Cooper pairs into a triplet, due to the applied magnetic field [48].

Early calculations of $H_{c2}(0)$ were based on Werthamer-Helfand-Hohenberg approximation (WHH), and suggest values between 150-400 T for $H_{c2}(0)$ [14, 40, 49, 50], a huge critical field over the BCS paramagnetic limit. However, nowadays it is not possible to generate a magnetic field or magnetic pulses of that magnitude. Other estimations that consider the specific properties of IBSC predict a lower value around 100 T.

In the present work, H_{c2} was calculated by numerical solution of a model based on the flux creep theory [38,51]

$$H_{irr}^{\frac{3-2\gamma}{2}} = \left(\frac{K}{T}\right)^2 \left[1 - \left(\frac{T}{T_c}\right)^2\right]^{m-\gamma} \left(1 - \frac{H_{irr}}{H_{c2}}\right)^{\delta} \qquad (6.9).$$

This is actually the equation used to derive (6.7), but here the factor $(1-\frac{H_{irr}}{H_{c2}})^{\delta}$ is preserved with the purpose to estimate H_{c2}. The variables have the same meaning as for eqs. 6.7 and 6.8. The numerical parameter δ is related to the magnetic field dependence of the creep-free critical current density. The value of K=355 is twice the value for a powder sample of $SmFeAsO_{0.85}$ (with no fluorine atoms) [51], with the use of SI units. The values m=1.5 and δ=2 are in accordance to the magnitudes used for other High-T_c layered superconductors [38]. The reduced temperature is $t=\frac{T}{T_c}=\frac{50\ K}{56.1\ K}=0.89$, γ=1.165 and H_{irr} was taken from Table 5.

With the parameter values mentioned above, eq. (6.9) was solved. The result was H_{c2}(50 K)= 22 T for the sample with r_g=1680 nm. This result is close to the values obtained in [40] for temperatures near T_c (with t≈0.95) for this same material. $H_{c2}(0)$ was estimated by using the empirical temperature dependence of the upper critical field [51]

$$H_{c2}(T)=\ H_{c2}(0)[1-(\frac{T}{T_c})^2] \tag{6.10}$$

$H_{c2}(0)$ is shown in the inset of Fig. 6-16.

The procedure explained before was repeated for the complete set of samples. The results can be found in Table 5 and Figure 6-16. It can be seen that for $r_g \sim \lambda$, H_{c2}(50 K) decreases following a power law of the form $r_g^{3/2}$ (blue line), while for r_g=1680 nm, H_{c2} has reached its bulk value. A value of $H_{c2}(0)$= 107 T was estimated for the sample with largest particle size. This magnitude is in agreement with some studies made using intense magnetic pulses of up to 60 T [52], and in which the spin paramagnetic effect was taken in account [40]. The behavior of H_{c2}(0) is similar to that observed in H_{c2}(50 K), see inset in Fig. 6-16.

The early calculations of $H_{c2}(0)$ based on the WHH approximation fail in two points: they were based mainly on the orbital pair breaking effect, which dominates pair breaking of conventional superconductors, in spite of $SmFeAsO_{1-x}F_x$ being an unconventional one. In the last case, the spin paramagnetic effect plays an important role in the destruction of the Cooper pairs [53]. In second place, the WHH approximation os based in a material in the dirty limit, with $l < \xi_{eff}$ [54]. Nevertheless, due to the small size of ξ_{eff}, it is unlikely that $SmFeAsO_{1-x}F_x$ can reach this last condition, and in consequence, the material is considered in the clean limit ($l >> \xi_{eff}$). The estimations of H_{c2} made here are much lower than the ones proposed early after the discovery of IBSC. However, by the reasons exposed above, the values of H_{c2}(50 K) and $H_{c2}(0)$, calculated here on the basis of the flux creep model, are proposed as a more accurate estimation. Moreover, the decrease in H_{c2} is in accordance with the observed behavior of H_{irr}.

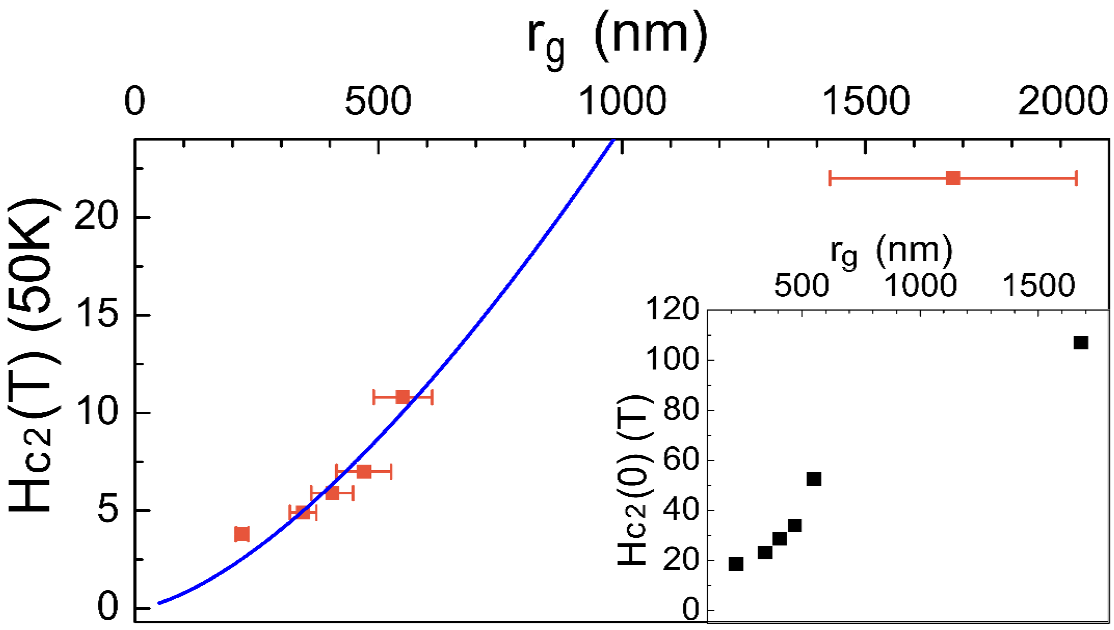

Figure 6-16. Calculated values of H_{c2} vs. r_g.
Values of H_{c2}, estimated from H_{irr} experimental values measured at a temperature of 50 K. The inset shows the values of $H_{c2}(0)$ estimated from H_{c2}. Magnetic fields are expressed in Tesla.

6.6.8 **Critical current density**

In *polycrystalline* samples of IBSC, two critical current densities have to be considered: the intragranular critical current density (J_{intra}), that corresponds to the volume currents inside each single grain in the sample, and the intergranular current density J_c, which corresponds to the current that flows across the grains, over the whole sample [55,56]. Moreover, the depairing critical current density (J_D) is defined as the highest current density that a superconductor can reach before the breaking of the Cooper pairs. In polycrystalline high temperature superconductors like $SmFeAsO_{1-x}F_x$, it has been noticed that $J_c << J_{intra} < J_D$.

The decrease of J_c is caused mainly, by the presence of large misorientations contiguous grain, the *weak-link problem* [57-59]. Due to the very small ξ of IBSC, the boundaries between misoriented grains cause the suppression of the superconducting order parameter, and, as a result, the material is divided into grains coupled by weak Josephson junctions. The pinning of Josephson vortices at the boundary, is weaker than the one of Abrikosov´s vortices at the bulk. Then, the grains are decoupled for current densities much lower than J_{intra} [60]. Any attempt to enhance J_c, is done with the purpose to reach the upper bound given by J_{intra}.

J_{intra} was determined experimentally by measuring ΔM from M-H hysteresis loops, measured at T=20 K. This temperature and the high applied magnetic field ($-5000 \leq H \leq 5000$ Oe),

favors the rupture of the Josephson junctions between the grains of the sample. Then, by using [61]

$$J_{intra} = \frac{30\Delta M}{r_g} \tag{6.11}$$

where ΔM is the magnetization loop width [61], the relation J_{intra} vs. H was calculated. The results[13] can be seen in Fig. 6-17. On the other side, J_c was determined in a similar way as J_{intra}, but the hysteresis loop was measured at 5 K, under a low applied magnetic field ($-200 \leq H \leq 200$ Oe). Both conditions prevent the rupture of the Josephson junctions that couple the grains in the sample. The calculation gave J_c= 6.56x10^5 A·m^{-2}, for the sample with r_g=1680 nm. J_c was not calculated for the other samples, since the milling process prevents reliable electrical measurements. J_D was calculated in the framework of the Ginzburg-Landau theory [58]

$$J_D = \frac{\Phi_0}{3\sqrt{3}\pi\mu_0\lambda_{eff}^2\xi_0} \tag{6.12}$$

with Φ_0= 2.0678 x 10^{-15} Tesla m^2, μ_0= 4π x 10^{-7} Wb (A m)$^{-1}$, and ξ_0=2.5 nm. λ_{eff} was calculated with eq. (6.4) and the values of ξ_{eff} were taken from Table 4. The complete set of results can be found in Table 6 and Figure 6-18.

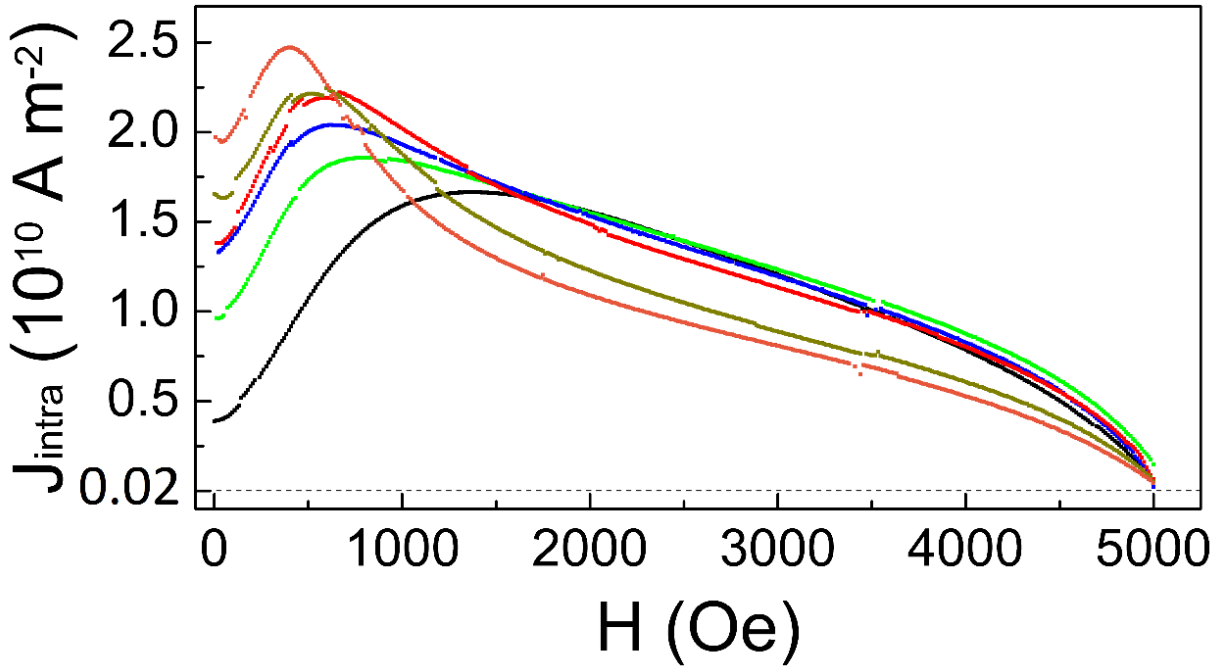

Figure 6-17. Experimental intragranular critical current density (Jintra).
T= 20 K. The curve in black corresponds to r_g=1680 nm, in green, 550 nm; in blue, 470 nm; in red, 405 nm; in dark green, 345 nm; and in orange, 220 nm.

[13] Eq. 6.11 requires ΔM in emu·cm^{-3}, r_g in cm, and gives J_{intra} in A·cm^{-2}. These units are in accordance with the scale of the experiments. However, the results are presented in SI units (A·m^{-2}).

Particle size (r_g) nm	λ_{eff} (nm)	J_D (10^{11} A·m^{-2})
1680	220	8.331
550	254	6.250
470	321	3.913
405	358	3.146
345	410	2.399
220	572	1.232

Table 6. Effective penetration depth (λ_{eff}) and depairing critical current density (J_D).
$SmFeAsO_{0.91}F_{0.09}$ samples. T=20 K. The values of λ_{eff}, were calculated from the estimated values of ξ_{eff}. In turn, λ_{eff} was used to calculted J_D.

The magnitudes obtained for J_{intra} and J_c are in accordance with the results of other works [56,63,64]. The same happens for the calculation of J_D [47]. As can be seen in Fig. 6-17, in the region of low H appears a peak in the maximum of J_{intra}. This maximum value increases as $r_g \rightarrow 0$. Moreover, the maximum value shifts to lower values of H as $r_g \rightarrow 0$. As H further increases, J_{intra} falls to a magnitude common for all samples. This fall is sharper as r_g decreases. Only in the case of $r_g \sim \lambda$ (220 and 345 nm), it is observed that J_{intra} falls below the value shown by the other samples.

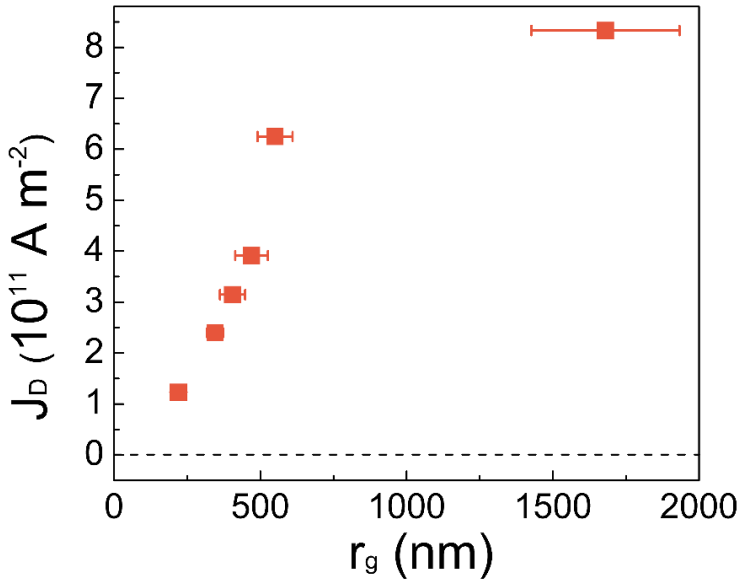

Figure 6-18. Calculated depairing critical current density (J_D).
T=20 K. r_g ranges from bulk size (1680 nm) to the scale of λ (220 nm). For magnitudes of r_g close to λ, J_D follows a linear dependence, similar to that observed in H_{irr}.

J_{intra} is determined by the magnetic vortex pinning, and in the case of charged-doped IBSC, the critical current is composed by the sum of two components. Hence, the behavior described above can be explained by considering two different pinning mechanisms: *strong pinning* and

weak collective pinning. The contribution of each one to J_{intra} is determined by the intensity of the applied field. For low H, the interaction between vortices is negligible and J_{intra} can be considered independent of H. In this regimen, strong vortex pinning dominates. This mechanism is caused by large and disperse defects that function as pinning centers, and also by the coexistence of phases (several nm in size) with variations in the dopant-atom density across the material [65,66]. In the intermediate H regime, vortex-vortex interaction appears and then $J_{intra} \propto H$. In this case, weak collective pinning dominates; it is caused by dopant atoms which acts as quasiparticle scatterers, also pinning the vortex lines due to local variations in the dopant-atom density [65,66].

Regarding J_D, it is one (or two) order(s) of magnitude larger than J_{intra} (Fig. 6-17 and 6-18). J_D decreases linearly with r_g, for $r_g \sim \lambda$, while for larger particles (r_g=1680 nm) it reaches the bulk value. If figures 6-15 and 6-18 are compared, it is evident that $H_{irr}^{1/3}$ and J_D have a very similar behavior.

On the other hand, the calculated value for J_c is extremely low, but is in accordance with the observation that *randomly oriented polycrystalline* samples of $SmFeAsO_{1-x}F_x$, have the lowest J_c when compared to thin films or single crystals [56,64]. This low value is caused by the well-known *weak link problem* associated with the granular nature of the material. Nevertheless, the compound $SmFeAsO_{1-x}F_x$ has a low J_c anisotropy. Then, in contrast with cuprates, the fabrication of wires or tapes would not require texturing processes [67]. Moreover, $SmFeAsO_{1-x}F_x$ has a strong pinning potential [68]. Both characteristics give a good potential for high magnetic field applications. A possible solution to improve intergranular vortex pinning and elevate J_c, is by reducing the anisotropy caused by the layered structure of $SmFeAsO_{1-x}F_x$, with the introduction of nano-scale columnar defects [47,48].

6.7 Bibliography

[1] Kamihara, Yoichi; Watanabe, Takumi; Hirano, Masahiro; Hosono, Hideo (2008). Iron-Based Layered Superconductor $La[O_{1-x}F_x]FeAs$ (x = 0.05–0.12) with T_c = 26 K. Journal of the American Chemical Society. 130 (11): 3296–3297. Doi:10.1021/ja800073m.

[2] Kamihara, Yoichi; Hiramatsu, Hidenori; Hirano, Masahiro; Kawamura, Ryuto; Yanagi, Hiroshi; Kamiya, Toshio; Hosono, Hideo (2006). Iron-Based Layered Superconductor: LaOFeP. J. Am. Chem. Soc. 128 (31): 10012–10013. Doi:10.1021/ja063355c.

[3] M Fujioka et al. Supercond. Sci. Technol. 26 085023 (2013). Phase diagram and superconductivity at 58.1 K in α-FeAs-free $SmFeAsO_{1-x}F_x$. Doi:10.1088/0953-2048/26/8/085023.

[4] Hyun-Sook Lee et al. Effects of two gaps and paramagnetic pair breaking on the upper critical field of $SmFeAsO_{0.85}$ and $SmFeAsO_{0.8}F_{0.2}$ single crystals. Phys. Rev. B 80, 144512 (2009). https://doi.org/10.1103/PhysRevB.80.144512.

[5] S. J. Singh, J. Shimoyama, A. Yamamoto, H. Ogino, K. Kishio. Transition Temperature and Upper Critical Field in $SmFeAsO_{1-x}F_x$ Synthesized at Low Heating Temperatures. IEEE Transactions On Applied Superconductivity 23, 7300605 (2013). https://arxiv.org/abs/1303.4163.

[6] H. Ponce-Flores, A. Conde-Gallardo. Influence of the Oxygen Excess in the Synthesis of $NdFeAsO_{1-x}F_x$ Superconductors. J. Supercond. Novel Magn. 27(3), 673 (2014). https://doi.org/10.1007/s10948-013-2336-8.

[7] L. Malavasi, G.A. Artioli, C. Ritter, M.C. Mozzati, B. Maroni, B. Pahari, A. Caneschi. Phase Diagram of $NdFeAsO_{1-x}F_x$: Essential Role of Chemical Composition. J. Am. Chem. Soc. 2010, 132, 7, 2417-2420. https://doi.org/10.1021/ja910426d.

[8] S. Senoussi, F. Pesty. Magnetization of organic superconductors: influence of defects. Studies of High Temperature Superconductors: Diverse Superconducting Systems and Some Miscellaneous Applications, vol. 37, Nova Science Publishers, Huntington, NY, USA, 2001.

[9] J.R. Waldram, A. Porch, H-M Cheah. Measurement of the microwave conductivities of high-Tc superconducting powders. Physica C 232 (1994) 189-198. https://doi.org/10.1016/0921-4534(94)90313-1.

[10] C. Ren and Z.S. Wang and H.Q. Luo and H. Yang and L. Shan and H.H Wen. Temperature dependence of the lower critical field H_{c1} in $SmFeASO_{0.9}F_{0.1}$ and $Ba_{0.6}K_{0.4}Fe_2As_2$ iron-arsenide superconductors. Physica C: Superconductivity 469(9), 599 (2009). https://doi.org/10.1016/j.physc.2009.03.015.

[11] L. Fang et al. Huge critical current density and tailored superconducting anisotropy in $SmFeAsO_{0.8}F_{0.15}$ by low-density columnar-defect incorporation. Nature Communications 4, 2655 (2013). https://doi.org/10.1038/ncomms3655.

[12] Y. Kamihara, T. Nomura, M. Hirano, J.E. Kim, K. Kato, M. Takata, Y. Kobayashi, S. Kitao, S. Higashitaniguchi, Y. Yoda, M. Seto, H. Hosono. Electronic and magnetic phase diagram of superconductors, $SmFeAsO_{1-x}F_x$. New J. Phys. 12(3), 033005 (2010). https://doi.org/10.1088/1367-2630/12/3/033005.

[13] John R. Clem, Vladimir G. Kogan. Theory of the Magnetization of Granular Superconductors: Application to High-T_c Superconductors. Japanese Journal of Applied Physics, Volume 26, Supplement 26-3, Part 2. doi:10.7567/jjaps.26s3.1161.

[14] C. Senatore, R. Flükiger, M. Cantoni, G. Wu, R. H. Liu, X. H. Chen. Upper critical fields well above 100 T for the superconductor SmFeAsO0.85F0.15 with Tc=46 K. Phys. Rev. B 78 (2008) 054514. doi:10.1103/Phys- RevB.78.054514.

[15] Thomas W. Krause, R.K. Nkum W.R. Datars. Intergrain and intragrain superconductivity in Sn- and Sb-doped $Bi_{1.7}Pb_{0.3}Sr_2Cu_3O_y$, Physica C: Superconductivity 210 (3) (1993) 333 – 342. https://doi.org/10.1016/0921-4534(93)90975-V.

[16] L. Wang, Z. Gao, Y. Qi, X. Zhang, D. Wang, Y. Ma. Structural and critical current properties in polycrystalline $SmFeAsO_{1-x}F_x$. Superconductor Science and Technology 22 (1) (2009) 015019. doi:https://doi.org/10.1088/0953-2048/22/1/015019.

[17] D.-X. Chen, A. Sanchez, J. Nogues, J. S. Muoz. Bean's, Kim's, and exponential critical-state models for High-T_c superconductors. Phys. Rev. B 41 (1990) 9510–9512. doi:10.1103/PhysRevB.41.9510.

[18] P.Chaddah, G. Ravi Kumar, A.K. Grover, C. Radhakrishnamurty, G.V. Subba Rao. Critical state model and the magnetic behavior of High-T_c superconductors. Cryogenics 29 (9) (1989) 907 – 914. https://doi.org/10.1016/0011-2275(89)90204-X.

[19] B. Mühlschlegel. Superconductivity of small particles. Physica B: Condensed Matter 203 (3) (1994) 444–447. https://doi.org/10.1016/0921-4526(94)90094-9.

[20] B. Mühlschlegel, D. J. Scalapino, R. Denton. Thermodynamic properties of small superconducting particles. Phys. Rev. B 6, 1767 (1972). https://doi.org/10.1103/PhysRevB.6.1767.

[21] S. Senoussi, C. Aguillon, P. Manuel. The origin of the low field peak in the hysteresis cycle of High-Tc oxides and the influence of magnetic pinnings, Physica C: Superconductivity 175 (1) (1991) 202 – 214. https://doi.org/10.1016/0921-4534(91)90254-V.

[22] V.G. Kogan, J.R. Clem. Anisotropy effects upon the magnetic properties of high-Tc superconductors, Jpn. J. Appl. Phys. 26 (S3-2) (1987) 1159. https://doi.org/10.7567/jjaps.26s3.1159.

[23] Y.L. Zuev, E.D. Specht, C. Cantoni, D.K. Christen, J.R. Thompson, R. Jin, A.S. Sefat, D.G. Mandrus, M.A. McGuire, B.C. Sales. Aligned crystallite powder of $NdFeAsO_{0.86}F_{0.14}$: magnetic hysteresis and penetration depth. Phys. Rev. B 79 224523 (2009). https://doi.org/10.1103/PhysRevB.79.224523.

[24] D. N. Zheng, H. D. Ramsbottom, D. P. Hampshire. Reversible and irreversible magnetization of the Chevrel phase superconductor PbMo6S8. Phys. Rev. B 52 (1995) 12931–12938. doi:10.1103/PhysRevB.52.12931.

[25] R. Liang, D. A. Bonn, W. N. Hardy, D. Broun. Lower critical field and superfluid density of highly under doped $YBa_2Cu_3O_{6+x}$ single crystals. Phys. Rev. Lett. 94 117001 (2005). doi:10.1103/PhysRevLett.94.117001.

[26] C. Putzke, P. Walmsley, J. D. Fletcher et al. Anomalous critical fields in quantum critical superconductors. Nature Communications 5 (5679). http://dx.doi.org/10.1038/ncomms6679.

[27] I. Pallecchi, C. Fanciulli, M. Tropeano, A. Palenzona, M. Ferretti, A. Malagoli, A. Martinelli, I. Sheikin, M. Putti, C. Ferdeghini. Upper critical field and fluctuation conductivity in the critical regime of doped SmFeAsO. Phys. Rev. B 79 104515 (2009). https://doi.org/10.1103/PhysRevB.79.104515.

[28] A. Srivastava, A. Pal, S. Singh, C. Shekhar, H.K. Singh, V.P.S. Awana, O.N. Srivastava. Magnetotransport and thermal properties characterization of 55 K superconductor $SmFeAsO_{0.85}F_{0.15}$, AIP Advances 3 (9) (2013) 092113. doi:https://doi.org/10.1063/1.4821335.

[29] Sangita Bose, Pratap Raychaudhuri, Rajarshi Banerjee, and Pushan Ayyub. Upper critical field in nanostructured Nb: Competing effects of the reduction in density of states and the mean free path. Phys. Rev. B 74, 224502 (2206). https://doi.org/10.1103/PhysRevB.74.224502.

[30] M. C. Fiolhais, J. L. Birman. Size effects in the Ginzburg–Landau theory. Solid State Communications 203 (2015) 51 – 53. https://doi.org/10.1016/j.ssc.2014.11.009.

[31] S. Bose, P. Ayyub. A review of finite size effects in quasi-zero dimensional superconductors. Reports on Progress in Physics 77 (11) 116503. http://dx.doi.org/10.1088/0034- 4885/77/11/116503.

[32] M. C. N. Fiolhais, J. L. Birman. Phenomenological correlations in high-temperature superconductors. EPL (Europhysics Letters) 107 (2) (2014) 27001. https://doi.org/10.1209/0295-5075/107/27001.

[33] Shiv J. Singh, Matthew Bristow, William R. Meier, Patrick Taylor, Stephen J. Blundell, Paul C. Canfield, and Amalia I. Coldea. Ultrahigh critical current densities, the vortex phase diagram, and the effect of granularity of the stoichiometric high-Tc superconductor $CaKFe_4As_4$. Phys. Rev. Materials 2, 074802. https://doi.org/10.1103/PhysRevMaterials.2.074802.

[34] Peidong Yang and Charles M. Lieber. Nanostructured high-temperature superconductors: Creation of strong-pinning columnar defects in nanorod/superconductor composites. Journal of Materials Research, Vol. 12, Issue 11, November 1997, (3981-3996). https://doi.org/10.1557/JMR.1997.0393.

[35] T. Plackowski et al. Reversible and irreversible magnetocaloric effect in the $NdBa_2Cu_3O_7$ superconductor in relation to specific heat and magnetization. J. Phys.: Condens. Matter 17 6871 (2005). https://doi.org/10.1088/0953-8984/17/43/007.

[36] V.A. Vlasenko, K.S. Pervakov, S.Yu. Gavrilkin, Yu.F. Eltsev. Unconventional Pinning in Iron Based Superconductors of 122 Family. Physics Procedia, Vol. 67, 952-957, (2015). https://doi.org/10.1016/j.phpro.2015.06.160.

[37] Hideo Hosono, Akiyasu Yamamoto, Hidenori Hiramatsu Yanwei Ma. Recent advances in iron-based superconductors toward applications. Materials Today, Volume 21, Issue 3, April 2018, Pages 278-302. https://doi.org/10.1016/j.mattod.2017.09.006.

[38] N. Ihara. T. Matsushita. Effect of flux creep on irreversibility lines in superconductors. Physica C 257 (1996) 223-231. https://doi.org/10.1016/0921-4534(95)00534-X.

[39] A. Sawa, H. Yamasaki, Y. Mawatari, H. Obara, M. Umeda, S. Kosaka. Thickness dependence of vortex-glass transition in $YBa_2Cu_3O_{7-\delta}$ thin films. Physica C 282-287 (1997) 2071. https://doi.org/10.1016/S0921-4534(97)01140-4.

[40] S.J. Singh, J. Shimoyama, A. Yamamoto, H. Ogino, K. Kishio. Transition Temperature and Upper Critical Field in $SmFeAsO_{1-x}F_x$ Synthesized at Low Heating Temperatures. IEEE Transactions on Applied Superconductivity, vol. 23, no. 3, (2013), Art no. 7300605. Doi:10.1109/TASC.2013.2239352.

[41] Teruo Matsushita. Flux Pinning in Superconductors. Chapter 8.5.1. Springer series in Solid-State Sciences 178. 2nd edition. Springer. 2014.

[42] T. Matsushita, E. S. Otabe, H. Wada, Y. Takahama, H. Yamauchi. Size dependencies of the peak effect and irreversibility field in superconducting Sm-123 powders. Physica C: Superconductivity, Vol. 397, Issues 1–2, 1 October 2003, pp. 38-46. https://doi.org/10.1016/S0921-4534(03)01085-2.

[43] T. Matsushita, T. Fujiyoshi, K. Toko, and K. Yamafuji. Flux creep and irreversibility line in high temperature oxide superconductors. Appl. Phys. Lett. 56, 2039 (1990). https://doi.org/10.1063/1.103011.

[44] Flux Pinning in Superconductors. Chapter 7.7. p. 304. Teruo Matsushita. Springer series in Solid-State Sciences 178. 2nd edition. Springer. 2014.

[45] Flux Pinning in Superconductors. Chapter 7.7. p. 348. Teruo Matsushita. Springer series in Solid-State Sciences 178. 2nd edition. Springer. 2014.

[46] Toshinori Ozaki, Lijun Wu, Cheng Zhang, Jan Jaroszynski, Weidong Si, Juan Zhou, Yimei Zhu and Qiang Li. A route for a strong increase of critical current in nanostrained iron-based superconductors. Nature Communications volume 7, Article number: 13036 (2016). DOI: 10.1038/ncomms13036.

[47] L. Fang, Y. Jia, V. Mishra, et al. Huge critical current density and tailored superconducting anisotropy in $SmFeAsO_{0.8}F_{0.15}$ by low-density columnar-defect incorporation. Nature Communications volume 4, Article number: 2655 (2013). DOI: 10.1038/ncomms3655.

[48] D. Solenov, M. Nikolo, J. Singleton, J. Jiang, J. Weiss, and E. Hellstrom. The impact of Maki parameter and spin orbit scattering constant in the WHH model on upper critical magnetic fields in Ni-and co-doped pnictide bulk superconductors. AIP Conference Proceedings 1895, 060004 (2017). https://doi.org/10.1063/1.5007389.

[49] G. Prando, P. Carretta, R. De Renzi, S. Sanna, A. Palenzona, M. Putti, and M. Tropeano. Vortex dynamics and irreversibility line in optimally doped $SmFeAsO_{0.8}F_{0.2}$ from ac susceptibility and magnetization measurements. Physical Review B 83, 174514 (2011). Doi:10.1103/PhysRevB.83.174514.

[50] R.S. Meena, K.V.R. Rao, Hari Kishan and V.P.S. Awana. Inter-comparison of electric and magnetic behaviour of superconducting quaternary oxypnictide compounds. IOP Conf. Series: Materials Science and Engineering 171 (2017) 012153. Doi:10.1088/1757-899X/171/1/012153.

[51] D. Ahmad, I. Park, G.C. Kim, J.H. Lee, Z.-A. Ren, Y.C. Kim. Irreversibility line and flux pinning properties in iron-based high-Tc superconductor $SmFeAsO_{0.85}$. Physica C: Superconductivity, vol. 469 (2009) 1052–1054. https://doi.org/10.1016/j.physc.2009.05.166.

[52] Hyun-Sook Lee et al. Effects of two gaps and paramagnetic pair breaking on the upper critical field of $SmFeAsO_{0.85}$ and $SmFeAsO_{0.8}F_{0.2}$ single crystals. Physical Review B 80, 144512 (2009). Doi: 10.1103/PhysRevB.80.144512.

[53] Xiangzhuo Xing, Wei Zhou, Jinhua Wang, Zengwei Zhu, Yufeng Zhang, Nan Zhou, Bin Qian, Xiaofeng Xu and Zhixiang Shi. Two-band and Pauli-limiting effects on the upper critical field of 112-type iron pnictide superconductors. Scientific Reports, vol.7, Article number: 45943 (2017). DOI: 10.1038/srep45943.

[54] Seunghyun Khim, Bumsung Lee, Jae Wook Kim, Eun Sang Choi, G. R. Stewart, and Kee Hoon Kim. Pauli-limiting effects in the upper critical fields of a clean LiFeAs single cristal. Physical Review B 84, 104502 (2011). DOI:10.1103/PhysRevB.84.104502.

[55] T. Tamegai, Y. Nakajima, Y. Tsuchiya, A. Iyo, K. Miyazawa, P.M. Shirage, H. Kito, H. Eisaki. Magneto-optical imaging of iron-oxypnictide $SmFeAsO_{1-x}F_x$ and $SmFeAsO_{1-y}$. Physica C 469 (2009) 915–920. https://doi.org/10.1016/j.physc.2009.05.098.

[56] . A. Yamamoto, A.A. Polyanskii, J. Jiang, F. Kametani, C. Tarantini, F. Hunte, J. Jaroszynski, E.E. Hellstrom, P.J. Lee, A. Gurevich, D.C. Larbalestier, Z.A. Ren, J.Yang, X.L. Dong, W. Lu and Z.X. Zhao. Evidence for two distinct scales of current flow in polycrystalline Sm and Nd iron oxypnictides. Supercond. Sci. Technol. 21 (2008) 095008 (11pp). Doi:10.1088/0953-2048/21/9/095008.

[57] J.H. Durrell, C.-B. Eom, A. Gurevich, E.E. Hellstrom, C. Tarantini, A. Yamamoto and D.C. Larbalestier. The behavior of grain boundaries in the Fe-based superconductors. Reports on Progress in Physics, Volume 74, Number 12. https://doi.org/10.1088/0034-4885/74/12/124511.

[58] Babar Shabbir, et al. Strong enhancement of critical current density in both low and high fields and flux pinning mechanism under hydrostatic pressure in optimally doped $(Ba,K)Fe_2As_2$ single crystals. Scientific Reports volume 6, Article number: 23044 (2016). Doi:10.1038/srep23044.

[59] Guanmei Wang, Mark J. Raine and Damian P. Hampshire. The cause of 'weak-link' grain boundary behaviour in polycrystalline $Bi_2Sr_2CaCu_2O_8$ and $Bi_2Sr_2Ca_2Cu_3O_{10}$ superconductors. Supercond. Sci. Technol. 31 (2018) 024001 (19pp). https://doi.org/10.1088/1361-6668/aaa1b8.

[60] A. Gurevich. Nonlocal Josephson electrodynamics and pinning in superconductors. https://doi.org/10.1103/PhysRevB.46.3187.

[61] S. Senoussi. Review of the critical current densities and magnetic irreversibilities in high T_c superconductors. J. Phys. III France 2 (1992) 1041-1257. (Page 1064).

[62] E. Shimizu and D. Ito. Critical current density obtained from particle-size dependence of magnetization in $YBa_2Cu_3O_{7-\delta}$ powders. Physical Review B, 39, 4. 1 Feb. 1989. https://doi.org/10.1103/PhysRevB.39.2921.

[63] Philip J.W. Moll, Roman Puzniak, Fedor Balakirev, Krzysztof Rogacki, Janusz Karpinski, Nikolai D. Zhigadlo and Bertram Batlogg. High magnetic-field scales and critical currents in SmFeAs(O, F) crystals. Nature Materials volume 9, pages 628–633(2010). DOI: 10.1038/NMAT2795.

[64] B. Ni, J. Ge, M. Kiuchi, E.S. Otabe, Z. Gao, L. Wang, Y. Qi, X. Zhang, Y. Ma. Critical current characteristics and history dependence in superconducting SmFeAsOF bulk. Journal of Physics: Conference Series 234 (2010) 012028. Doi:10.1088/1742-6596/234/1/012028.

[65] S. Demirdis, and C. J. van der Beek. Strong pinning and vortex energy distributions in single-crystalline $Ba(Fe_{1-x}Co_x)_2As_2$. Physical Review B 84, 094517 (2011). DOI: 10.1103/PhysRevB.84.094517.

[66] C. J. van der Beek, G. Rizza, M. Konczykowski et al. Flux pinning in PrFeAsO0.9 and NdFeAsO0.9F0.1 superconducting crystals. Physical Review B 81, 174517 (2010). DOI: 10.1103/PhysRevB.81.174517.

[67] Pallecchi I, Tropeano M, Lamura G, Pani M, Palombo M, Palenzona A and Putti M. Upper critical fields and critical current densities of Fe-based superconductors as compared to those of other technical superconductors. Physica C: Superconductivity and its Applications, Vol. 482, 68-73, (2012). https://doi.org/10.1016/j.physc.2012.05.015.

[68] Nadezda Yu. Panarina, Yurii I. Talanov, Tatyana S. Shaposhnikova et al. Pinning effects in ceramic SmO1−xFxFeAs as revealed by microwave absorption. Phys. Rev. B 81 224509 (2010). https://doi.org/10.1103/PhysRevB.81.224509.

7 Conclusions

This work studies the effects that particle size reduction has on the superconducting properties of the iron-based superconductor $SmFeAsO_{0.91}F_{0.09}$. The thesis is focused on the behavior of the critical fields (H_{c1}, H^*, H_{irr}, H_{c2}), the characteristic lengths (λ, ξ_{eff}) and the critical currents (J_c, J_{intra}, J_D) of this material. Although at present it is not feasible to accurately control the particle size in these materials, it was possible to determine the behavior followed by the fundamental parameters mentioned above as the particle size was changed from 220 to 1680 nm. The trends observed should be valid for any particle with a size between 220-600 nm, that is, for particles whose size is similar to the penetration length λ.

It was synthetized a polycrystalline powder sample with a T_c= 56.1 K. *The milling did not affect the crystalline structure* of the set of samples ($220 \leq r_g \leq 1680$ nm); this fact was verified by XRD.

The magnetic characterization provides the experimental data in which the conclusions of this thesis are based. The *granular nature* of the samples was stablished by the presence of a second transition around T = 19 K, in the M-T curves. On the other side, the virgin magnetization region was studied in the M-H curves. It was found that H_{c1}, which limits the Meissner regime, exhibit a *quadratic power law dependence on the particle size*: $H_{c1} \sim r_g^2$. Moreover, H^* that limits the virgin magnetization region follows a *logarithmic law* as a function of r_g: $H^* = H_0(1 + \frac{r_g}{r_0})$, with H_0=709.97 Oe and r_0=178 nm. Both experimental results are in agreement with some theoretical models of HTS.

The experimental values obtained for H_{c1} were used to calculate the effective coherence length ξ_{eff}. *This parameter gets shorter as the particle size diminishes, following a quadratic power law*: $\xi_{eff} \sim r_g^2$, taking values from 2.5 nm for the sample with r_g = 1680 nm, to 0.37 nm for r_g= 220 nm. The quadratic dependence of ξ_{eff} as a function of r_g agrees with a recently proposed model for clean type II HTS, which affirms that in particles with the same scale as λ appears a new ground state (E_1), leading to a discretization of the energy spectrum.

H_{irr} was determined directly from M-H hysteresis loops, the values going from 15.8 to 7.1 kOe, with decreasing r_g. For particles whose size is similar to the penetration length λ ($220 \leq r_g \leq$ 550 nm), H_{irr} *diminishes linearly with* r_g, while for larger particle size (r_g = 1680 nm) it reaches a saturation value. *This behavior is well represented by the small particle limit of the flux creep model*.

The values of H_{irr} were used to estimate $H_{c2}(0)$ *(107 T for r_g = 1680 nm)*, with the aid of the *flux creep* model. The values are much lower than the ones proposed early after the discovery of IBSC, but are in agreement with the experimental behavior of H_{irr} and the tendency observed in recent experimental studies.

J_{intra}(H) was calculated by measuring the width of the magnetization loop in the M-H curves. *Two types of vortex pinning mechanisms were found*: For low H the *strong vortex pinning* dominates. In the intermediate H regime, the *weak collective pinning* dominates. The highest value of J_{intra} was obtained for the sample with r_g= 220 nm. However, this is true only for a low applied field (< 500 Oe). The intergranular J_c was determined in a similar way as J_{intra} for the as sintered sample (r_g = 1680 nm) only. The *low value* J_c= 6.56x10^5 A·m^{-2} *is caused by the weak-link problem*.

The calculated values of ξ_{eff} were used to calculate λ_{eff}, and these were in turn used to calculate J_D. The calculated values of this critical current are one order of magnitude larger than J_{intra}. J_D *decreases linearly with particle size* for values of r_g of the order of λ. While for a particle size r_g=1680 nm, J_D reaches its bulk value. This is the same behavior observed for $H_{irr}^{1/3}$.

The compound $SmFeAsO_{1-x}F_x$ has a low J_c anisotropy, so that, although the J_c values are low, the fabrication of wires or tapes would not require texturing processes. Moreover, $SmFeAsO_{1-x}F_x$ has a strong pinning potential, which give high J_{intra} values. These characteristics together with its high upper critical field, make this material feasible for magnetic field applications. Nevertheless, it is necessary to increase J_c to values close to J_{intra}. In this regard, a possible way to improve intergranular vortex pinning, which would increase J_c, is by reducing the anisotropy caused by the crystalline layered structure of $SmFeAsO_{1-x}F_x$. This can be done by introducing nano-scale columnar defects in the crystalline structure by heavy-ion irradiation.

Although the study of particle size effects on type I superconductors began in the mid-20th century, little has been said about this topic for high critical temperature superconductors, and even less about iron-based superconductors, because all the attention has been focused on copper-based materials. In that sense, the conclusions of this thesis are pioneering results in this research field, covering the fundamental parameters that need to be studied in any superconducting material. In addition, the methodology used in this work could be used in the study of other materials.

8 Future perspectives

As can be seen from the results of this work, the iron-based superconductor $SmFeAsO_{1-x}F_x$ has some properties that make it feasible for technological applications. In particular, the expected high value for the upper critical field H_{c2}, and the large intergranular critical current density, seem promising in this regard. However, the disadvantage of low intergranular critical current density remains to be solved. Once this problem is overcome, the material could be used in the generation of huge magnetic fields. This would undoubtedly open up new possibilities for scientific research and technological applications in a variety of fields.

Thus, in the future, a research line could be focused on the improvement of the critical fields and currents of the Josephson junctions that couple the grains in the HTS. Hopefully, such research will provide a solution to the low intergranular critical current density. The objective of a second research line can be the development of a synthesis process that allows controlling precisely the particle size of the HTS. This would give applicability to the knowledge acquired in the study of size effects in HTS.

From the perspective of basic science, it might be useful to investigate the behavior of the critical fields, the characteristic lengths and the critical currents for particle size below 220 nm, which is the minimum size achieved in the present study, and is also a value close to the magnitude of the penetration depth of $SmFeAsO_{1-x}F_x$. The results of such research could be important for the understanding of the physics involved in Cooper pair breaking induced by the shrinkage of particle size.

Appendices

A. Derivation of eq. (2.14)

It is necessary to take the curl of Eq. 2.11:

$$\nabla \mathrm{X}\boldsymbol{E} = \frac{4\pi}{c^2}\lambda_L^2 \nabla \mathrm{X}\left(\frac{d\boldsymbol{J}}{dt}\right) \tag{A.1}$$

Using Maxwell´s equation $\nabla \mathrm{X}\boldsymbol{E} = -\frac{1}{c}\frac{\partial \boldsymbol{B}}{\partial t}$, and later taking the curl of eq. (A.1)

$$-\frac{1}{c}\nabla \mathrm{X}\left(\frac{\partial \boldsymbol{B}}{\partial t}\right) = \frac{4\pi}{c^2}\lambda_L^2\left[\nabla \mathrm{X}\left(\nabla \mathrm{X}\left(\frac{\partial \boldsymbol{J}}{\partial t}\right)\right)\right] = \frac{4\pi}{c^2}\lambda_L^2\left[\nabla\left(\nabla\cdot\left(\frac{\partial \boldsymbol{J}}{\partial t}\right)\right) - \nabla^2\left(\frac{\partial \boldsymbol{J}}{\partial t}\right)\right] \tag{A.2}$$

But $(\nabla\cdot\mathbf{J})$= 0 by the conservation of charge in a steady state. Then, the first term of the right member of eq. (A.2) is null. Thus, the above equation is rewritten

$$\frac{c}{4\pi\lambda^2}\nabla \mathrm{X}\left(\frac{\partial \boldsymbol{B}}{\partial t}\right) = \nabla^2\left(\frac{\partial \boldsymbol{J}}{\partial t}\right) \tag{A.3}$$

But $\nabla \mathrm{X}\,\boldsymbol{B} = \frac{4\pi}{c}\,\boldsymbol{J}$, then

$$\frac{1}{\lambda^2}\left(\frac{d\boldsymbol{J}}{dt}\right) = \nabla^2\left(\frac{d\boldsymbol{J}}{dt}\right) \tag{A.4}$$

Integrating

$$\frac{1}{\lambda^2}J = \nabla^2 J \tag{2.14}$$

B. Derivation of eq. (2.31)

The free energy of a superconductor immersed in a magnetic field, is given by eq. 2.17, with all its terms:

$$F_s - F_{n0} = \alpha|\psi|^2 + \frac{\beta}{2}|\psi|^4 + \frac{|(-i\hbar\nabla - (\mathrm{e}^*\mathrm{A}/\mathrm{c}))\,\psi|^2}{2m^*} + \frac{H^2}{8\pi}$$

With the purpose to find the minimum of the free energy expressed above, it is necessary to take the derivative with respect to the vector potential $\boldsymbol{A}$ and make it equal to 0.

$$\frac{\delta}{\delta \boldsymbol{A}}(F_s - F_{n0}) = \frac{\delta}{\delta \boldsymbol{A}}\left(\alpha|\psi|^2 + \frac{\beta}{2}|\psi|^4 + \frac{\left|\left(-i\hbar\nabla - \left(\frac{\mathrm{e}^*\mathbf{A}}{\mathrm{c}}\right)\right)\psi\right|^2}{2m^*} + \frac{H^2}{8\pi}\right) = \frac{\delta}{\delta \boldsymbol{A}}\frac{|(-i\hbar\nabla - (\mathrm{e}^*\mathbf{A}/\mathrm{c}))\,\psi|^2}{2m^*} + \frac{\delta}{\delta \boldsymbol{A}}\frac{H^2}{8\pi}=0 \tag{2.30}$$

The first term of eq. 2.30 can be extended as follows:

$$\frac{\delta}{\delta \boldsymbol{A}}\frac{|(-i\hbar\nabla - (\mathrm{e}^*\mathbf{A}/\mathrm{c}))\,\psi|^2}{2m^*} = \frac{1}{2m^*}\frac{\delta}{\delta \boldsymbol{A}}\left[\left(i\hbar\nabla - \frac{\mathrm{e}^*\mathbf{A}}{\mathrm{c}}\right)\psi^* \cdot \left(-i\hbar\nabla - \frac{\mathrm{e}^*\mathbf{A}}{\mathrm{c}}\right)\psi\right]$$

$$= \frac{1}{2m^*}\left[\left(-\frac{\mathrm{e}^*\frac{\delta}{\delta \boldsymbol{A}}\mathbf{A}\psi^*}{\mathrm{c}}\right)\cdot\left(-i\hbar\nabla - \frac{\mathrm{e}^*\mathbf{A}}{\mathrm{c}}\right)\psi + \left(-\frac{\mathrm{e}^*\frac{\delta}{\delta \boldsymbol{A}}\mathbf{A}\psi}{\mathrm{c}}\right)\cdot\left(i\hbar\nabla - \frac{\mathrm{e}^*\mathbf{A}}{\mathrm{c}}\right)\psi^*\right]$$

$$= \frac{1}{2m^*}\left[\frac{i\hbar\mathrm{e}^*\left(\frac{\delta}{\delta \boldsymbol{A}}\mathbf{A}\cdot\nabla\psi\right)\psi^*}{\mathrm{c}} - \frac{\mathrm{i}\hbar\mathrm{e}^*\left(\frac{\delta}{\delta \boldsymbol{A}}\mathbf{A}\cdot\nabla\psi^*\right)\psi}{\mathrm{c}} + \frac{e^{*2}\left(\frac{\delta}{\delta \boldsymbol{A}}\mathbf{A}\cdot\boldsymbol{A}\right)|\psi|^2}{c^2} + \frac{e^{*2}(\boldsymbol{A}\cdot\frac{\delta}{\delta \boldsymbol{A}}\mathbf{A})|\psi|^2}{c^2}\right]$$

$$= \left[\frac{-i\hbar\mathrm{e}^*}{2m^*c}(\psi\cdot\nabla\psi^* - \psi^*\cdot\nabla\psi) + \frac{2e^{*2}|\psi|^2\boldsymbol{A}}{2m^*c^2}\right]\cdot\frac{\delta}{\delta \boldsymbol{A}} \tag{2.31}$$

C. Derivation of eq. (3.7)

As pointed out in chapter 3.3, the calculation of ψ or ϵ_1 requires the solution of the nonlinear Ginzburg-Landau equations:

$$\alpha\psi + \beta|\psi|^2\psi + \frac{1}{4m}(-i\hbar\nabla - \frac{2e\boldsymbol{A}}{c})^2\psi = 0 \qquad (2.38)$$

and

$$\boldsymbol{J} = \frac{ei\hbar}{2m}(\psi\cdot\nabla\psi^* - \psi^*\cdot\nabla\psi) - \frac{2e^2|\psi|^2\boldsymbol{A}}{mc} \qquad (2.35).$$

However, it is possible to approximate a solution, and even find a useful analytic result for the limit κ >> 1. Let us consider the case with arbitrary κ. The vortex wave function is obtained by normalizing the order parameter:

$$\psi = \psi_\infty f(r)e^{i\theta} \qquad (C.1).$$

From the cylindrical symmetry of a vortex, it is assumed that $\psi = \psi(r)$, with r the length from the center of the flux line. The phase of ψ along one circle of radius r changes by 2π, and the factor $e^{i\theta}$ accounts for that. In addition, eq. (C.1) defines the vector potential as:

$$\boldsymbol{A} = A(r)\widehat{\boldsymbol{\theta}} \qquad (C.2).$$

This equation leads to two values of $A(r)$, one for r ≤ ξ (near the core of the vortex), and other for r > ξ (most of the vortex and the bulk of the material).

By substituting eq. (C.1) in (2.38), leads to: $f - f^3 - \xi^3\left[\left(\frac{1}{r} - \frac{2\pi\boldsymbol{A}}{\Phi_0}\right)^2 f - \frac{1}{r}\frac{d}{dr}\left(r\frac{df}{dr}\right)\right] = 0$ (C.3).

From eq. (C.2), the current has only one component ($\widehat{\boldsymbol{\theta}}$), and from eq. 2.35:

$$\boldsymbol{J} = \frac{-c}{4\pi}\frac{d}{dr}\left[\frac{1}{r}\frac{d}{dr}(r\boldsymbol{A})\right] = \frac{e\hbar}{m}\psi_\infty^2 f^2\left(\frac{1}{r} - \frac{2\pi\boldsymbol{A}}{\Phi_0}\right) \qquad (C.4).$$

The problem consists in solving the system of differential equations (C.3) and (C.4). Considering that $B = \nabla X A(r)\widehat{\boldsymbol{\theta}}$, and by using cylindrical coordinates, $\nabla X A(r)\widehat{\boldsymbol{\theta}} = \frac{1}{\boldsymbol{r}}\frac{\partial}{\partial r}rA(r)\widehat{\boldsymbol{\theta}}$, leads to $A(r) = \frac{h(0)r}{2}$ for small values of r (close to the core). Putting this in eq. (C.3) gives:

$$f - f^3 - \xi^3\left[\left(\frac{1}{r} - \frac{\pi h(0)r}{\Phi_0}\right)^2 f - \frac{1}{r}\frac{d}{dr}\left(r\frac{df}{dr}\right)\right] = 0 \qquad (C.5)$$

The function f of eq. (C.5) has to fulfill three requirements: First, it has to be a solution of eq. (C.5). Second, the order parameter tends rapidly to zero in the region $r < \xi$; third, the order parameter tends to a limiting value (ψ_∞) far from the core of the vortex. All requirements are kept by the approximate solution ($f \approx \psi$)

$$f \approx \tanh\frac{\nu r}{\xi} \qquad (3.7)$$

D. Balancing of chemical equations

The chemical balance used in preparing $SmFeAsO_wF_y$ by a solid-state reaction process is:

a(Sm)+**b**(SmF_3)+**c**(As)+**d**(Fe)+**e**(Fe_2O_3) → **x**($SmFeAsO_wF_y$)

The system of linear equations associated to the previous equation is:

1) **a**(Sm) + **b**(SmF_3) = **x**(Sm)

2) **d**(Fe) + 2**e**(Fe_2O_3) = **x**(Fe), the coefficient e is multiplied by 2 because Fe_2O_3 has two atoms of Fe.

3) **c**(As) = **x**(As)

4) 3**e**(Fe_2O_3) = **x**(**w**)(O), the coefficient e is multiplied by 3 because Fe_2O_3 has three atoms of O and the coefficient (**w**) comes from the oxygen subscript in the product of the balance equation.

5) 3**b**(SmF_3) = **x**(**y**)(F), the coefficient **y** comes from the fluoride subscript on the right side of the balance equation.

The example will be calculated for $SmFeAsO_{0.65}F_{0.2}$. Then, the system of linear equations has to be set out with **x**=1, **y**=0.2 and **w**=0.65:

1) **a** + **b** = 1

2) **d** + 2**e** = 1

3) **c** = 1

4) 3**e** = 0.65

5) 3**b** = 0.2

The system can be solved by simple substitution or by using matrices.

First **x=1**.

Then, from 3): **c=1.**

By 4): **e**$= \frac{65}{100*3} = \frac{13}{20*3} = \mathbf{\frac{13}{60}}$.

From eq. 5): **b** $= \frac{0.2}{3} = \frac{2}{10*3} = \mathbf{\frac{1}{15}} = \mathbf{\frac{4}{60}}$**.**

Previous results give: 2) **d**$+2\left(\frac{13}{60}\right)=1$. Thus, **d** $= 1 - \frac{26}{60} = \mathbf{\frac{34}{60}}$.

And: Eq. 1) **a**+$\left(\frac{4}{60}\right)$= 1. Thus, $\mathbf{a} = 1 - \frac{4}{60} = \mathbf{\frac{56}{60}}$.

A simple way to verify:

a+**b**= 1. $\frac{56}{60} + \frac{4}{60} = 1$

d+2**e**= 1. $\frac{34}{60} + \frac{26}{60} = 1.$

3**e**= 0.65. $3\left(\frac{13}{60}\right) = 0.65.$

3**b**= 0.2. $3\left(\frac{4}{60}\right) = 0.2.$

The system of linear equations can also be solved by using a matrix method. Equations 1-5 can be written as:

$$\begin{bmatrix} 1 & 1 & 0 & 0 & 0 & | & \mathbf{1} \\ 0 & 0 & 0 & 1 & 2 & | & \mathbf{1} \\ 0 & 0 & 1 & 0 & 0 & | & \mathbf{1} \\ 0 & 0 & 0 & 0 & 3 & | & \mathbf{(65/100)} \\ 0 & 3 & 0 & 0 & 0 & | & \mathbf{(20/100)} \end{bmatrix}$$

Applying elementary matrix operations:

$$\begin{bmatrix} 1 & 0 & 0 & 0 & 0 & | & \mathbf{(280/300)} \\ 0 & 0 & 0 & 1 & 0 & | & \mathbf{(170/300)} \\ 0 & 0 & 1 & 0 & 0 & | & \mathbf{1} \\ 0 & 0 & 0 & 0 & 1 & | & \mathbf{(65/300)} \\ 0 & 1 & 0 & 0 & 0 & | & \mathbf{(20/300)} \end{bmatrix}$$

The results from the last matrix are: **a** =$\frac{280}{300} = \frac{56}{60}$, **b** =$\frac{20}{300} = \frac{4}{60}$, **c** = 1, **d** =$\frac{170}{300} = \frac{34}{60}$, **e** =$\frac{65}{300} = \frac{13}{60}$.

Choosing a convenient amount of reactants, we need to calculate the moles of samarium in 0.4 g.

$$\frac{1\ mol\ Sm}{150.36\ g} : \frac{x\ mol}{0.4\ g}$$

The result is that 0.4 g of samarium represent a quantity of 0.002660281 mol of samarium. This number represents a fraction of $\frac{56}{60}$ from the total amount of samarium present in the reactants. So we need to calculate the total amount of samarium considering both the reactants Sm and SmF_3:

$$\frac{0.002660281\ mol}{{}^{56}/_{60}} : \frac{x\ mol}{1}$$

The result is 0.002850301071 mol of samarium present in the reactants. The quantity (in grams) of reactants can be calculated by using this result and the previously determined coefficients.

Fe_2O_3:

$$\frac{1\ mol\ Fe_2O_3}{159.68\ g}: \frac{0.002850301071\ \ mol}{x\ g}$$

The result is 0.4551360750 g. Now, multiplying by the corresponding coefficient (**e**= $\frac{13}{60}$), the quantity of Fe_2O_3 necessary is 0.0986 g.

The quantities of the rest of the reactants can be calculated following the previous procedure. The results are:

SmF_3=0.0394 g.

As=0.2135 g.

Fe=0.0902 g.

E. Pictures of the experiments

1. Synthesis of the superconductor $SmFeAsO_{1-x}F_x$.

Fig. E-1. The chemical precursors were mixed by grinding inside the glove box shown in the photograph, under a highly pure argon atmosphere.

2. Resistance-Temperature measurements

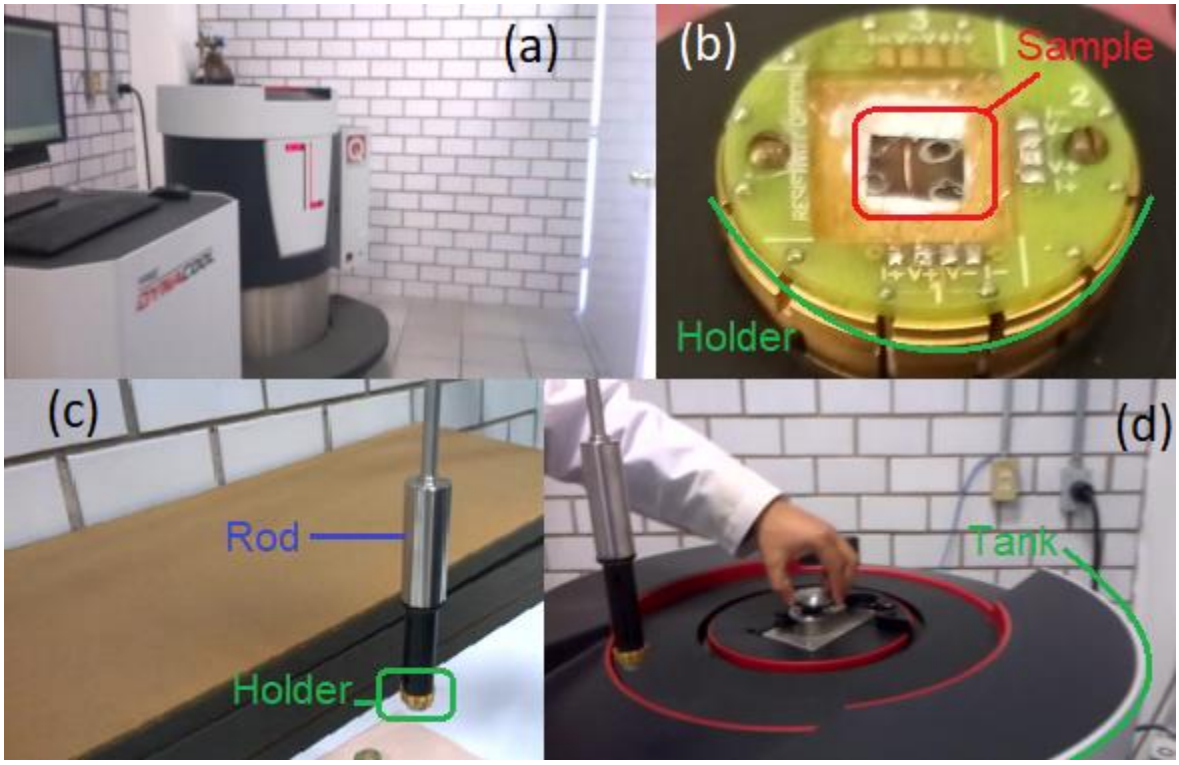

Fig. E-3. In (a) the PPMS equipment (without the VSM module). (b) shows the electrical connections between the sample (a similar sample) and the holder. This arrangement is necessary to perform R-T measurement. (c) shows the coupling of the holder to the rod. Fig. (d) shows the placement of the sample inside the PPMS tank.

3. Magnetic measurements

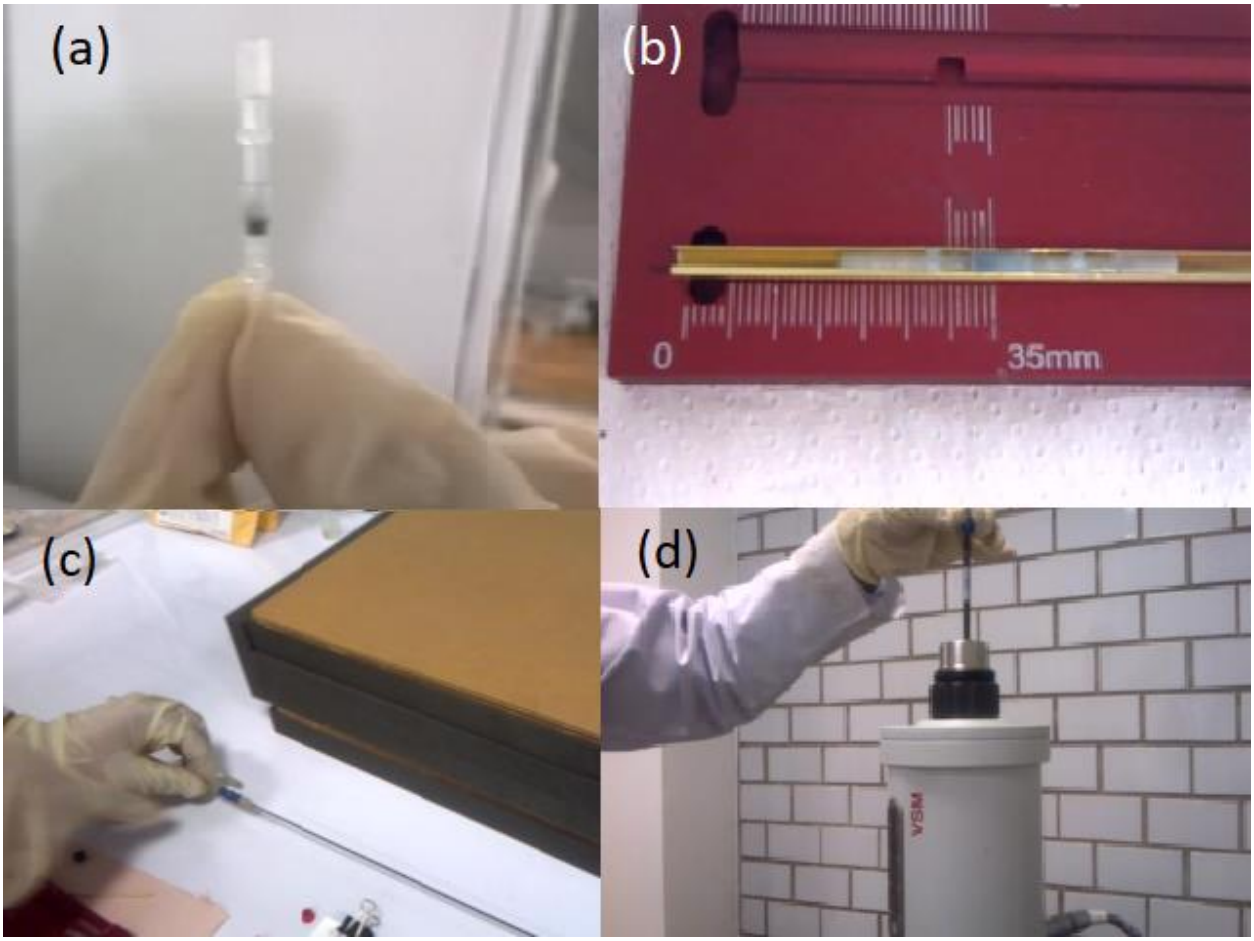

Fig. E-4. The first picture (a) shows a small quantity of superconducting powder (dark) inside the sample carrier. Then, the sample is fixed in a holder, the distance between the tip of the holder and the superconducting powder must be precise (35 mm), as can be seen in Fig. (b). Then, the holder is attached to a rod (Fig. c). Finally, in Fig. d, the VSM module is coupled to the PPMS tank and the rod is placed inside the PPMS tank.

F. Diamagnetic signal from VSM measurements

Magnetization vs. Magnetic field curves (M-H) measured from the $SmFeAsO_{0.91}F_{0.09}$ sample in the superconducting state, $T < T_c$=56.1 K, show a narrow ferromagnetic hysteresis. The presence of a ferromagnetic background in $SmFeAsO_{1-x}F_x$ was first reported by Senatore et al. [1], and is attributed to unreacted Fe and Fe_2O_3 in the sample. In consequence, the M-H curves obtained directly from VSM measurements are considered the sum of a diamagnetic contribution and a ferromagnetic complement [1,2].

In pursuance of isolating the diamagnetic signal, the ferromagnetic contribution was considered as a temperature independent background, and the M-H curves measured for $T > T_c$ (with only the ferromagnetic signal) were subtracted from the corresponding curves measured under T_c (which includes diamagnetic and ferromagnetic signals). The procedure is based on references [1,3], and is described in the following.

In the first instance, the hysteresis loop for the sample with particle size of 550 nm was measured[14] under the conditions T=50 K, and $-1000 \leq H \leq 1000$ Oe (see Fig. a). The loop shows a ferromagnetic behavior in spite of the temperature being under T_c. The net magnetization measured by the VSM consists of the sum of a diamagnetic and a ferromagnetic signal. A second measurement was performed under similar conditions, but this time at T=70 K, so that the material is not in the superconducting state and, in consequence, the diamagnetic contribution is null. Thus, the net magnetization measured by the VSM comes only from the ferromagnetic contribution (see Fig. b). The magnetization in (b) is greater than that in (a) because it is not attenuated by the diamagnetic signal.

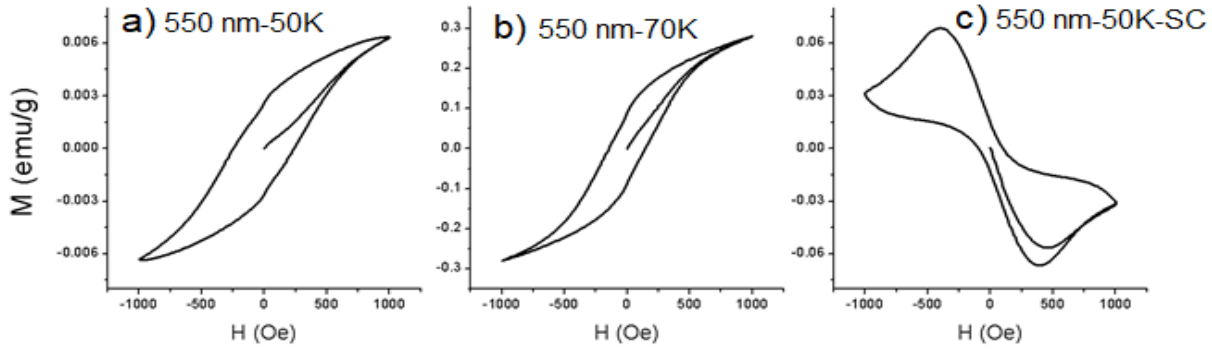

[14] M-H measurements were performed on a Quantum Design PPMS Dynacool, in the Physics Department, of CINVESTAV Zacatenco.

[1] Physical Review B **78**, 054514 (2008). https://doi.org/10.1103/PhysRevB.78.054514.

[2] Chinese Physics Letters, Volume 26, Number 3. https://doi.org/10.1088/0256-307X/26/3/037401.

[3] Modern Physics Letters B, Vol. 26, No. 30 (2012) 1250197. Doi: 10.1142/S0217984912501977.

The hysteresis loop of Fig. c is the result of subtracting the experimental data in Fig. b from data in Fig. a. The subtraction of the experimental data is an elementary arithmetic operation. However, the experimental data must be ordered to ensure that the values of magnetization M from (a) and (b) that are subtracted, have been measured for similar magnitudes of applied field H. For example, the magnetization M_{50K} and M_{70K} in row 1 of the table below can be subtracted, because their corresponding values of applied field (H) are similar. The result is in column M_{sc}, and can be used to plot (c). On the contrary, M_{50K} and M_{70K} in row 3 have different values of H, and cannot be used to plot (c).

Row	a) 550 nm-50 K		b) 550 nm-70 K		c) 550nm- 50 K SC	
	H (Oe)	M_{50K} (emu/g)	H (Oe)	M_{70K} (emu/g)	H (Oe)	M_{SC} (emu/g)
1	50	0.00212	50	0.00107	50	0.00105
2	62	0.00258	62	0.00115	62	0.00143
3	74	0.00305	91	0.00123	---	---
4	110	0.00398	135	0.00131	---	---

Following the method explained above, the diamagnetic magnetization due to superconductivity can be isolated from the M-H measurements. Once the diamagnetic signal is isolated, the hysteresis loops can be used to study the superconducting properties. This procedure was used in all M-H measurements, so the present work is probably the first in applying the method to study the particle size effects in an iron-based superconductor.